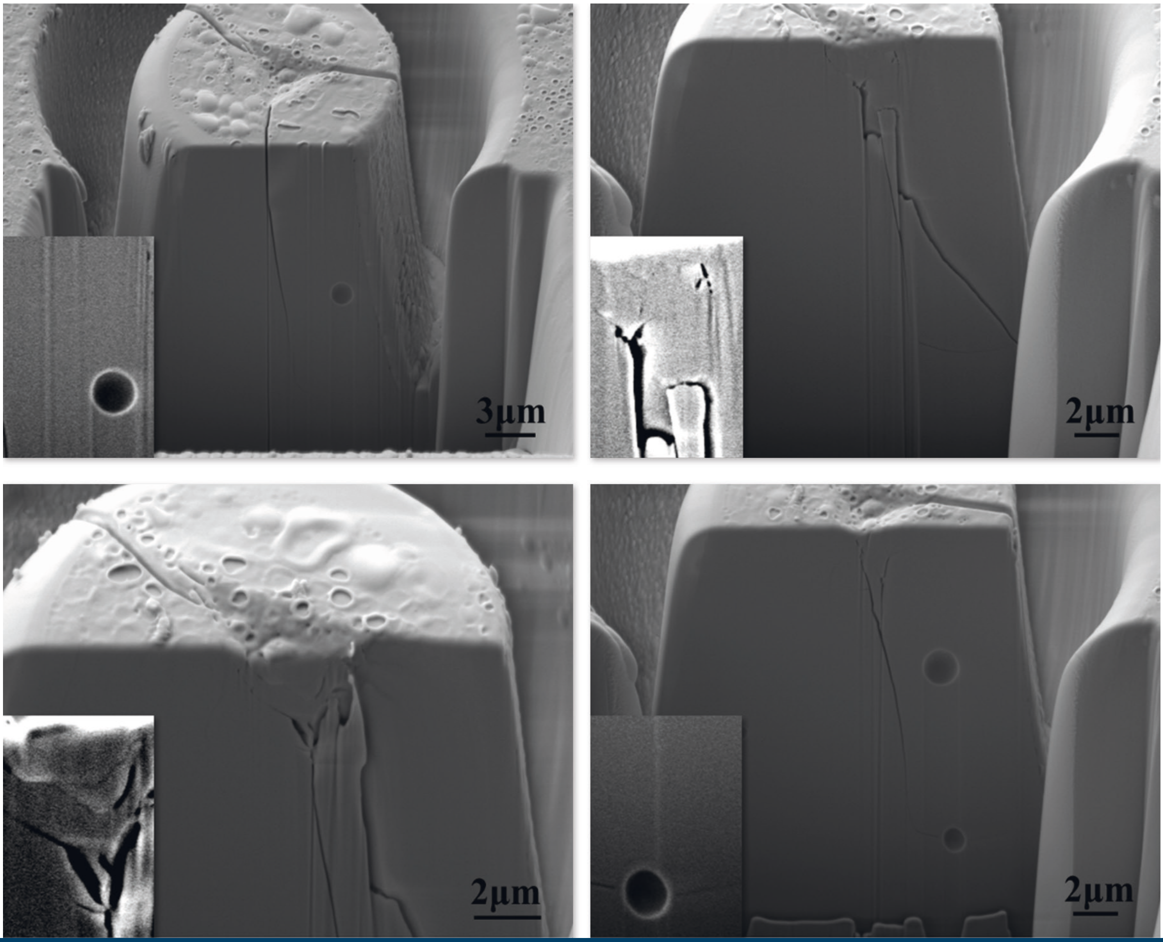

Mechanical properties of single and dual phase proton conducting membranes

Wenyu Zhou

Energie & Umwelt / Energy & Environment
Band / Volume 584
ISBN 978-3-95806-645-8

UNIVERSITY
OF TWENTE.

JÜLICH
Forschungszentrum

Schriften des Forschungszentrums Jülich
Reihe Energie & Umwelt / Energy & Environment Band / Volume 584

Forschungszentrum Jülich GmbH
Institut für Energie- und Klimaforschung
Werkstoffstruktur und -eigenschaften (IEK-2)

Mechanical properties of single and dual phase proton conducting membranes

Wenyu Zhou

Schriften des Forschungszentrums Jülich
Reihe Energie & Umwelt / Energy & Environment Band / Volume 584

ISSN 1866-1793 ISBN 978-3-95806-645-8

Bibliografische Information der Deutschen Nationalbibliothek.
Die Deutsche Nationalbibliothek verzeichnet diese Publikation in der
Deutschen Nationalbibliografie; detaillierte Bibliografische Daten
sind im Internet über http://dnb.d-nb.de abrufbar.

Herausgeber und Vertrieb: Forschungszentrum Jülich GmbH
Zentralbibliothek, Verlag
52425 Jülich
Tel.: +49 2461 61-5368
Fax: +49 2461 61-6103
zb-publikation@fz-juelich.de
www.fz-juelich.de/zb

Umschlaggestaltung: Grafische Medien, Forschungszentrum Jülich GmbH

Druck: Grafische Medien, Forschungszentrum Jülich GmbH

Schriften des Forschungszentrums Jülich
Reihe Energie & Umwelt / Energy & Environment, Band / Volume 584

(Diss. Univ. Twente, 2022)

ISSN 1866-1793
ISBN 978-3-95806-645-8

Content

SUMMARY

SAMENVATTING

1 Introduction 1

1.1 Energy consumption 2

1.2 Hydrogen production technologies 3

1.3 Hydrogen separation membranes 4

1.3.1 Mechanism of hydrogen separation 5

1.3.2 Membrane materials 6

1.4 Scope of the thesis 9

References 12

2 Promoting densification and grain growth of $BaCe_{0.65}Zr_{0.2}Y_{0.15}O_{3-\delta}$ at 1500 °C with a low amount of NiO as sintering aid 17

Abstract 17

2.1 Introduction 18

2.2 Experimental 19

2.3 Results and discussion 21

2.3.1 Powder pre-treatment 21

2.3.2 Sintering with NiO 22

2.3.3 Global and local chemistry 24

2.3.4 Mechanism for promoting densification and grain growth 27

2.4 Conclusions 34

References 35

Appendix A2 41

3 Mechanical properties of BaCe$_{0.65}$Zr$_{0.2}$Y$_{0.15}$O$_{3-\delta}$ proton-conducting material determined using different nanoindentation methods........ 43

Abstract... 43

3.1 Introduction 44

3.2 Experimental.. 46

3.3 Results and discussion 50

3.3.1 Phase constituents and microstructure 50

3.3.2 Elastic modulus and hardness 51

3.3.3 Fracture toughness.. 52

3.4 Conclusions 60

References 62

4 High temperature compressive creep behaviour of BaCe$_{0.65}$Zr$_{0.2}$Y$_{0.15}$O$_{3-\delta}$ in air and 4% H$_2$/Ar 67

Abstract... 67

4.1 Introduction 68

4.2 Experimental.. 69

4.3 Results and discussion 72

4.3.1 Creep behaviour in 4% H_2/Ar 72

4.3.2 Microstructural investigations 75

4.3.3 Creep behaviour in air 77

4.3.4 Decomposition investigation 83

4.4 Conclusions 88

References 90

5 Mechanical properties of $BaCe_{0.65}Zr_{0.2}Y_{0.15}O_{3-\delta}$-$Ce_{0.85}Gd_{0.15}O_{2-\delta}$ dual-phase proton-conducting material with emphasis on micro-pillar splitting 95

Abstract 95

5.1 Introduction 96

5.2 Experimental 98

5.3 Results and discussion 101

5.3.1 Phase and microstructure characterizations 101

5.3.2 Mechanical properties 104

5.4 Conclusions 114

References 116

Appendix A5 124

6 Reflections and perspectives 127

6.1 Introduction 128

6.2 Material preparation 128

6.3 Mechanical properties 130

6.4 Conclusions 131

References 133

Acknowledgements

About the author

SUMMARY

Dual-phase hydrogen permeation membranes, consisting of protonic and electronic conducting phases, shows great potential for high purity hydrogen production due to its high stability in harsh applications. Hydrogen-ion conductive perovskite phases (e.g. $BaCe_{0.65}Zr_{0.2}Y_{0.15}O_{3-\delta}$) and electron conductive fluorite oxides (e.g. $Ce_{0.85}Gd_{0.15}O_{2-\delta}$) are promising candidate for this biphasic hydrogen transport membrane. Mechanical properties (e.g. elastic modulus, hardness, fracture toughness) of the membranes are essential parameters regarding the reliability of subsequent applications. These parameters are closely related to microstructural features such as grain size, phase distribution and defects (e.g. pores and microcracks). However, these relationships are not yet fully understood. Therefore, in this thesis, the effects of grain size, phase distribution, pores and microcracks on mechanical properties are investigated for $BaCe_{0.65}Zr_{0.2}Y_{0.15}O_{3-\delta}$ and $BaCe_{0.65}Zr_{0.2}Y_{0.15}O_{3-\delta}$-$Ce_{0.85}Gd_{0.15}O_{2-\delta}$ membranes. Material preparation procedures (e.g. milling and sintering) are optimized to overcome the difficulty in material preparation.

Chapter 1 of this thesis introduces the currently known fundamental concepts (e.g. mechanisms of hydrogen transport and material candidates) and prospective applications of hydrogen transport membranes. The future of biphasic hydrogen transport membranes is prospected, particularly those of $BaCe_{0.65}Zr_{0.2}Y_{0.15}O_{3-\delta}$-$Ce_{0.85}Gd_{0.15}O_{2-\delta}$ composites.

Chapter 2 reports on the optimization of $BaCe_{0.65}Zr_{0.2}Y_{0.15}O_{3-\delta}$ material processing aiming towards an improved microstructure. With 0.5 wt.% NiO as sintering aid, single-phase $BaCe_{0.65}Zr_{0.2}Y_{0.15}O_{3-\delta}$ is obtained after 1500 °C / 5 h sintering, with density higher than 99 % and average grain size ~ 13 μm, without any secondary phase being observed.

The elemental distribution in the sintered large grain size $BaCe_{0.65}Zr_{0.2}Y_{0.15}O_{3-\delta}$ material is, for the first time, investigated using different complementary methods. Ni is distributed almost evenly in the material, and only a marginal Ni enrichment at the grain boundaries can be observed due to the imperfect nature of this mismatch region.

The mechanical properties of $BaCe_{0.65}Zr_{0.2}Y_{0.15}O_{3-\delta}$ are investigated in **Chapter 3** applying different micro and macroscale testing methods. Consistent values of the elastic modulus are determined on a larger range of tested volumes corroborating the validity of the determined values. The hardness values determined using different maximum loads do not show a dependence on the apparent indentation depth, which reflects the high quality and homogeneity of the tested material. The values of ~ 120 GPa for the elastic modulus and ~ 7 GPa for the hardness, respectively, are in a range typical of ceramic materials and comparable to the properties of similar materials used as transport membranes. The microscale intrinsic fracture toughness determined by micropillar splitting yields higher values than the Vickers indentation based analysis, which probes a larger volume of the material. A detailed microstructural analysis clearly reveals the effect of pores and crack deflection. The presence of a pore close to the surface of one of the pillars is likely responsible for the lower apparent fracture toughness value derived in this pillar splitting test. The Vickers indentation based apparent fracture toughness represents a rough estimate due to irregular crack patterns, bifurcation and delamination affecting the derived mesoscale values.

The high temperature compressive creep behavior of $BaCe_{0.65}Zr_{0.2}Y_{0.15}O_{3-\delta}$ in different atmospheres is studied in **Chapters 4**. From 850 °C to 1000 °C, in 4% H_2/Ar atmosphere, the stress exponent is ~ 3 and the activation energy ~ 160 kJ/mol, indicating a dislocation creep mechanism. For creep in the temperature range 1100 °C – 1200 °C, in air, the stress exponent is ~ 1 and the activation energy ~ 350 kJ/mol, suggesting a diffusional creep mechanism. At ~1000 °C, a change of the predominant creep mechanism is observed in air. Grain growth and densification during the creep tests can be ruled out on the basis of experimental evidence, which indicates that the observed deformation corresponds solely to the creep behavior. After the creep tests in both atmospheres, gaping grain boundaries are observed near the surfaces, while decomposition is only observed for the specimen that is tested in air. The oxygen partial pressure appears to be responsible for the observed decomposition rather than the temperature, which can be considered to be important for the technical application, since as a material candidate for H_2 permeation, $BaCe_{0.65}Zr_{0.2}Y_{0.15}O_{3-\delta}$ will not be exposed to oxygen under realistic application conditions.

The observed creep rate of $BaCe_{0.65}Zr_{0.2}Y_{0.15}O_{3-\delta}$ in 4% H_2/Ar at 850 °C is somewhat higher than the suggested critical compressive creep rate for commercial use of the membrane materials (1% per year). However, since the application temperature (~ 600 – 800 °C) is lower than the tested temperatures, an extrapolation of the creep rate of $BaCe_{0.65}Zr_{0.2}Y_{0.15}O_{3-\delta}$ to the application temperature can be made, which results in a creep rate close to the envisaged 1% per year. Therefore, for the design of reliable membrane components, the thermomechanical stability and in particular the creep behavior need to be considered.

Chapter 5 reports the material preparation and mechanical properties of $BaCe_{0.65}Zr_{0.2}Y_{0.15}O_{3-\delta}$-$Ce_{0.85}Gd_{0.15}O_{2-\delta}$ obtained using different indentation-based methods on a large range of tested volumes. The elastic modulus does not depend on the applied load and is determined to be ~ 170 GPa. The hardness decreases with increasing applied load, from ~ 9 GPa at loads lower than 200 mN to ~ 7 GPa at loads higher than 1 N, which might be due to the formation of radial/median cracks at higher loads.

The microscale intrinsic fracture toughness has been determined by micropillar splitting. Slice-by-slice FIB milling of tested pillars and a detailed microstructural investigation confirms that the two kinks in the load-depth curve indicate the partial split of the pillar and the splitting of the whole pillar, respectively. Thus, the fracture toughness of ~ 1.1 $MPa \cdot m^{0.5}$ represents the dual-phase $BaCe_{0.65}Zr_{0.2}Y_{0.15}O_{3-\delta}$-

$Ce_{0.85}Gd_{0.15}O_{2-\delta}$ intrinsic fracture toughness. Significant toughening associated effects due to crack deflections to avoid $Ce_{0.85}Gd_{0.15}O_{2-\delta}$ are observed.

The apparent fracture toughness is also estimated via the Vickers indentation based method. While it represents only a rough estimate, it can still be used as a means for comparison, in particular when evaluating similar types of material. Both methods confirm that the introduction of $Ce_{0.85}Gd_{0.15}O_{2-\delta}$ indeed significantly toughens the material, which can be a guide for further materials and component design.

In the end, **Chapter 6** reveals the overall conclusions and gives prospects for future research. It is concluded that the $BaCe_{0.65}Zr_{0.2}Y_{0.15}O_{3-\delta}$ membranes with high density and large grain size can be obtained using optimized powder preparation procedure and sintering profile. After introduction of $Ce_{0.85}Gd_{0.15}O_{2-\delta}$, the dual phase membranes with a constituent of 50 vol.% $BaCe_{0.65}Zr_{0.2}Y_{0.15}O_{3-\delta}$-50 vol.% $Ce_{0.85}Gd_{0.15}O_{2-\delta}$ is obtained with individual phases' being connected. This dual phase membranes show significantly improved elastic and plastic responses and fracture resistance compared with $BaCe_{0.65}Zr_{0.2}Y_{0.15}O_{3-\delta}$ membranes. Further improvements in mechanical resistance might be realized by multi-layer component structure. In addition, it appears necessary to study the mechanical stability of the membrane after a long period of operation.

SAMENVATTING

Twee-fase waterstof selectieve membranen, bestaande uit een protonen- en elektronengeleidende fase, vertonen potentieel interessante industriële toepassingen voor het verkrijgen van zeer zuiver waterstof, vanwege hun hoge mechanische, thermische en chemische stabiliteit onder extreme omstandigheden. Veelbelovende materialen voor dit type membranen zijn de waterstofion geleidende perovskiet fasen (b.v. $BaCe_{0.65}Zr_{0.2}Y_{0.15}O_{3-\delta}$) en de elektronen geleidende fluorietoxiden (b.v. $Ce_{0.85}Gd_{0.15}O_{2-\delta}$). De mechanische eigenschappen (b.v. elasticiteitsmodulus, hardheid, breuktaaiheid) van de membranen zijn belangrijke parameters voor een betrouwbare toepassing van deze materialen. De mechanische eigenschappen zijn nauw verbonden met microstructurele karakteristieken, zoals korrelgrootte, faseverdeling en defecten (bv. poriën en microscheurtjes). Deze relaties worden momenteel echter niet volledig begrepen. Daarom wordt in dit proefschrift de invloed van korrelgrootte, faseverdeling, poriën en microscheurtjes op de mechanische eigenschappen onderzocht voor éénfasige $BaCe_{0.65}Zr_{0.2}Y_{0.15}O_{3-\delta}$ en tweefasige $BaCe_{0.65}Zr_{0.2}Y_{0.15}O_{3-\delta}$-$Ce_{0.85}Gd_{0.15}O_{2-\delta}$ membranen. De materiaal bereiding (b.v. malen en sinteren) is geoptimaliseerd om het optimale keramische materiaal te verkrijgen. Verder worden de invloed van temperatuur en atmosfeer op het kruipgedrag besproken voor een $BaCe_{0.65}Zr_{0.2}Y_{0.15}O_{3-\delta}$ membraan.

Hoofdstuk 1 van dit proefschrift presenteert de mogelijke toepassingen en basisconcepten van waterstoftransportmembranen. Het mechanisme van waterstof transport, alsmede potentiële materiaalkandidaten worden hier behandeld. De veelbelovende vooruitzichten voor twee-fase waterstoftransport membranen worden weergegeven, met in het bijzonder die voor de $BaCe_{0.65}Zr_{0.2}Y_{0.15}O_{3-\delta}$-$Ce_{0.85}Gd_{0.15}O_{2-\delta}$ twee-fase composieten.

Hoofdstuk 2 rapporteert een optimale bereiding van $BaCe_{0.65}Zr_{0.2}Y_{0.15}O_{3-\delta}$ met het oog op een verbeterde microstructuur. Door toevoeging van 0,5 wt.% NiO als sinterhulpmiddel wordt éénfasig $BaCe_{0.65}Zr_{0.2}Y_{0.15}O_{3-\delta}$ > 99 % dicht materiaal met een gemiddelde korrelgrootte van ~ 13 µm verkregen na sinteren bij 1500 °C gedurende 5 uur, , zonder waargenomen tweede fase. De geleidbaarheid, in het bijzonder de korrelgrensgeleidbaarheid, van de bereide $BaCe_{0.65}Zr_{0.2}Y_{0.15}O_{3-\delta}$ wordt dus verondersteld niet beïnvloed te worden door de aanwezigheid van een tweede fase.

De element verdeling in het gesinterde $BaCe_{0.65}Zr_{0.2}Y_{0.15}O_{3-\delta}$ materiaal is, voor de eerste keer, onderzocht op verschillende lengteschalen. Nikkel verdeelde zich bijna gelijkmatig in het materiaal, en slechts een marginale nikkelverrijking op de korrelgrenzen kon worden waargenomen.

De mechanische eigenschappen van $BaCe_{0.65}Zr_{0.2}Y_{0.15}O_{3-\delta}$ worden beschreven in **Hoofdstuk 3**. Verschillende micro- en macroschaal testmethoden worden toegepast. Identieke waarden van de elasticiteitsmodulus worden gevonden op verschillende lengteschalen, hetgeen de validiteit van de bepaalde waarden bevestigt. De hardheid, bepaald met verschillende maximale belastingen, vertoont geen afhankelijkheid van de diepte, hetgeen de hoge kwaliteit en homogeniteit van het geteste materiaal weerspiegelt. De waarden van ongeveer 120 GPa en 7 GPa voor respectievelijk de elasticiteitsmodulus en de hardheid liggen in een bereik, dat typisch is voor keramische materialen en zijn vergelijkbaar met de eigenschappen van soortgelijke materialen die gebruikt worden als membranen. De intrinsieke breuktaaiheid op microscopische schaal, bepaald door het splitsen van micropilaren, levert hogere waarden op dan de analyses op basis van Vickers indentatie, welke laatste een groter volume van het materiaal bestrijkt. Een gedetailleerde microstructuur analyse laat duidelijk het bestaan van poriën en scheurafbuiging zien. De aanwezigheid van een porie dicht bij het oppervlak van één van de pilaren is waarschijnlijk verantwoordelijk voor de lagere breuktaaiheidswaarde die door de pilaar-splijtproef wordt verkregen. De schijnbare breuktaaiheid is een ruwe schatting vanwege onregelmatige scheurpatronen, scheursplitsing en delaminatie; factoren die de mesoschaal waarden beïnvloeden.

Het kruipgedrag van $BaCe_{0.65}Zr_{0.2}Y_{0.15}O_{3-\delta}$ als functie van de temperatuur en in verschillende gas atmosferen wordt beschreven in **Hoofdstuk 4**. Van 850 °C tot 1000 °C, in 4% H_2/Ar atmosfeer, is de spanningsexponent ~ 3 en de activeringsenergie ~ 160 kJ/mol, wat wijst op een dislocatie kruipmechanisme. Voor kruip in het temperatuurgebied 1100 - 1200 °C in lucht is de spanningsexponent ~ 1 en de activeringsenergie ~ 350 kJ/mol, wat overeenkomt met een diffusie kruipmechanisme. Bij ~1000 °C wordt in lucht een verandering van het overheersende kruipmechanisme waargenomen. Korrelgroei en verdichting tijdens de kruiptesten kunnen worden uitgesloten, wat erop wijst dat de waargenomen vervorming uitsluitend het kruipgedrag weergeeft. Na de kruiptesten in beide atmosferen worden open korrelgrenzen aan het oppervlak waargenomen, terwijl ontleding alleen wordt waargenomen bij het proefstuk dat in lucht wordt getest. De partiële zuurstofdruk is verantwoordelijk voor de waargenomen chemische degradatie en niet de temperatuur, wat belangrijk is voor de technische toepassing, aangezien $BaCe_{0.65}Zr_{0.2}Y_{0.15}O_{3-\delta}$ als materiaal onder experimentele (H_2-permeatie) omstandigheden niet aan zuurstof zal worden blootgesteld.

De waargenomen kruipsnelheid van $BaCe_{0.65}Zr_{0.2}Y_{0.15}O_{3-\delta}$ in 4% H_2/Ar bij 850 °C is iets hoger dan de kritische kruipsnelheid voor commercieel gebruik van de membraanmaterialen onder compressie (= 1% per jaar). Aangezien de toepassingstemperatuur (~ 600 - 800 °C) lager is dan de testtemperatuur, kan een ruwe extrapolatie van de kruipsnelheid van $BaCe_{0.65}Zr_{0.2}Y_{0.15}O_{3-\delta}$ naar de toepassingstemperatuur worden gemaakt, wat resulteert in een kruipsnelheid die dicht bij de beoogde 1% per jaar ligt. Daarom moet voor het ontwerp van betrouwbare membraancomponenten rekening worden gehouden met de thermomechanische stabiliteit en in het bijzonder met het kruipgedrag van het materiaal.

Hoofdstuk 5 beschrijft de materiaal bereiding en de mechanische eigenschappen van tweefasige $BaCe_{0.65}Zr_{0.2}Y_{0.15}O_{3-\delta}$-$Ce_{0.85}Gd_{0.15}O_{2-\delta}$ materialen. Ook hier zijn de mechanische eigenschappen bestudeerd met verschillende indentatie methoden op verschillende lengteschalen. De elasticiteitsmodulus is onafhankelijk van de toegepaste belasting en bedraagt ~ 170 GPa. De hardheid neemt af met toenemende indringdiepte, van ~ 9 GPa bij belastingen lager dan 200 mN tot ~ 7 GPa bij belastingen hoger dan 1 N, wat verklaard kan worden door de vorming van radiale/mediane scheuren bij hogere belastingen.

De intrinsieke breuktaaiheid op microschaal wordt bepaald door het splitsen van micro pilaren. Laag-voor laag FIB-frezen van de geteste pilaren en een gedetailleerd microstructuur onderzoek bevestigen dat de twee knikken in de belasting-diepte curve respectievelijk de gedeeltelijke splitsing van de pilaar en de splitsing van de volledige pilaar aangeven. Het tweefasige $BaCe_{0.65}Zr_{0.2}Y_{0.15}O_{3-\delta}$-$Ce_{0.85}Gd_{0.15}O_{2-\delta}$ heeft een intrinsieke breuktaaiheid van ~ 1,1 MPa-√m.. Significante vertaaiing als gevolg van scheurvervormingen om de $Ce_{0.85}Gd_{0.15}O_{2-\delta}$ korrels is waargenomen.

De schijnbare breuktaaiheid is ook bepaald via de Vickers indentatie methode. Hoewel via deze methode slechts een ruwe schatting verkregen word, kan het toch worden gebruikt als vergelijkingsmethode, met name bij de evaluatie van soortgelijke materiaalsoorten. Beide methoden (micro pilaar en Vickers indenter) bevestigen dat de toevoeging van $Ce_{0.85}Gd_{0.15}O_{2-\delta}$ het materiaal inderdaad aanzienlijk taaier maakt, wat een leidraad kan zijn voor verdere materiaal- en componentontwerpen.

Hoofdstuk 6 tenslotte geeft de algemene bevindingen weer van het werk, beschreven in dit proefschrift, en geeft perspectieven voor toekomstig onderzoek. Het blijkt dat de $BaCe_{0.65}Zr_{0.2}Y_{0.15}O_{3-\delta}$ membranen met hoge dichtheid en grote korrelgrootte worden verkregen door gebruik te maken van een geoptimaliseerde poederbereidingsprocedure en sinterprogramma. Na de introductie van $Ce_{0.85}Gd_{0.15}O_{2-\delta}$, wordt het twee-fase membraan verkregen met een samenstelling van 50 vol.% $BaCe_{0.65}Zr_{0.2}Y_{0.15}O_{3-\delta}$-50 vol.% $Ce_{0.85}Gd_{0.15}O_{2-\delta}$. Deze tweefasige membranen vertonen significant verbeterde elastische en plastische eigenschappen en een hogere breukweerstand in vergelijking met éénfasige $BaCe_{0.65}Zr_{0.2}Y_{0.15}O_{3-\delta}$ membranen. Verdere verbeteringen in de mechanische eigenschappen kunnen worden gerealiseerd door gebruik te maken van een meerlaagse componentstructuur. Bovendien is het noodzakelijk om de mechanische stabiliteit van het membraan na langdurig gebruik te onderzoeken.

CHAPTER 1

Introduction

1.1 Energy consumption

Global energy demand is increasing rapidly due to the rapid population growth and the advancement of civilization [1]. By 2050, global energy use is expected to increase nearly 50% compared with 2020 [2], as presented in Figure 1.1. Fossil fuels (coal, natural gas, petroleum and other liquids including biofuels) have, and will continue to, play a leading role in the global energy system for decades to come [2, 3]. They provide substantial economic benefits, but at the same time raise concerns about their environmental costs [4, 5]. As shown in the U.S. case in Figure 1.2, over 70% greenhouse gas emissions result from fossil fuel combustion carbon dioxide (CO_2) [6], which is commonly recognized critical for global warming [7, 8]. To reduce the greenhouse gas emission and slow the global warming, Kyoto Protocol [9] and Paris Agreement [10] were signed globally for the transformation of energy production towards clean and renewable.

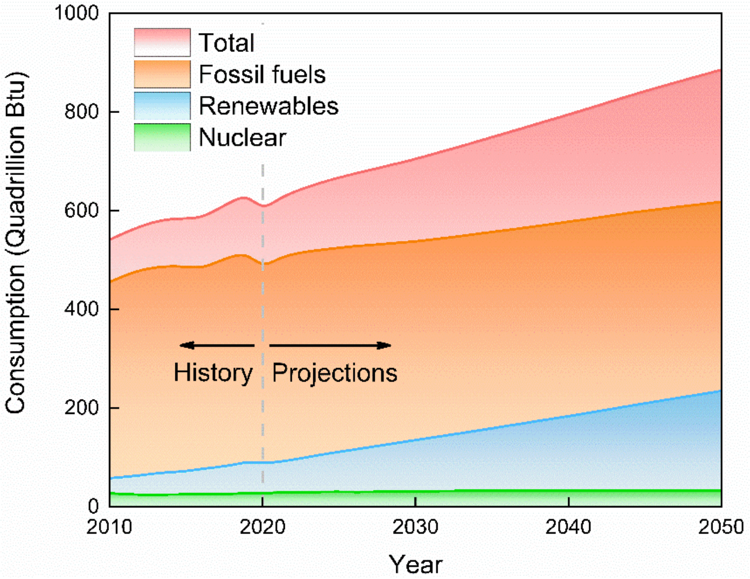

Figure 1.1 Global energy consumption. Data obtained from U.S. Energy Information Administration [2].

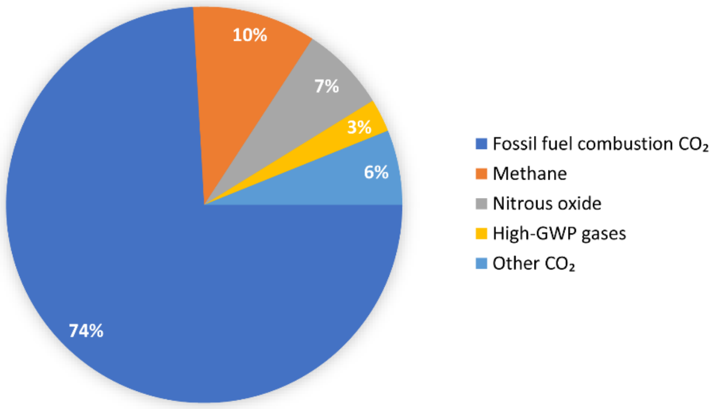

Figure 1.2 U.S. greenhouse gas emissions in 2019. Data obtained from U.S. Energy Information Administration [6].

With the support from economic and policy mechanisms, the market for clean and renewable energy systems is developing rapidly [11]. However, most renewable energy sources are intermittent and volatile and therefore require the development of efficient media for energy storage [12]. Hydrogen, as clean energy and a promising energy carrier [13], has gaining increasing amount of attention.

1.2 Hydrogen production technologies

Hydrogen (H_2) is the lightest element on the earth and it can be used as an energy carrier rather than an energy source [14]. H_2 can store and provide energy, but it does not normally exist naturally in large quantities in the earth's natural environment and must therefore be generated from the compounds that contain it [15].

Hydrogen can be produced through low-carbon pathways using diverse resources [16]. Thermo-chemical processes utilize chemical reactions and heat to release H_2 from organic compounds, including fossil fuels and biomass [17]. Electrolytic processes use electricity or solar energy to split water into hydrogen and oxygen [18]. Biological processes use sunlight or organic matter to produce hydrogen with help of microorganisms such as bacteria and algae [19].

In the mid- and long-term, electrolysis and biological pathways are anticipated to reach the cost targets and become viable [20]. Nowadays, most of the world's hydrogen is generated from natural gas via steam methane reforming (SMR) [21], as presented in Figure 1.3.

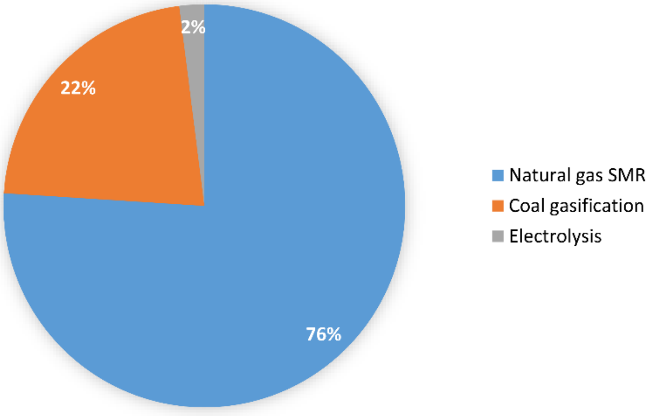

Figure 1.3 Global H_2 production in 2020. Data adapted from U.S. Department of Energy [21].

The SMR process is heavily endothermic, governed by equilibrium, and requires subsequent H_2 separation procedures [22]. Therefore, it's very crucial to develop H_2 separation technologies to separate H_2 from by-products.

1.3 Hydrogen separation membranes

Ceramic protonic-electronic conducting membranes are promised materials due to their tremendous advantage of 100% selectivity for H_2, hence, ruling out the need for subsequent purification procedures and saving the costs. [23]. In addition, they can be integrated directly into reforming or gasification reactors [24]. Without an exterior power input, both protons and electrons diffuse across the membrane utilising the H2 partial pressure gradient as a driving force at application temperatures [25]. The mechanism of H_2 separation and the membrane materials are discussed respectively in sections 1.3.1 and 1.3.2.

1.3.1 Mechanism of hydrogen separation

When hydrogen partial pressure (P_{H_2}) gradient is applied across the membrane at elevated temperatures (typically 300-900 °C), the hydrogen permeation procedure begins with 3 main stages: gas-solid surface exchange at the high P_{H_2} side, ambipolar diffusion of the charge carrier through the hydrogen permeation membrane, and solid-gas surface exchange at the low P_{H_2} side.

For surface exchange at high P_{H_2} side, multiple steps take place: hydrogen adsorption, hydrogen dissociation, incorporation of dissociated hydrogen ions into the membrane lattice forming the hydroxide defects, which is expressed (using Kröger-Vink notation) in equation (1.1) [26]. Accordingly, the inverse form of the equation (1.1) can stand for what happens at low P_{H_2} side, as exemplified by equation (1.2).

$$H_2 + 2O_O^x \rightarrow 2OH_O^\bullet + 2e' \tag{1.1}$$

$$2OH_O^\bullet + 2e' \rightarrow H_2 + 2O_O^x \tag{1.2}$$

where O_O is the oxygen ion on an oxygen lattice site and OH_O a hydroxide defect on an oxygen lattice site. Superscripts x, $\bullet$ and $'$ denote electroneutral state, one positive and one negative charge.

When hydrogen ions and electrons are considered as charge carriers and no diffusion path for hydrogen ions is addressed, the overall reaction associated with the exchange of hydrogen on both sides can be simplified by equation (1.3) and equation (1.4) [23].

$$H_2 \rightarrow 2H^+ + 2e^- \tag{1.3}$$

$$2H^+ + 2e^- \rightarrow H_2 \tag{1.4}$$

Figure 1.4 illustrates schematically the ambipolar diffusion through the membrane. Driven by the P_{H_2} gradient between the membrane 2 sides, pure H_2 is separated from a hydrogen-containing gas mixture by allowing hydrogen ions and electrons flow (same direction) through membrane.

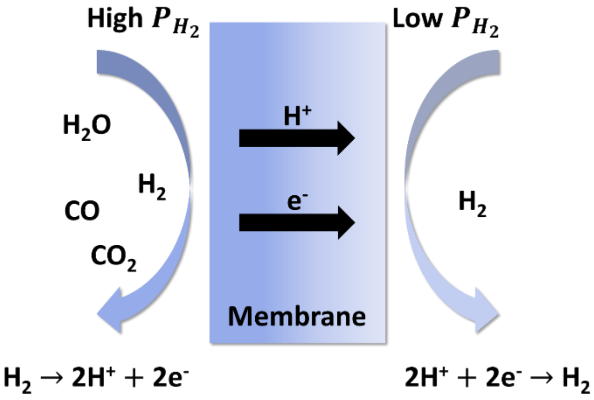

Figure 1.4 Schematic of hydrogen separation process through ceramic protonic-electronic conducing membrane.

The overall hydrogen separation process is governed by the slowest stage. Assuming bulk diffusion is the sole rate-limited process, the hydrogen flux across the membrane may be depicted by the Wagner formula [27]:

$$j_{H^+} = \frac{-RT}{2F^2L} \int_{I}^{II} \sigma_{amb} \, d \, ln \, P_{H_2} \tag{1.5}$$

where R - gas constant, T - temperature, F - Faraday constant, L - thickness of the membrane, I and II represent two sides of the membrane and σ_{amb} is the ambipolar conductivity.

The hydrogen flux through a mixed conducting material thus depends on three groups of factors: the operating conditions, the material properties (protonic and electronic conductivity) and the material thickness.

1.3.2 Membrane materials

According to the phase constituents for ambipolar diffusion of hydrogen ions and electrons, there are two groups of membrane materials: single-phase and dual-phase membranes [28], demonstrated in Figure 1.5. Single-phase membranes utilise just one phase to achieve mixed proton-electron conductivity (Figure 1.5(a)). Biphasic membranes use 2 phases to attain mixed proton-electron conductivity (Figure 1.5(b)), with each phase providing either proton or electron conductivity.

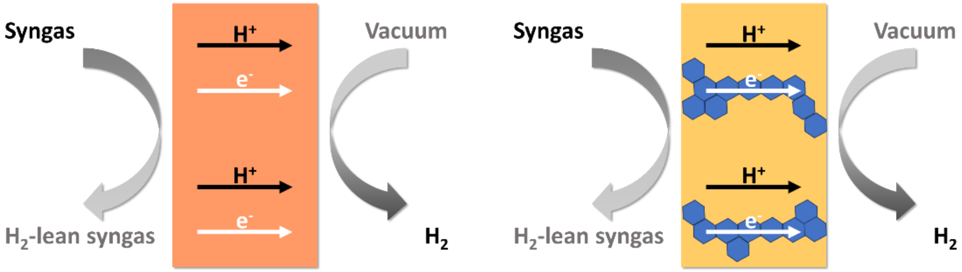

Figure 1.5 Schematics demonstrating (a) single-phase membrane and (b) dual-phase membrane for hydrogen transport. The hexagons, in (b), represent the electron conducting phase, surrounded by the proton conducting phase.

Single phase membranes

The existence of protonic defects in wide band gap oxides at elevated temperatures has been well established since the work of Stoltz and Wagner in 1966 [29]. Over a decade later, a systematic study on acceptor-doped perovskite-type oxides, e.g. $LaAlO_3$, $LaYO_3$ and $SrZrO_3$, provided experimental evidence indicating that these materials might be prototype conductors in a H_2-containing atmosphere [30], although the conductivity observed was fairly low.

Among the oxide proton conductors investigated so far, $SrCeO_3$ or $BaCeO_3$ based materials, in which some aliovalent rare earth cations partially substitute cerium, exhibit already decent protonic conductivity under a H_2-containing atmosphere in the 400 °C - 800 °C temperature range [31, 32]. Protonic conductors based on $BaCeO_3$ show the greatest conductivity of any conductor in this class [33]. However, the lack of chemical stability under operational conditions remains a concern for many applications [34], i.e. elevated temperatures and with other species present such as CO_2, H_2O. Conversely, $BaZrO_3$ based protonic conductors exhibit higher chemical stability but rather low conductivity due to difficulty to fabricate dense samples [33, 35]. Y-doped $BaCe_{1-x}Zr_xO_{3-\delta}$ (BCZY) perovskite oxides incorporates both high proton conductivity and improved chemical resistance to CO_2 and H_2O [36-40], which are thus considered as promising proton conducting materials. Nevertheless, the poor electronic conductivity limits the ambipolar conductivity, as a result, the permeation of H_2 through the membrane being reduced or even excluded [40-42]. It has been suggested that a further doping on the B-site of the ABO_3 perovskite could be a strategy to enhance the electronic conductivity but will be detrimental to the protonic transport [24]; another promising option is the introduction of an electronic conducting secondary phase forming hence a dual-phase composite [43].

Dual phase membranes

Biphasic membrane consisting of a proton-conducting phase and an electron-conducting phase (see Figure 1.5 (b)). In this context, ceramic-metal (cer-met) composite membranes have been investigated in detail [44-49], however, all-ceramic (cer-cer) systems demonstrated already significant advantages regarding mechanical and chemical stability [50-57].

Rare earth doped ceria is known for its outstanding electron conductivity in reducing atmospheres at temperatures above 600 °C due to the reduction of Ce^{4+} to Ce^{3+} [58-60]. The hydrogen separation process (see Figure 1.4) related temperature and atmosphere requirements are fulfilled by their electronic conductivity. Besides that, the incorporation of doped ceria as electron conducting phase is expected to enhance the application relevant thermomechanical resistance of cerate materials (e.g. $BaCeO_3$ based protonic conductors) to CO_2 and H_2O in the all-ceramic composites, as it changes the equilibrium of the degradation reaction of the protonic conductor towards the reactant side thus preserving the desired proton conducting phase [61, 62].

In a nutshell, the critical advantage of biphasic membranes over monophasic membranes is the enhanced ambipolar conductivity in reducing environments (e.g. H_2 containing syngas).

Promising material candidates for hydrogen separation

Biphasic membranes should have more promising potential than single-phase perovskite membranes for hydrogen separation. One promising candidate material, specifically developed towards hydrogen separation, is the $BaCe_{0.65}Zr_{0.2}Y_{0.15}O_{3-\delta}$-$Ce_{0.85}Gd_{0.15}O_{2-\delta}$ (BCZ20Y15-GDC15) membrane material, which consists of a BCZ20Y15 perovskite phase to be the proton conducting phase, and a GDC15 phase as the electron conducting phase [43]. The composition 50 vol.% BCZ20Y15 - 50 vol.% GDC15, being above the percolation limit, possesses exceptional hydrogen permeation [43], enhanced sulfur tolerance [62] and structural stability [63, 64], which indicates its potential for application. In order to reduce the cost of hydrogen separation, it is essential to develop simple, efficient and economical synthetic approaches, such as solid-state reactive sintering, to scale up the hydrogen separation membranes production [65].

1.4 Scope of the thesis

Despite the progress with respect to conductivity and chemical stability, only few studies focused on mechanical properties of all ceramic biphasic gas transport membranes [66-72] and, to the best of the author's knowledge, no systematic study exists focusing on mechanical properties of single-phase $BaCe_{0.65}Zr_{0.2}Y_{0.15}O_{3-\delta}$ membranes or dual phase $BaCe_{0.65}Zr_{0.2}Y_{0.15}O_{3-\delta}$-$Ce_{0.85}Gd_{0.15}O_{2-\delta}$ membranes.

The thesis contains a concise research framework on single phase $BaCe_{0.65}Zr_{0.2}Y_{0.15}O_{3-\delta}$ membranes and dual phase $BaCe_{0.65}Zr_{0.2}Y_{0.15}O_{3-\delta}$-$Ce_{0.85}Gd_{0.15}O_{2-\delta}$ membranes prepared by solid-state reactive sintering using $BaCO_3$, CeO_2, ZrO_2, Y_2O_3 and Gd_2O_3 as starting materials. The purpose of this work is to investigate their thermo-mechanical properties via different length-scale methods to understand the mechanisms behind the properties. The microstructure characterization and the phase composition are analysed in detail for the sintered membranes. Their effects on thermo-mechanical properties (i.e. elastic modulus, hardness, fracture toughness and creep) are discussed. Elastic modulus and hardness represent the elastic and plastic responses of the material under the applied load, which can be fundamental parameters for finite elemental method (FEM) simulation. Fracture toughness represents the energy that can be absorbed by the material during the crack propagation, which indicates the material fracture resistance. Creep behaviour benefit the analysis of the material long-term structural stability in different atmospheres under elevated temperatures.

In **Chapter 2**, the preparation method of $BaCe_{0.65}Zr_{0.2}Y_{0.15}O_{3-\delta}$ is optimized, with 0.5 wt.% NiO as sintering aid, to improve the microstructure with respect to application relevant boundary conditions. High density single phase $BaCe_{0.65}Zr_{0.2}Y_{0.15}O_{3-\delta}$ material with large grain size is obtained. The distribution of Ni in the sintered material is studied at various length scales via different methods.

In **Chapter 3**, the mechanical properties of $BaCe_{0.65}Zr_{0.2}Y_{0.15}O_{3-\delta}$ are determined on different length scales using different methods including impulse excitation, indentation testing, and micro-pillar splitting. A detailed microstructural analysis of pillars reveals that irregular results are caused by pores causing crack deflection and complex crack patterns.

In **Chapter 4**, the elevated temperature compressive creep behavior of $BaCe_{0.65}Zr_{0.2}Y_{0.15}O_{3-\delta}$ in the temperature regime of 850 °C to 1200 °C is studied in both air and 4% H_2/Ar as a function of the applied stress. The results indicate different creep mechanisms depending on atmosphere and temperature range. While dislocation creep is observed in 4% H_2/Ar over the full range, a dislocation creep mechanism is observed in air at temperatures $\leq$ 1050 °C and a diffusional creep mechanism at temperature $\geq$ 1100 °C. A detailed microstructural analysis of the post-creep test specimens reveals that being exposed in oxygen results in local stoichiometry variations and decomposition on the surface.

In **Chapter 5**, $BaCe_{0.65}Zr_{0.2}Y_{0.15}O_{3-\delta}$-$Ce_{0.85}Gd_{0.15}O_{2-\delta}$ dual-phase material is prepared via solid-state reactive sintering method. After phase constituents and microstructural characterizations, mechanical properties are investigated to evaluate the mechanical behavior and develop strategies to warrant structural stability. Elastic modulus, hardness and fracture toughness values are studied using different indentation-based methods. The fracture experiments at different length-scales both reveal that the introduction of GDC15 makes the material significantly tougher, facilitating the design of robust and reliable components.

In the end, **Chapter 6** concludes by reflecting on the significance of the overall research findings and offering suggestions for further study.

References

[1] M.A. Abdelkareem, K. Elsaid, T. Wilberforce, M. Kamil, E.T. Sayed, A. Olabi, Environmental aspects of fuel cells: A review, Science of The Total Environment 752 (2021) 141803.

[2] International Energy Outlook 2021 (IEO2021), U.S. Energy Information Administration (EIA), Washington, DC, USA (2021).

[3] N. Abas, A. Kalair, N. Khan, Review of fossil fuels and future energy technologies, Futures 69 (2015) 31-49.

[4] M.I. Hoffert, Farewell to fossil fuels?, Science 329(5997) (2010) 1292-1294.

[5] T. Covert, M. Greenstone, C.R. Knittel, Will we ever stop using fossil fuels?, Journal of Economic Perspectives 30(1) (2016) 117-38.

[6] U.S. greenhouse gas emissions by gas, U.S. Energy Information Administration (EIA), Washington, DC, USA (2019).

[7] V. Ramanathan, Y. Feng, Air pollution, greenhouse gases and climate change: Global and regional perspectives, Atmospheric environment 43(1) (2009) 37-50.

[8] J.G. Olivier, J.A. Peters, G. Janssens-Maenhout, Trends in global CO_2 emissions. 2012 report, (2012).

[9] C. Böhringer, The Kyoto protocol: a review and perspectives, Oxford Review of Economic Policy 19(3) (2003) 451-466.

[10] R. Falkner, The Paris Agreement and the new logic of international climate politics, International Affairs 92(5) (2016) 1107-1125.

[11] O. Ellabban, H. Abu-Rub, F. Blaabjerg, Renewable energy resources: Current status, future prospects and their enabling technology, Renewable and sustainable energy reviews 39 (2014) 748-764.

[12] I. Dincer, C. Acar, A review on clean energy solutions for better sustainability, International Journal of Energy Research 39(5) (2015) 585-606.

[13] K.T. Møller, T.R. Jensen, E. Akiba, H.-w. Li, Hydrogen-A sustainable energy carrier, Progress in Natural Science: Materials International 27(1) (2017) 34-40.

[14] K. Mazloomi, C. Gomes, Hydrogen as an energy carrier: Prospects and challenges, Renewable and Sustainable Energy Reviews 16(5) (2012) 3024-3033.

[15] J.D. Holladay, J. Hu, D.L. King, Y. Wang, An overview of hydrogen production technologies, Catalysis today 139(4) (2009) 244-260.

[16] P. Nikolaidis, A. Poullikkas, A comparative overview of hydrogen production processes, Renewable and sustainable energy reviews 67 (2017) 597-611.

[17] J.A. Turner, Sustainable hydrogen production, Science 305(5686) (2004) 972-974.

[18] J. Turner, G. Sverdrup, M.K. Mann, P.C. Maness, B. Kroposki, M. Ghirardi, R.J. Evans, D. Blake, Renewable hydrogen production, International journal of energy research 32(5) (2008) 379-407.

[19] D. Das, T.N. Veziroğlu, Hydrogen production by biological processes: a survey of literature, International journal of hydrogen energy 26(1) (2001) 13-28.

[20] F. Dawood, M. Anda, G. Shafiullah, Hydrogen production for energy: An overview, International Journal of Hydrogen Energy 45(7) (2020) 3847-3869.

[21] Global Production of Hydrogen, U.S. Department of Energy, Washington, DC, USA (2020).

[22] L. Barelli, G. Bidini, F. Gallorini, S. Servili, Hydrogen production through sorption-enhanced steam methane reforming and membrane technology: a review, Energy 33(4) (2008) 554-570.
[23] J. Phair, S. Badwal, Review of proton conductors for hydrogen separation, Ionics 12(2) (2006) 103-115.
[24] T. Norby, R. Haugsrud, Dense ceramic membranes for hydrogen separation, Wiley-VCH Verlag: Weinheim2006.
[25] K.-D. Kreuer, Proton conductivity: materials and applications, Chemistry of materials 8(3) (1996) 610-641.
[26] D. Thomas, J. Lander, Hydrogen as a donor in zinc oxide, The Journal of Chemical Physics 25(6) (1956) 1136-1142.
[27] A.F. Sammells, M.V. Mundschau, Nonporous inorganic membranes: for chemical processing, John Wiley & Sons2006.
[28] X. Zhu, W. Yang, Mixed conducting ceramic membranes, Green Chemistry and Sustainable Technology (2017).
[29] S. Stotz, C. Wagner, Die löslichkeit von wasserdampf und wasserstoff in festen oxiden, Berichte der Bunsengesellschaft für physikalische Chemie 70(8) (1966) 781-788.
[30] I.H. Takahashi T, Rev. Chim. Mine´r. (t17) (1980) 243.
[31] H. Iwahara, H. Uchida, S. Tanaka, High temperature type proton conductor based on SrCeO3 and its application to solid electrolyte fuel cells, Solid State Ionics 9 (1983) 1021-1025.
[32] H. Iwahara, H. Uchida, K. Ono, K. Ogaki, Proton conduction in sintered oxides based on BaCeO3, Journal of the Electrochemical Society 135(2) (1988) 529-533.
[33] K. Kreuer, Proton-conducting oxides, Annual Review of Materials Research 33(1) (2003) 333-359.
[34] S.V. Bhide, A.V. Virkar, Stability of BaCeO3-based proton conductors in water-containing atmospheres, Journal of The Electrochemical Society 146(6) (1999) 2038-2044.
[35] P. Babilo, T. Uda, S.M. Haile, Processing of yttrium-doped barium zirconate for high proton conductivity, Journal of materials research 22(5) (2007) 1322-1330.
[36] E. Fabbri, A. D'Epifanio, E. Di Bartolomeo, S. Licoccia, E. Traversa, Tailoring the chemical stability of $Ba(Ce_{0.8-x}Zr_x)Y_{0.2}O_{3-\delta}$ protonic conductors for intermediate temperature solid oxide fuel cells (IT-SOFCs), Solid State Ionics 179(15-16) (2008) 558-564.
[37] A. Magrez, T. Schober, Preparation, sintering, and water incorporation of proton conducting $Ba_{0.99}Zr_{0.8}Y_{0.2}O_{3-\delta}$: comparison between three different synthesis techniques, Solid State Ionics 175(1-4) (2004) 585-588.
[38] S. Tao, J.T. Irvine, Conductivity studies of dense yttrium-doped $BaZrO_3$ sintered at 1325 C, Journal of Solid State Chemistry 180(12) (2007) 3493-3503.
[39] J. Li, J.-L. Luo, K.T. Chuang, A.R. Sanger, Chemical stability of Y-doped Ba (Ce, Zr) O_3 perovskites in H2S-containing H2, Electrochimica Acta 53(10) (2008) 3701-3707.
[40] K.H. Ryu, S.M. Haile, Chemical stability and proton conductivity of doped $BaCeO_3$–$BaZrO_3$ solid solutions, Solid State Ionics 125(1-4) (1999) 355-367.
[41] S. Barison, M. Battagliarin, T. Cavallin, L. Doubova, M. Fabrizio, C. Mortalo, S. Boldrini, L. Malavasi, R. Gerbasi, High conductivity and chemical stability of $BaCe_{1-x-y}Zr_x Y_yO_{3-\delta}$ proton conductors prepared by a sol–gel method, Journal of Materials Chemistry 18(42) (2008) 5120-5128.
[42] S. Barison, M. Battagliarin, T. Cavallin, S. Daolio, L. Doubova, M. Fabrizio, C. Mortalo, S. Boldrini, R. Gerbasi, Barium Non-Stoichiometry Role on the Properties of $Ba_{1+x}Ce_{0.65}Zr_{0.20}Y_{0.15}O_{3-\delta}$ Proton Conductors for IT-SOFCs, Fuel cells 8(5) (2008) 360-368.

[43] E. Rebollo, C. Mortalo, S. Escolástico, S. Boldrini, S. Barison, J.M. Serra, M. Fabrizio, Exceptional hydrogen permeation of all-ceramic composite robust membranes based on $BaCe_{0.65}Zr_{0.20}Y_{0.15}O_{3-\delta}$ and Y-or Gd-doped ceria, Energy & Environmental Science 8(12) (2015) 3675-3686.

[44] H. Kim, B. Kim, J. Lee, K. Ahn, H.-R. Kim, K.J. Yoon, B.-K. Kim, Y.W. Cho, H.-W. Lee, J.-H. Lee, Microstructural adjustment of Ni–$BaCe_{0.9}Y_{0.1}O_{3-\delta}$ cermet membrane for improved hydrogen permeation, Ceramics International 40(3) (2014) 4117-4126.

[45] S. Fang, K.S. Brinkman, F. Chen, Hydrogen permeability and chemical stability of Ni–$BaZr_{0.1}Ce_{0.7}Y_{0.1}Yb_{0.1}O_{3-\delta}$ membrane in concentrated H_2O and CO_2, Journal of membrane science 467 (2014) 85-92.

[46] Z. Zhu, W. Sun, L. Yan, W. Liu, W. Liu, Synthesis and hydrogen permeation of Ni–Ba $(Zr_{0.1}Ce_{0.7}Y_{0.2})O_{3-\delta}$ metal–ceramic asymmetric membranes, International journal of hydrogen energy 36(10) (2011) 6337-6342.

[47] S. Fang, L. Bi, C. Yang, L. Yan, C. Chen, W. Liu, H_2S poisoning and regeneration of Ni–$BaZr_{0.1}Ce_{0.7}Y_{0.2}O_{3-\delta}$ at intermediate temperature, Journal of alloys and compounds 475(1-2) (2009) 935-939.

[48] C. Zuo, T. Lee, S. Dorris, U. Balachandran, M. Liu, Composite Ni–Ba $(Zr_{0.1}Ce_{0.7}Y_{0.2})O_3$ membrane for hydrogen separation, Journal of Power Sources 159(2) (2006) 1291-1295.

[49] C. Zuo, S. Dorris, U. Balachandran, M. Liu, Effect of Zr-doping on the chemical stability and hydrogen permeation of the Ni−$BaCe_{0.8}Y_{0.2}O_{3-\alpha}$ mixed protonic−electronic conductor, Chemistry of materials 18(19) (2006) 4647-4650.

[50] W.A. Rosensteel, S. Ricote, N.P. Sullivan, Hydrogen permeation through dense $BaCe_{0.8}Y_{0.2}O_{3\text{-delta}}$-$Ce_{0.8}Y_{0.2}O_{2\text{-delta}}$ composite-ceramic hydrogen separation membranes, International Journal of Hydrogen Energy 41(4) (2016) 2598-2606.

[51] W.A. Rosensteel, N.P. Sullivan, Fabrication and hydrogen permeation through novel $BaZr_{0.9}Y_{0.1}O_{3-\delta}$–Cu composite ceramic-metallic membranes, International Journal of Hydrogen Energy 42(7) (2017) 4216-4223.

[52] Y. Wei, J. Xue, W. Fang, Y. Chen, H. Wang, J. Caro, Enhanced stability of Zr-doped $Ba(CeTb)O_{3-\delta}$-Ni cermet membrane for hydrogen separation, Chemical Communications 51(58) (2015) 11619-11621.

[53] S. Escolastico, C. Solis, C. Kjølseth, J. Serra, Outstanding hydrogen permeation through CO_2-stable dual-phase ceramic membranes, Energy & Environmental Science 7(11) (2014) 3736-3746.

[54] J.M. Polfus, Z. Li, W. Xing, M.F. Sunding, J.C. Walmsley, M.-L. Fontaine, P.P. Henriksen, R. Bredesen, Chemical stability and H2 flux degradation of cercer membranes based on lanthanum tungstate and lanthanum chromite, Journal of Membrane Science 503 (2016) 42-47.

[55] J.S. Fish, S. Ricote, F. Lenrick, L.R. Wallenberg, T.C. Holgate, R. O'Hayre, N. Bonanos, Synthesis by spark plasma sintering of a novel protonic/electronic conductor composite: $BaCe_{0.2}Zr_{0.7}Y_{0.1}O_{3-\delta}/Sr_{0.95}Ti_{0.9}Nb_{0.1}O_{3-\delta}$ (BCZY27/STN95), Journal of Materials Science 48(18) (2013) 6177-6185.

[56] D. Montaleone, E. Mercadelli, A. Gondolini, P. Pinasco, A. Sanson, On the compatibility of dual phase $BaCe_{0.65}Zr_{0.2}Y_{0.15}O_3$-based membrane for hydrogen separation application, Ceramics International 43(13) (2017) 10151-10157.

[57] E. Mercadelli, D. Montaleone, A. Gondolini, P. Pinasco, A. Sanson, Tape-cast asymmetric membranes for hydrogen separation, Ceramics International 43(11) (2017) 8010-8017.

[58] M. Mogensen, N.M. Sammes, G.A. Tompsett, Physical, chemical and electrochemical properties of pure and doped ceria, Solid State Ionics 129(1-4) (2000) 63-94.

[59] Y. Xiong, K. Yamaji, T. Horita, N. Sakai, H. Yokokawa, Electronic Conductivity of 20 mol% $YO_{1.5}$ doped CeO_2, Journal of the Electrochemical Society 149(11) (2002) E450.

[60] J.B. Goodenough, Oxide-ion electrolytes, Annual review of materials research 33(1) (2003) 91-128.

[61] D. Lin, Q. Wang, K. Peng, L.L. Shaw, Phase formation and properties of composite electrolyte $BaCe_{0.8}Y_{0.2}O_{3-\delta}$–$Ce_{0.8}Gd_{0.2}O_{1.9}$ for intermediate temperature solid oxide fuel cells, Journal of Power Sources 205 (2012) 100-107.

[62] C. Mortalò, E. Rebollo, S. Escolástico, S. Deambrosis, K. Haas-Santo, M. Rancan, R. Dittmeyer, L. Armelao, M. Fabrizio, Enhanced sulfur tolerance of $BaCe_{0.65}Zr_{0.20}Y_{0.15}O_{3-\delta}$-$Ce_{0.85}Gd_{0.15}O_{2-\delta}$ composite for hydrogen separation membranes, Journal of Membrane Science 564 (2018) 123-132.

[63] C. Mortalò, A. Santoru, C. Pistidda, E. Rebollo, M. Boaro, C. Leonelli, M. Fabrizio, Structural evolution of $BaCe_{0.65}Zr_{0.20}Y_{0.15}O_{3-\delta}$-$Ce_{0.85}Gd_{0.15}O_{2-\delta}$ composite MPEC membrane by in-situ synchrotron XRD analyses, Materials Today Energy 13 (2019) 331-341.

[64] C. Mortalò, M. Boaro, E. Rebollo, V. Zin, E. Aneggi, M. Fabrizio, A. Trovarelli, Insights on the Interfacial Processes Involved in the Mechanical and Redox Stability of the $BaCe_{0.65}Zr_{0.20}Y_{0.15}O_{3-\delta}$–$Ce_{0.85}Gd_{0.15}O_{2-\delta}$ Composite, ACS Applied Energy Materials 3(10) (2020) 9877-9888.

[65] J. Zhu, G. Zhang, G. Liu, Z. Liu, W. Jin, N. Xu, Perovskite hollow fibers with precisely controlled cation stoichiometry via one-step thermal processing, Advanced Materials 29(18) (2017) 1606377.

[66] F. Zeng, J. Malzbender, S. Baumann, W. Zhou, M. Ziegner, A. Nijmeijer, O. Guillon, R. Schwaiger, W.A. Meulenberg, Mechanical reliability of $Ce_{0.8}Gd_{0.2}O_{2-\delta}$-$FeCo_2O_4$ dual phase membranes synthesized by one-step solid-state reaction, Journal of the American Ceramic Society 104(4) (2021) 1814-1830.

[67] F. Zeng, J. Malzbender, S. Baumann, F. Schulze-Küppers, M. Krüger, A. Nijmeijer, O. Guillon, W.A. Meulenberg, Micromechanical Characterization of $Ce_{0.8}Gd_{0.2}O_{2-\delta}$–$FeCo_2O_4$ Dual Phase Oxygen Transport Membranes, Advanced engineering materials 22(6) (2020) 1901558.

[68] F. Zeng, J. Malzbender, S. Baumann, A. Nijmeijer, L. Winnubst, O. Guillon, R. Schwaiger, W.A. Meulenberg, Residual stress and mechanical strength of $Ce_{0.8}Gd_{0.2}O_{2-\delta}$-$FeCo_2O_4$ dual phase oxygen transport membranes, Journal of the European Ceramic Society (2021).

[69] F. Zeng, J. Malzbender, S. Baumann, A. Nijmeijer, L. Winnubst, M. Ziegner, O. Guillon, R. Schwaiger, W.A. Meulenberg, Optimization of sintering conditions for improved microstructural and mechanical properties of dense $Ce_{0.8}Gd_{0.2}O_{2-\delta}$-$FeCo_2O_4$ oxygen transport membranes, Journal of the European Ceramic Society 41(1) (2021) 509-516.

[70] T. Nithyanantham, S. Biswas, N. Nagendra, S. Bandopadhyay, Studies on mechanical behavior of LSFT-CGO dual-phase membranes at elevated temperatures in ambient air and slightly reducing environments, Ceramics International 40(6) (2014) 7783-7790.

[71] S. Kim, S.H. Kim, K.S. Lee, J.H. Yu, Y.-H. Seong, I.S. Han, Mechanical properties of LSCF ($La_{0.6}Sr_{0.4}Co_{0.2}Fe_{0.8}O_{3-\delta}$)–GDC ($Ce_{0.9}Gd_{0.1}O_{2-\delta}$) for oxygen transport membranes, Ceramics International 43(2) (2017) 1916-1921.

[72] K. Raju, S. Kim, C.J. Hyung, J.H. Yu, Y.-H. Seong, S.-H. Kim, I.-S. Han, Optimal sintering temperature for $Ce_{0.9}Gd_{0.1}O_{2-\delta}$–$La_{0.6}Sr_{0.4}Co_{0.2}Fe_{0.8}O_{3-\delta}$ composites evaluated

through their microstructural, mechanical and elastic properties, Ceramics International 45(1) (2019) 1460-1463.

CHAPTER 2

Promoting densification and grain growth of $BaCe_{0.65}Zr_{0.2}Y_{0.15}O_{3-\delta}$ at 1500 °C with a low amount of NiO as sintering aid

Abstract

$BaCe_{0.65}Zr_{0.2}Y_{0.15}O_{3-\delta}$ (BCZ20Y15) has raised great interest due to its good protonic conductivity and chemical stability. However, the sintering of the material is considerably challenged by its refractory nature. In the current work, almost fully densified single-phase BCZ20Y15 with grain sizes exceeding 10 µm is successfully fabricated by sintering at 1500 °C by using calcinated powders consisting of naturally separated perovskite phases and 0.5 wt.% NiO. Global and local chemistry of the sintered material are studied by Inductively Coupled Plasma Optical Emission Spectroscopy (ICP-OES) and Atom Probe Tomography (APT) methods, respectively. Furthermore, the mechanism leading to the promoted densification and grain growth is elucidated based on current experimental results and a comprehensive review of literature studies.

This chapter will be submitted to Chemistry of Materials in June 2022.

2.1 Introduction

$BaCeO_3$-based materials have raised considerable interest due to their high protonic conductivity [1-6], in particular when doped with 15% Y [7, 8]. Additional doping with more than 20% Zr enhances the chemical tolerance against atmospheres containing CO_2, H_2O, and/or H_2S [9-13]. Hence, Y and Zr co-doped $BaCeO_3$ compounds, e.g. $BaCe_{0.65}Zr_{0.2}Y_{0.15}O_{3-\delta}$ (BCZ20Y15), have been developed and proved to be promising candidates for applications as membranes for hydrogen separation and electrolytes for intermediate-temperature solid oxide fuel cells [14-17]. In particular, BCZ20Y15 shows remarkably high H_2 permeance when combined with Gd-doped CeO_2 forming a dual-phase composite [17].

However, the Zr-doped $BaCeO_3$ compounds possess poor sinterability and high resistance at grain boundary [18], which severely impeded their applications. The use of high sintering temperatures (1700 °C) and long annealing times (24 h + 6 h) can lead to full densification [19], but lead also to BaO vaporization, which impairs the performance (conductivity and stability) of the obtained material [14, 20, 21]. Thus, the processing challenges necessitate the use of sintering additives [18, 22]. A widely studied sintering aid is NiO [18, 23-28], which permits a decrease in the densification temperature to ~ 1400 °C [28, 29]. NiO also contributes to enhanced grain growth. For instance, a grain size up to 10 μm has successfully been obtained for $BaZr_{0.5}Ce_{0.3}Y_{0.2}O_{3-\delta}$ with 1 wt.% NiO addition at 1600 °C [30]. Such a large grain size significantly reduces the number of grain boundaries, and hence, improves the conductivity [30-32]. Nevertheless, this temperature (1600 °C) is still rather high, thus, the sample has to be buried within powder precursors to prevent or compensate for BaO loss [33]. Further reduction of the temperature to 1550 °C can eliminate the need to use a BaO-protective powder cover, but cannot realize a comparable grain size exceeding 10 μm [18, 30], even when a prolonged sintering time of more than 20 h has been implemented [31]. Besides, the evolution of the local chemistry within grains and the nanosized grain boundaries following the large grain growth has not been well disclosed, which necessitates the utilization of high-resolution characterization methods, e.g. Atom Probe Tomography (APT).

In the current work, BCZ20Y15 with high density and grain sizes exceeding 10 μm is successfully synthesized by a solid state reaction at a temperature of 1500 °C. NiO is used as a sintering aid with a low amount (0.5 wt.%), and thus secondary phases are avoided after sintering. The chemical composition and distribution within the obtained large grains and nanosized grain boundaries are characterized by APT. Furthermore, the mechanism that promotes densification and grain growth behavior is elucidated based on the current experimental results and a review of literature studies.

2.2 Experimental

BCZ20Y15 samples were prepared by a solid state reaction method (SSR). $BaCO_3$ (99%, Sigma Aldrich), CeO_2 (99.9%, Sigma Aldrich), ZrO_2 (99%, Sigma Aldrich) and Y_2O_3 (99%, Sigma Aldrich) were used as starting materials. Precursor powders were mixed (shaker mixer TURBULA T2, Willy A. Bachofen GmbH, Nidderau, Germany) in ethanol according to the stoichiometry for 24 h and the resultant mixtures were dried at 80 °C. Then, the BCZ20Y15 mixtures were calcined at 1150 °C for 6 h [14] and 1300 °C for 5 h [33]. 0.5 wt. % NiO (99%, Sigma Aldrich) was then added to the calcined powders as a sintering aid [34], and the obtained powder mixture was ball-milled (Rollermill RM1, Zoz GmbH, Wenden, Germany. ZrO_2 balls, 3.5 mm diameter, weight ratio powder : balls : ethanol = 1 : 2 : 3) in ethanol for either 1 day or 7 days, respectively. Finally, the powder mixtures were dried and sieved through a 160 μm mesh.

Particle size distribution (PSD) of the meshed powders was measured by laser diffraction spectrometry (Horiba LA950-V2, Horiba Europe GmbH, Germany) and the specific surface area was measured via BET-method [35] by nitrogen adsorption at a temperature of -196 °C (AREAmeter Ⅱ, Ströhlein Instruments, Germany).

Bulk membranes were obtained by uniaxially pressing the powders into a disc shape under a pressure of ~ 20 MPa for 5 minutes, yielding green samples with diameters and thicknesses of ~ 27 mm and ~ 1 mm, respectively. The samples were sintered at 1500 °C for 5 h in air [33, 34], and a constant heating/cooling rate of 5 $K\cdot min^{-1}$ was used. Sintering behavior was characterized by a dilatometer (DIL 402 C Dilatometer, Netzsch-Gerätebau GmbH, Germany).

The crystal structure and phase purity of the sintered samples were characterized using an EMPYREAN (PANalytical) diffractometer with parafocusing Bragg-Brentano geometry, employing a Cu-LFF-tube (40 kV / 40 mA), a BBHD mirror (Bragg-BrentanoHD mirror, manufactured by Malvern Panalytical, Ltd., Malvern, UK), 0.04 rad Soller slits, and a PIXcel3D detector. X-ray diffraction (XRD) patterns were recorded at room temperature using a step scan procedure (0.4 s per step, 0.013 ° per step size) in the 2θ range of 5-90 °. The Rietveld refinement was conducted using the FullProf software package [36].

The microstructures and topographies of the samples were assessed by a Zeiss SUPRA 50VP field emission scanning electron microscope (SEM, Zeiss Microscopy GmbH, Oberkochen, Germany). The respective specimen for this test was first embedded in epoxy resin, ground sequentially using SiO_2 sandpaper with 400 and 2000 grit size and then polished using 6 μm, followed by a 1 μm, diamond suspension. The final polishing was conducted using 50 nm colloidal silica polishing suspension. The image analysis software Image J [37] was used to determine the grain sizes and porosity from the backscattered scanning electron microscope (BSEM) micrograph.

The chemical composition of the sintered sample was determined using the inductively-coupled plasma optical emission spectroscopy (ICP-OES) with a device of Thermo Fisher Scientific (Germany).

Atom probe tomography (APT) specimens were prepared using a dual-beam focused-ion-beam (FIB) system (FEI Helios Nanolab 600i) by the conventional liftout technique [38]. To reduce Ga implantation, a 2 keV Ga beam was used for the final shaping of APT tips. APT analyses were performed using a reflectron-equipped local electrode atom probe tool (LEAP 4000X HR, Cameca Instruments) in laser mode. Laser pulses of 355 nm wavelength, 12 ps pulse length, 30 pJ pulse energy and 200 kHz frequency were applied. The specimen base temperature was kept at 50 K and the ion detection rate was maintained at 1%. Data reconstruction and analysis were performed using Cameca IVAS 3.6.14 software package. Reconstruction parameters (evaporation field and image compression factor) were calibrated to match the specimen end radius and the length of the field-evaporated volume as measured by SEM done before and after the APT run.

2.3 Results and discussion

2.3.1 Powder pre-treatment

After calcination at 1150 °C for 6 h, the mixed powders still contain at least 4 phases, including raw materials of CeO_2 and $BaCO_3$, as indicated by the XRD investigation in the supplementary Figure A2.1. When the calcination temperature increases to 1300 °C, the powder mixtures are free of any kind of raw powders, but contain more than one perovskite phase (Figure 2.1 (a)). These phases share overlapped peak positions, which cannot be precisely separated and quantified (Figure 2.1(b)). Nevertheless, the upper and lower bounds of the compositions can be qualitatively (according to the peak positions) identified as $BaCe_{0.8}Y_{0.2}O_{3-\delta}$ (ICSD: 92261) and $BaZr_{0.885}Y_{0.115}O_{3-\delta}$ (ICSD: 8383), respectively. The $BaCe_{0.8}Y_{0.2}O_{3-\delta}$ phase possesses the highest intensities, and thus, represents the major phase, while $BaZr_{0.885}Y_{0.115}O_{3-\delta}$ is the minor phase with the lowest intensity. Intermediate phases are also presented, and their peak positions are between the ones of the major and the minor phase, but closer to the ones of the major phase. This indicates that the intermediate phases are also Ce and Y-rich perovskites and likely possess a small amount of Zr.

Although single-phase powders can be synthesized by additional calcination step(s) at the same or a high temperature [1, 13, 19, 28, 39-42], the multiple-phase powders obtained here by the one-step calcination were not thermally treated further but directly used for sintering after NiO addition and ball milling. There are two reasons behind this: firstly, the use of a sintering temperature (1500 °C) that is higher than the calcination temperature will eventually ensure the forming of single-phase composition, so it is not necessary to pre-synthesize single-phase powder precursors via the multiple calcination steps; secondly, and more importantly, it is anticipated that the significant amount of Ce-rich and Zr-free perovskites in the powder precursors is a benefit for fast grain growth during sintering [3, 39, 43-47], which will be discussed later in detail in section 2.3.4.

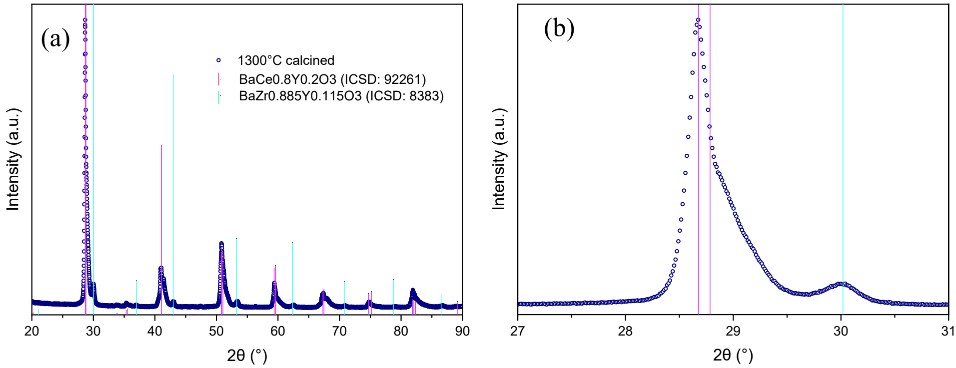

Figure 2.1 XRD patterns of the mixed powders after 1300 °C / 5 h calcination. (b) represents the magnified 2θ angle range in (a) covering the peak with the highest intensity. The legends in (a) also apply to (b).

2.3.2 Sintering with NiO

0.5 wt.% NiO as a sintering aid was added into the calcined powders before ball-milling to enhance sintering properties. A further ball-milling was carried out to reduce the particle size and primary grain size, thus benefiting sintering [48-50]. After either 1 day or 7 days of ball-milling, a negligible difference could be observed regarding the particle size distributions (Figure A2.2). However, the specific surface area of the powder after one week of ball-milling is ~ 4 m^2/g, which is significantly higher than the one (~ 1 m^2/g) after 24 h ball-milling. The higher specific surface area indicates a smaller primary grain size, implying a reduced elemental diffusion distance and enhanced driving force during sintering, which will benefit the formation of single-phase BCZ20Y15 during sintering.

The uniaxially cold-pressed powders were then sintered at 1500 °C for 5 h, thus single-phase BCZ20Y15 was obtained, as verified by XRD (Figure 2.2 (a)). The Rietveld analysis via FullProf yields the best calculation result (χ^2=2.21, Rwp=8.64) when the $BaCe_{0.65}Zr_{0.2}Y_{0.15}O_{3-\delta}$ (ICSD: 181962) with a space group of I2/m is used as the reference. This indicates that a single perovskite structure is obtained.

When NiO is used as a sintering aid, an emerging phase-BaY_2NiO_5 and residual NiO have been reported to exist in the sintered materials [18, 42, 50, 51], which is suggested to reduce the conductivity [28]. However, peaks related to potential phases in addition to the perovskites were not observed in the current XRD patterns, as shown in Figure 2.1 as well as Figure A2.3, indicating an optimization via elimination of secondary phases is successfully achieved for the material prepared in this work.

The microstructure of the sintered sample shows significantly large grain sizes of ~ 13 μm and fewer pores (< 1 %), as shown in Figure 2.2(b). For protonic conducting material, the impedance at grain boundaries is usually several orders higher than the bulk conductivity [52]. Larger grain sizes reflect fewer grain boundaries, which will thus benefit the proton conduction [32]. Besides, also fewer pores indicate a larger effective area for proton conduction. Therefore, the material obtained here exhibits significant advantages regarding microstructural characteristics for its application as a proton conducting membrane.

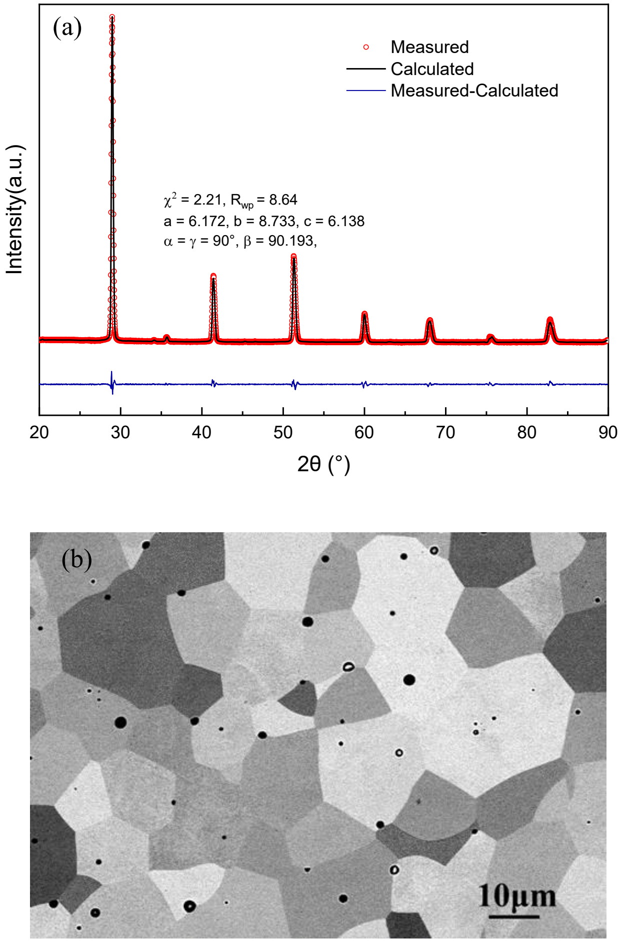

Figure 2.2 Rietveld refined XRD pattern (a) and microstructure (b) of the sample sintered at 1500 °C for 5 h (with 0.5 wt.% NiO as sintering aid). The black dots in (b) are pores.

2.3.3 Global and local chemistry

The ICP-OES characterized elements concentration (Table 1) reveals that the overall actual stoichiometry of the sintered material is $Ba_{0.98}Ce_{0.67}Zr_{0.19}Y_{0.14}O_{3-\delta}$, which is close to the targeted one - e.g. $BaCe_{0.65}Zr_{0.2}Y_{0.15}O_{3-\delta}$. This indicates no substantial loss of Ba at the sintering temperature of 1500 °C. Besides that, the Ni content confirms that the addition of NiO is indeed ~ 0.5 wt.%.

Table 2.1 Elemental concentration of BCZ20Y15 characterized by ICP-OES.

Probe	BCZ20Y15				
	Ba	Ce	Zr	Y	Ni
Content [wt.%]	46.6 ± 1.6	32.4 ± 1.1	5.9 ± 0.2	4.3 ± 0.1	0.45 ± 0.01

A complementary APT investigation was performed to elucidate the local chemistry of the grain bulk and boundary at a nanoscale. The grain boundary within the pre-sharpened APT specimen is marked by the arrows in Figure 2.3 (a). The 3D reconstructions of the cation distributions are displayed in Figure 2.3 (b-f)). At the grain boundary, Y, Zr, and Ni are enriched, while Ba is depleted. Ce seems also marginally accumulated at only a few positions (but not everywhere) within the grain boundary. As quantitative information, the elemental relative concentration profiles across the grain boundary were extracted from APT data and plotted in Figure 2.3 (g, h). The Ni is detected within the grain bulk (see Figure 2.3(h)), which indicates that Ni is doped into the perovskite crystal structure. The ratio between Ba, Y, and Ni significantly deviates from the one of the BaY_2NiO_5 phase, which has been reported as a potential secondary phase [28, 30, 51]. This suggests the absence of BaY_2NiO_5 as a second phase within the grain boundary. However, it should be noted that the absolute concentration values in the profiles are not accurate, since the peak overlap in the mass spectrum cannot be locally deconvoluted.

The grain boundary accumulation of Y has been also reported for $BaZrO_3$ doped with 6% [53] and 10% Y [54], where the grain boundary depletion of Ba has been only reported for 6% Sc-doped $BaZrO_3$ [53] but not for the Y-doped one [53, 54]. For the $BaZrO_3$-based materials, Y as a dopant replaces Zr forming the negatively charged $[Y'_{Zr}]$ [55], the accumulation of which at the grain boundary contributes to an improvement of the conductivity by reducing the space charge potential (or the width of the space charge layer) caused by the positively charged grain boundary core [53, 55, 56]. Analogously, for $BaCeO_3$-based materials, $[Y'_{Ce}]$ tends to form when Y is introduced as a dopant. Hence, the grain boundary accumulation of Y observed in our materials can benefit the conductivity. Besides, Ba depletion at the grain boundary can also be an advantage for the conductivity, considering that Ba vacancies are possibly negatively charged [53], which needs further investigation in future studies.

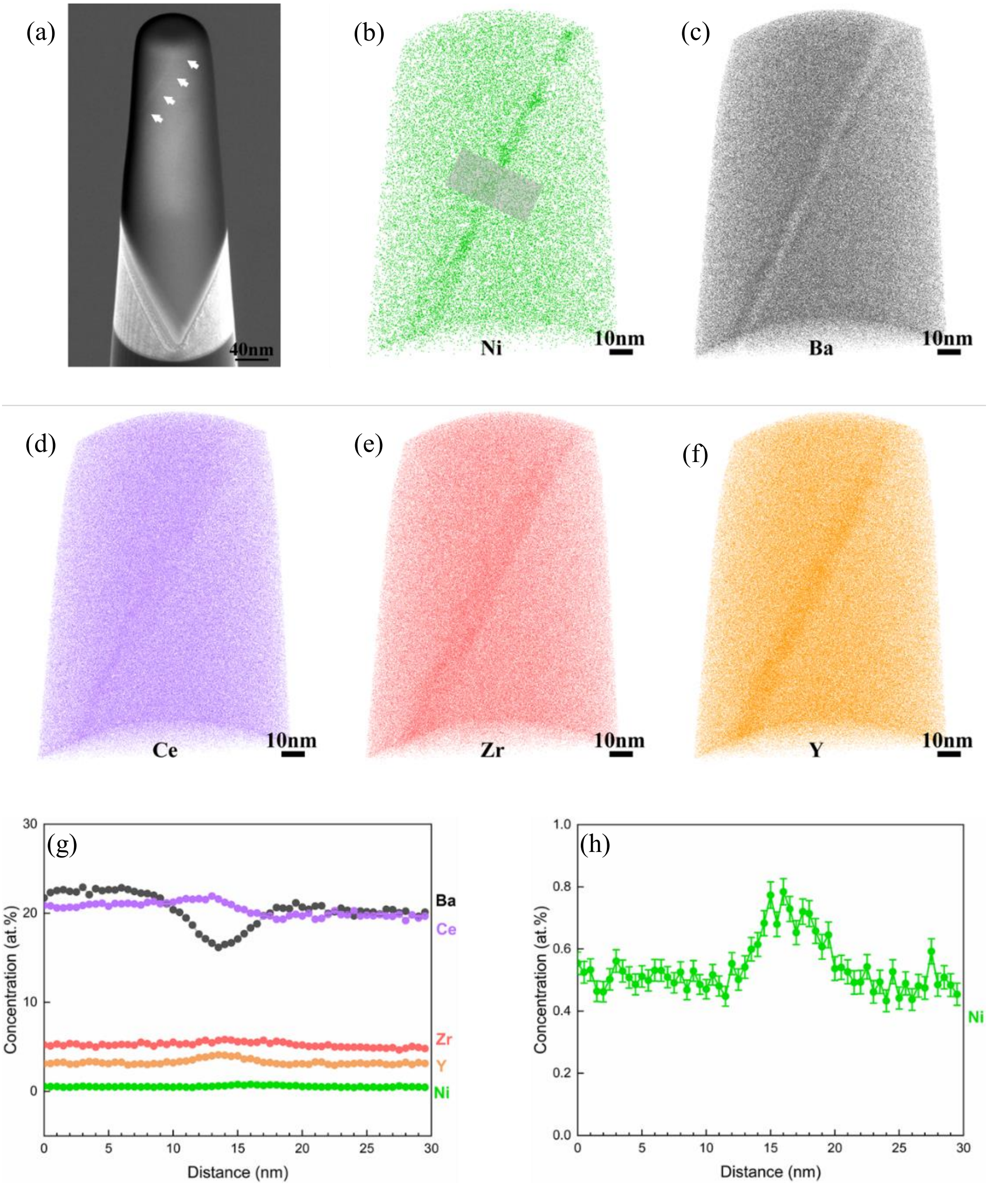

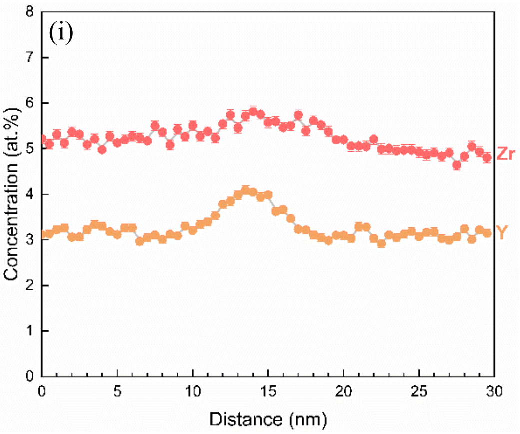

Figure 2.3 APT analysis of a BCZ20Y15 specimen. (a) SEM of the pre-sharped APT specimen. The arrows mark the grain boundary. (b) APT elemental maps for Ni, (c) Ba, (d) Ce, (e) Zr and (f) Y. (g) Elemental concentration profiles across the grain boundary of the position marked in (b), and in particular zoomed-in (h) the Ni concentration profile and (i) Zr and Y profiles.

2.3.4 Mechanism for promoting densification and grain growth

Substantial studies exist already on the synthesis of doped barium zirconate/cerate materials. One of the most widely used synthesis routines is the solid state reaction method, where $BaCO_3$ or $BaSO_4$, CeO_2, Y_2O_3, and/or ZrO_2 are used as the raw materials. The solid state reaction method is more environmentally friendly and cost-effective than the wet chemistry method [30, 31]. Besides, it is also very feasible and promising for upscaling.

In a conventional solid state reaction (CSSR) process, the raw materials are calcined to completely remove raw materials and form the desired single-phase solid solution. In addition, a sintering aid will be added, if necessary, into the calcined powders before compacting and sintering. Whereas, in an "unconventional" solid state reaction method, i.e. the so-called solid state reactive sintering (SSRS), the calcination step is excluded and the ball-milled powder mixture of raw materials and sintering aid, e.g. NiO, is directly compacted for sintering [18, 26, 30, 31, 47, 51, 57].

The BCZ20Y15 in this work was prepared following the CSSR procedure, but the calcination step was “incomplete” since heterogeneous perovskites are present within the calcined material. The sintering process of BCZ20Y15 involves complex phase evolution steps that can be analogous to those taking place during the SSRS process. Therefore, densification and grain growth behaviors observed here are compared with the reported ones from CSSR and SSRS.

2.3.4.1 Comparison with conventional solid state reaction (CSSR)

Table 2.2 displays a series of doped barium zirconate/cerate materials obtained by CSSR. Without sintering aid, Y-doped $BaCeO_3$ (Zr-free) materials generally possess much better sinterability (higher density and larger grain sizes at lower sintering temperatures) than Zr-doped $BaCeO_3$ materials. Furthermore, the grain growth is increased in the case of additional Y content for both Y-doped $BaCeO_3$ and Zr-doped $BaCeO_3$ materials. Besides, introducing Zr as a second dopant into the Y-doped $BaCeO_3$ significantly decreases the sinterability, which is closely correlated to the reduced Ce and Y concentrations. Therefore, the significant amount Zr-free and Y-rich Ba(Ce, Y)O_3 (likely $BaCe_{0.8}Y_{0.2}O_{3-\delta}$) as observed in our calcined material (see Figure 2.1) is a big advantage for densification due to its high intrinsic sinterability.

When NiO is added as a sintering aid, the sinterabilities of all Zr-containing materials are improved. The sinterability of BCZ20Y15 calcined material with 0.5 wt.% NiO in this work appears to be superior to other Zr-containing Ba(Ce, Y)O_3. An even better sinterability is expected for the Zr-free Ba(Ce, Y)O_3 with NiO addition due to its high intrinsic sinterability, although there is currently, to the best of our knowledge, no available data as direct support.

Currently, there are two theories to explain the role of NiO during sintering. One theory assumes that Ni is accommodated on the B-site of the parent perovskite [47, 58], i.e. doped into the crystal structure, which creates point defects and improves the diffusion leading to an enhanced sinterability [28, 59, 60]. The other one is a liquid phase sintering theory [18, 61]. NiO induces phase reactions at ~800 °C yielding a new phase product of $BaNiO_x$, followed by another reaction at ~900 °C, obtaining then BaY_2NiO_5 [31]. The perovskite as a reactant with NiO is expected to experience an increase in cation vacancies due to the loss of Ba and Y [51]. The emerging $BaNiO_x$ phase exists in a narrow temperature range between 800-850 °C [31], whereas, BaY_2NiO_5 remains in a broad temperature range between 900-1500 °C [30, 31]. BaY_2NiO_5 melts at 1450-1500 °C [31], and wets the solid grains, creating a capillary force that pulls the grains together. Thus, mass diffusion is facilitated in this liquid vessel, leading to grain coarsening at lower temperatures and for shorter sintering times [62].

The liquid phase sintering theory is well supported by the observation of BaY_2NiO_5 residue for the materials (except $BaCe_{0.35}Zr_{0.5}Y_{0.15}O_{3-\delta}$ and our BCZ20Y15) sintered below 1600 °C (see Table 2.2). For the materials sintered at 1600 °C, the BaY_2NiO_5 residue appears to be absent, since BaY_2NiO_5 likely decomposes itself at ~1600 °C [30, 31, 63]. Interestingly, for materials sintered at 1500 °C, BaY_2NiO_5 is found for $BaCe_{0.5}Zr_{0.3}Y_{0.2}O_{3-\delta}$ with 1 wt.% NiO addition [30], but not for our BCZ20Y15 with 0.5 wt.% NiO addition. Similarly, Tong et al. [26] also observed BaY_2NiO_5 in $BaZr_{0.8}Y_{0.2}O_{3-\delta}$ samples sintered with 1 wt.% and 2 wt.% NiO at 1500 °C, but not in the one with 0.5 wt.% NiO. Knight et al. [64] applied a fast quenching step as well as a slowly cooling step from 1500 °C for the $BaZr_{0.8}Y_{0.2}O_{3-\delta}$ samples sintered with 0.1-0.8 wt.% NiO content, and detected a BaY_2NiO_5 phase for all quenched samples but not for the slow cooled ones. This indicates that, when the NiO addition is less than 1 wt.%, BaY_2NiO_5 still forms but disappears (likely dissolves into the perovskite crystal structure according to the APT results in Figure 2.3) during slow cooling from 1500 °C. However, for $BaCe_{0.7}Zr_{0.2}Y_{0.1}O_{3-\delta}$ with 0.5 wt.% NiO sintered at 1400 °C, BaY_2NiO_5 is still present although no quenching step was applied [28]. Since the sintering temperature is ~50 K lower than the melting temperature of BaY_2NiO_5, BaY_2NiO_5 likely exists in a mixed state of solid and liquid. The liquid portion can easily dissolve into the surrounding perovskite particles due to the good contact, while the solid portion cannot dissolve and remains after cooling. But it is not clear, for $BaCe_{0.35}Zr_{0.5}Y_{0.15}O_{3-\delta}$ with 4 mol.% NiO sintered at 1400 °C, why NiO is residual instead of BaY_2NiO_5.

Nevertheless, BaY_2NiO_5 is expected to form from the phase reactions between our calcined BCZ20Y15 and NiO, and it melts at the final sintering temperature (1500 °C), but disappears after cooling. The occurrence of the phase reactions is indicated by the decreased initial shrinking temperature after NiO addition, as shown in Table 2.2. The BCZ20Y15 calcine with 0.5 wt.% in this work starts to shrink at 800 °C (see Table 2.2 and Figure 2.4), which is almost identical to the phase reaction temperature. Whereas, the initial shrinking temperature is only reduced to ~1000 °C for $BaCe_{0.7}Zr_{0.1}Y_{0.2}O_{3-\delta}$ [28] and $BaCe_{0.35}Zr_{0.5}Y_{0.15}O_{3-\delta}$ by NiO addition, which can be attributed to the low sinterability of the material itself due to Zr incorporation as well as sluggish and hysteretic phase reactions, possibly caused by the Zr-stabilized perovskite structure. It is anticipated that, in low-temperature ranges (< 1000 °C), the reaction in the current calcined BCZ20Y15 mainly initiates between NiO and the $Ba(Ce, Y)O_3$ (which possesses no Zr, and hence has a high intrinsic sinterability) phase component, which promotes the shrinkage. Despite the low reactivity with NiO below 1000 °C, the particles of other Zr-rich $Ba(Zr, Y)O_3$ phase components are likely to be compacted together by the surrounding particles of the $Ba(Ce, Y)O_3$ phase component. Above a certain temperature, the different perovskite phases are expected to be merged as one perovskite phase, and the role of NiO in this process will be discussed in the next section in comparison with SSRS.

Table 2.2 Ba(Ce, Y, Zr)O_3 synthesized by CSSR.

Material	NiO addition	Initial shrinking temperature	Final sintering conditions	Density [%]	Grain size [µm]	Secondary phase(s)	Ref.
$BaZr_{0.95}Y_{0.05}O_{3-\delta}$	-	-	1800 °C for 20 h	> 95	0.67	-	[43, 65]
$BaZr_{0.9}Y_{0.1}O_{3-\delta}$	-	-	1800 °C for 20 h	> 95	1.4	-	[43]
	1 wt.%	-	1600 °C for 10 h	96.5	1-4	-	[66]
$BaZr_{0.85}Y_{0.15}O_{3-\delta}$	-	-	1800 °C for 20 h	> 95	2.7	-	[43]
$BaZr_{0.8}Y_{0.2}O_{3-\delta}$	-	-	1600 °C for 10 h	~100	1.4	-	[67]
	-	-	1500 °C for 24 h	97	0.7	-	[68]
$BaCe_{0.9}Y_{0.1}O_{3-\delta}$	-	-	1600 °C for 24 h	97.5	8-12	-	[69]
	-	-	1550 °C or 10 h	-	2.8	-	[70]
$BaCe_{0.8}Y_{0.2}O_{3-\delta}$	-	-	1550 °C or 10 h	-	4.5	-	[70]
$BaCe_{0.7}Zr_{0.1}Y_{0.2}O_{3-\delta}$	-	1150°C	1400 °C for 6 h	79.5	0.9	-	[28]
	0.5 wt.%	1000°C	1400 °C for 6 h	98.7	3.6	BaY_2NiO_5	[28]
$BaCe_{0.6}Zr_{0.3}Y_{0.1}O_{3-\delta}$	-	-	1700 °C for 6 h	90-95	0.5-5	-	[39]
$BaCe_{0.5}Zr_{0.3}Y_{0.2}O_{3-\delta}$	-	-	1600 °C for 10 h	> 95	1.5	-	[30]
	1 wt.%	-	1600 °C for 10 h	> 95	5	-	[30]
	1 wt.%	-	1500 °C for 10 h	> 97	3	BaY_2NiO_5	[30]
$BaCe_{0.35}Zr_{0.5}Y_{0.15}O_{3-\delta}$	-	1150°C	1700 °C for 10 h	> 95	3-5	-	[42]
	4 mol.%	1000°C	1400 °C for 6 h	> 95	3-5	NiO	[42]
$BaCe_{0.65}Zr_{0.2}Y_{0.15}O_{3-\delta}$	**0.5 wt.%**	**800°C**	**1500 °C for 5h**	**> 99**	**13**	-	**This work**

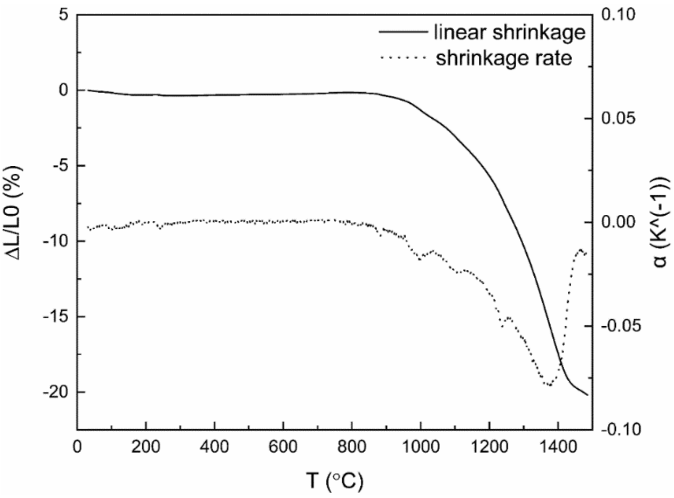

Figure 2.4 Sintering behaviour of the BCZ20Y15 calcine (with 0.5 wt.% NiO addition).

2.3.4.2 Comparison with solid state reactive sintering (SSRS)

Table 2.3 lists several Ba(Ce, Y, Zr)O_3 materials synthesized by SSRS with 1 wt.% NiO at sintering temperatures of 1500 °C or 1400 °C. The highest sinterability is observed for the $BaCe_{0.8}Y_{0.2}O_{3-\delta}$ with 1 wt. % NiO addition, which coincides with our conclusions from CSSR that the Zr-free Ba(Ce, Y)O_3 composition will gain the largest promotion on sinterability by NiO addition. Besides, comparable sinterabilities are indicated for the Zr and Y co-doped $BaCeO_3$ during SSRS and CSSR with NiO addition, while better sinterability is shown for the calcined BCZ20Y15 with NiO addition in the current work. Besides, a BaY_2NiO_5 residue is generally found for the Ba(Ce, Y, Zr)O_3 materials with 20 %Y, while for the Ba(Ce, Y, Zr)O_3 materials with Y less than 20%, BaY_2NiO_5 will not be residue and it is probably dissolved into perovskites. This reflects that the Y content, in addition to the NiO content as discussed in the previous section, also affects the presence of any BaY_2NiO_5 residue.

Table 2.3 Ba(Ce, Y, Zr)O_3 synthesized by SSRS with 1 wt.% NiO.

Material	Sintering	Density [%]	Grain size [μm]	Secondary phase(s)	Ref.
$BaZr_{0.9}Y_{0.1}O_{3-\delta}$	1500 °C for 4 h	98	1.3	Negligible	[57]
$BaZr_{0.8}Y_{0.2}O_{3-\delta}$	1500 °C for 24 h	95	5	BaY_2NiO_5	[26]
$BaCe_{0.8}Y_{0.2}O_{3-\delta}$	1400 °C for 12 h	98	> 10	BaY_2NiO_5	[51]
$BaCe_{0.5}Zr_{0.3}Y_{0.2}O_{3-\delta}$	1500 °C for 10 h	> 97	≥3	BaY_2NiO_5	[30]
$BaCe_{0.4}Zr_{0.5}Y_{0.1}O_{3-\delta}$	1500 °C for 4 h	98.2	3.3	Negligible	[57]
$Ba_{1.015}Zr_{0.664}Ce_{0.20}Y_{0.136}O_{3-\delta}$	1500 °C for 8 h	>95	2-3	No	[18]

During the SSRS process, raw materials disappear gradually and emerging phases including $BaNiO_x$, BaY_2NiO_5, and Ba(Ce, Y, Zr)O_3 perovskites appear successively above 800 °C [18, 31]. The powder mixtures can approach a sintering stage that is analogous to the one in this work, where heterogenous perovskites with NiO are present. For instance, during the SSRS process of $Ba_{1.015}Zr_{0.664}Ce_{0.20}Y_{0.136}O_{3-\delta}$ with 0.5 wt. % NiO, a nearly undoped $BaZrO_3$ phase and a Zr-free Ba(Ce, Y)O_3 phase form simultaneously at ~1000 °C [18], and merge into one single perovskite phase above 1400 °C. Further increasing the NiO content to 2 wt.% is reported to decrease the formation temperature of the single perovskite phase by 50 K [18], which highlights the NiO contribution regarding uniforming perovskite phases. For comparison, the calcined powders in this work contain a similar phase component, i.e., the Zr-free Ba(Ce, Y)O_3 phase, but also a different one, i.e. the Y-doped $BaZrO_3$ instead of the undoped $BaZrO_3$ phase. A temperature below 1400 °C can be expected for the formation of a single perovskite phase in the calcined powders (with 0.5 wt. % NiO) in this work, since the crystal structure discrepancy between the Zr-free Ba(Ce, Y)O_3 and the Y-doped $BaZrO_3$ is smaller than the one between the Zr-free Ba(Ce, Y)O_3 and the undoped $BaZrO_3$. Besides, this reduction is also contributed by the phase reactions between the Zr-free Ba(Ce, Y)O_3 and NiO starting at ~800 °C. The phase reactions possibly stimulate and/or promote complex cation/anion/defects diffusion between particles of different perovskites to construct a new stable perovskite structure in two ways: 1) increasing concentrations of cation vacancies in the Zr-free Ba(Ce, Y)O_3, and 2) initiating a shrinkage and reduction of the particle distance.

According to all discussions above, sinterability is verified to be superior for our calcined BCZ20Y15 after adding 0.5 wt.% NiO in comparison to literature data. The superiority is attributed to the NiO addition as well as the presence of the Zr-free Ba(Ce, Y)O_3 phase as the major component in the BCZ20Y15 calcine. The Zr-free Ba(Ce, Y)O_3 phase possesses high sinterability. It likely reacts with NiO and initiates sintering of the BCZ20Y15 calcine at a temperature as low as 800 °C. It will merge with the minor Zr-rich Ba(Zr, Y)O_3 phase components forming a single-phase perovskite at a temperature lower than 1400 °C due to NiO. At the final sintering temperature of 1500 °C, the phase reaction product-BaY_2NiO_5 melts and significantly promotes densification and grain growth. The amount of BaY_2NiO_5 is low due to the low NiO addition (0.5 wt. %) so the BaY_2NiO_5 likely dissolves completely into the perovskite crystal structure, instead of being a residue after sintering.

2.4 Conclusions

In the current work, a superior microstructure (density of > 99 % and average grain size of ~13 µm) is obtained for the proton conducting ceramic BCZ20Y15 at a sintering temperature of 1500 °C. Although 0.5 wt.% NiO is added as a sintering aid and the calcined powders possess heterogenous perovskite phases, no secondary phase impurities in addition to BCZ20Y15 perovskite are found according to XRD, SEM, and APT investigations. The superior sinterability is attributed to the NiO addition as well as the presence of a very sinterable phase (likely $BaCe_{0.8}Y_{0.2}O_{3-\delta}$) as the major component in the calcined powders. NiO starts to promote the sintering behavior of the calcine at a low temperature possibly by reacting with the abundant $BaCe_{0.8}Y_{0.2}O_{3-\delta}$ phase in the calcine. The phase reaction product (likely BaY_2NiO_5) melts and significantly promotes the densification and grain growth during the final sintering stage at 1500 °C. However, the BaY_2NiO_5 is not residual after sintering but likely dissolves into the perovskite crystal structure. Furthermore, a potential alleviation of the space change potential, and hence a benefit for conductivity is indicated by the accumulation of Y and depletion of Ba at the grain boundary as characterized by APT.

References

[1] K. Katahira, Y. Kohchi, T. Shimura, H. Iwahara, Protonic conduction in Zr-substituted $BaCeO_3$, Solid State Ionics 138(1) (2000) 91-98.

[2] X. Ma, J. Dai, H. Zhang, D.E. Reisner, Protonic conductivity nanostructured ceramic film with improved resistance to carbon dioxide at elevated temperatures, Surface and Coatings Technology 200(5-6) (2005) 1252-1258.

[3] P. Sawant, S. Varma, B. Wani, S. Bharadwaj, Synthesis, stability and conductivity of $BaCe_{0.8-x}Zr_xY_{0.2}O_{3-\delta}$ as electrolyte for proton conducting SOFC, international journal of hydrogen energy 37(4) (2012) 3848-3856.

[4] M. Yano, A. Tomita, M. Sano, T. Hibino, Recent advances in single-chamber solid oxide fuel cells: a review, Solid State Ionics 177(39-40) (2007) 3351-3359.

[5] N. Radenahmad, A. Afif, P.I. Petra, S.M. Rahman, S.-G. Eriksson, A.K. Azad, Proton-conducting electrolytes for direct methanol and direct urea fuel cells–A state-of-the-art review, Renewable and Sustainable Energy Reviews 57 (2016) 1347-1358.

[6] J. Phair, S. Badwal, Review of proton conductors for hydrogen separation, Ionics 12(2) (2006) 103-115.

[7] K. Kreuer, Proton-conducting oxides, Annual Review of Materials Research 33(1) (2003) 333-359.

[8] G. Chiodelli, L. Malavasi, C. Tealdi, S. Barison, M. Battagliarin, L. Doubova, M. Fabrizio, C. Mortalo, R. Gerbasi, Role of synthetic route on the transport properties of $BaCe_{1-x}Y_xO_3$ proton conductor, Journal of Alloys and Compounds 470(1-2) (2009) 477-485.

[9] E. Fabbri, A. D'Epifanio, E. Di Bartolomeo, S. Licoccia, E. Traversa, Tailoring the chemical stability of $Ba\,(Ce_{0.8-x}Zr_x)Y_{0.2}O_{3-\delta}$ protonic conductors for intermediate temperature solid oxide fuel cells (IT-SOFCs), Solid State Ionics 179(15-16) (2008) 558-564.

[10] A. Magrez, T. Schober, Preparation, sintering, and water incorporation of proton conducting $Ba_{0.99}Zr_{0.8}Y_{0.2}O_{3-\delta}$: comparison between three different synthesis techniques, Solid State Ionics 175(1-4) (2004) 585-588.

[11] S. Tao, J.T. Irvine, Conductivity studies of dense yttrium-doped $BaZrO_3$ sintered at 1325 C, Journal of Solid State Chemistry 180(12) (2007) 3493-3503.

[12] J. Li, J.-L. Luo, K.T. Chuang, A.R. Sanger, Chemical stability of Y-doped Ba (Ce, Zr) O_3 perovskites in H_2S-containing H_2, Electrochimica Acta 53(10) (2008) 3701-3707.

[13] K.H. Ryu, S.M. Haile, Chemical stability and proton conductivity of doped $BaCeO_3$–$BaZrO_3$ solid solutions, Solid State Ionics 125(1-4) (1999) 355-367.

[14] S. Barison, M. Battagliarin, T. Cavallin, S. Daolio, L. Doubova, M. Fabrizio, C. Mortalo, S. Boldrini, R. Gerbasi, Barium Non - Stoichiometry Role on the Properties of $Ba_{1+x}Ce_{0.65}Zr_{0.20}Y_{0.15}O_{3-\delta}$ Proton Conductors for IT-SOFCs, Fuel cells 8(5) (2008) 360-368.

[15] S. Barison, M. Battagliarin, T. Cavallin, L. Doubova, M. Fabrizio, C. Mortalo, S. Boldrini, L. Malavasi, R. Gerbasi, High conductivity and chemical stability of $BaCe_{1-x-y}Zr_xY_yO_{3-\delta}$ proton conductors prepared by a sol–gel method, Journal of Materials Chemistry 18(42) (2008) 5120-5128.

[16] L. Doubova, S. Barison, S. Boldrini, M. Fabrizio, C. Mortalo, C. Pagura, Conductivity studies of sol-gel prepared $BaCe_{0.85-x}Zr_xY_{0.15}O_{3-\delta}$ solid electrolytes using impedance spectroscopy, Journal of applied electrochemistry 39(11) (2009) 2129-2141.

[17] E. Rebollo, C. Mortalo, S. Escolástico, S. Boldrini, S. Barison, J.M. Serra, M. Fabrizio, Exceptional hydrogen permeation of all-ceramic composite robust membranes based on $BaCe_{0.65}Zr_{0.20}Y_{0.15}O_{3-\delta}$ and Y-or Gd-doped ceria, Energy & Environmental Science 8(12) (2015) 3675-3686.

[18] Y. Huang, R. Merkle, J. Maier, Effects of NiO addition on sintering and proton uptake of Ba (Zr, Ce, Y)$O_{3-\delta}$, Journal of Materials Chemistry A (2021).

[19] S. Ricote, N. Bonanos, M.M. De Lucas, G. Caboche, Structural and conductivity study of the proton conductor $BaCe_{(0.9-x)}Zr_xY_{0.1}O_{(3-\delta)}$ at intermediate temperatures, Journal of Power Sources 193(1) (2009) 189-193.

[20] P. Babilo, T. Uda, S.M. Haile, Processing of yttrium-doped barium zirconate for high proton conductivity, Journal of materials research 22(5) (2007) 1322-1330.

[21] S. Haile, G. Staneff, K. Ryu, Non-stoichiometry, grain boundary transport and chemical stability of proton conducting perovskites, Journal of Materials Science 36(5) (2001) 1149-1160.

[22] F.J. Loureiro, N. Nasani, G.S. Reddy, N. Munirathnam, D.P. Fagg, A review on sintering technology of proton conducting $BaCeO_3$-$BaZrO_3$ perovskite oxide materials for Protonic Ceramic Fuel Cells, Journal of Power Sources 438 (2019) 226991.

[23] D. Han, K. Shinoda, S. Tsukimoto, H. Takeuchi, C. Hiraiwa, M. Majima, T. Uda, Origins of structural and electrochemical influence on Y-doped $BaZrO_3$ heat-treated with NiO additive, Journal of Materials Chemistry A 2(31) (2014) 12552-12560.

[24] C.-Y. Yoo, D.S. Yun, J.H. Joo, J.H. Yu, The effects of NiO addition on the structure and transport properties of proton conducting $BaZr_{0.8}Y_{0.2}O_{3-\delta}$, Journal of Alloys and Compounds 621 (2015) 263-267.

[25] E. Kim, Y. Yamazaki, S. Haile, H.-I. Yoo, Effect of NiO sintering-aid on hydration kinetics and defect-chemical parameters of $BaZr_{0.8}Y_{0.2}O_{3-\Delta}$, Solid State Ionics 275 (2015) 23-28.

[26] J. Tong, D. Clark, M. Hoban, R. O'Hayre, Cost-effective solid-state reactive sintering method for high conductivity proton conducting yttrium-doped barium zirconium ceramics, Solid State Ionics 181(11) (2010) 496-503.

[27] J.M. Polfus, M.-L. Fontaine, A. Thøgersen, M. Riktor, T. Norby, R. Bredesen, Solubility of transition metal interstitials in proton conducting BaZrO 3 and similar perovskite oxides, Journal of Materials Chemistry A 4(21) (2016) 8105-8112.

[28] Z. Liu, X. Wang, M. Liu, J. Liu, Enhancing sinterability and electrochemical properties of $Ba(Zr_{0.1}Ce_{0.7}Y_{0.2})O_{3-\delta}$ proton conducting electrolyte for solid oxide fuel cells by addition of NiO, Int. J. Hydrogen Energy 43(29) (2018) 13501-13511.

[29] J. Bu, P.G. Jönsson, Z. Zhao, Transport properties of $BaZr_{0.5}Ce_{0.3}Y_{0.2}O_{3-\delta}$ proton conductor prepared by spark plasma sintering, Ceramics International 42(3) (2016) 4393-4399.

[30] J. Bu, P.G. Jönsson, Z. Zhao, The effect of NiO on the conductivity of $BaZr_{0.5}Ce_{0.3}Y_{0.2}O_{3-\delta}$ based electrolytes, RSC Advances 6(67) (2016) 62368-62377.

[31] J. Tong, D. Clark, L. Bernau, M. Sanders, R. O'Hayre, Solid-state reactive sintering mechanism for large-grained yttrium-doped barium zirconate proton conducting ceramics, J. Mater. Chem. 20(30) (2010) 6333-6341.

[32] B. Wang, L. Bi, X.S. Zhao, Exploring the role of NiO as a sintering aid in $BaZr_{0.1}Ce_{0.7}Y_{0.2}O_{3-\delta}$ electrolyte for proton-conducting solid oxide fuel cells, J. Power Sources 399 (2018) 207-214.

[33] W. Zhou, J. Malzbender, F. Zeng, W. Deibert, O. Guillon, R. Schwaiger, W.A. Meulenberg, Mechanical properties of $BaCe_{0.65}Zr_{0.2}Y_{0.15}O_{3-\delta}$ proton-conducting material determined using different nanoindentation methods, Journal of the European Ceramic Society 40(15) (2020) 5653-5661.

[34] W. Zhou, J. Malzbender, W. Deibert, O. Guillon, R. Schwaiger, A. Nijmeijer, W.A. Meulenberg, High temperature compressive creep behavior of $BaCe_{0.65}Zr_{0.2}Y_{0.15}O_{3-\delta}$ in air and 4% H_2/Ar, Journal of the American Ceramic Society 104(6) (2021) 2730-2740.

[35] S. Brunauer, P.H. Emmett, E. Teller, Adsorption of gases in multimolecular layers, Journal of the American chemical society 60(2) (1938) 309-319.

[36] J. Rodríguez-Carvajal, Recent advances in magnetic structure determination by neutron powder diffraction, Physica B: Condensed Matter 192(1) (1993) 55-69.

[37] C.A. Schneider, W.S. Rasband, K.W. Eliceiri, NIH Image to ImageJ: 25 years of image analysis, Nature methods 9(7) (2012) 671-675.

[38] K. Thompson, D. Lawrence, D. Larson, J. Olson, T. Kelly, B. Gorman, In situ site-specific specimen preparation for atom probe tomography, Ultramicroscopy 107(2-3) (2007) 131-139.

[39] S. Ricote, N. Bonanos, G. Caboche, Water vapour solubility and conductivity study of the proton conductor $BaCe_{(0.9-x)}Zr_xY_{0.1}O_{(3-\delta)}$, Solid State Ionics 180(14) (2009) 990-997.

[40] C. Zuo, S. Zha, M. Liu, M. Hatano, M. Uchiyama, $Ba(Zr_{0.1}Ce_{0.7}Y_{0.2})O_{3-\delta}$ as an Electrolyte for Low-Temperature Solid-Oxide Fuel Cells, Adv. Mater. 18(24) (2006) 3318-3320.

[41] L. Yang, C. Zuo, M. Liu, High-performance anode-supported Solid Oxide Fuel Cells based on $Ba(Zr_{0.1}Ce_{0.7}Y_{0.2})O_{3-\delta}$ (BZCY) fabricated by a modified co-pressing process, J. Power Sources 195(7) (2010) 1845-1848.

[42] H. An, D. Shin, H.-I. Ji, Effect of Nickel Addition on Sintering Behavior and Electrical Conductivity of $BaCe_{0.35}Zr_{0.5}Y_{0.15}O_{3-\delta}$, J. Korean Ceram. Soc 56(1) (2019) 91-97.

[43] F. Iguchi, N. Sata, T. Tsurui, H. Yugami, Microstructures and grain boundary conductivity of $BaZr_{1-x}Y_xO_3$ (x=0.05, 0.10, 0.15) ceramics, Solid State Ionics 178(7) (2007) 691-695.

[44] H.-W. Kim, J. Seo, J.H. Yu, K.S. Yun, J.H. Joo, J. Moon, H.J. Park, Effect of cerium on yttrium-doped barium zirconate with a ZnO sintering aid: Grain and grain boundary protonic conduction, Ceram. Int. 47(23) (2021) 32720-32726.

[45] Z. Zhong, Stability and conductivity study of the $BaCe_{0.9-x}Zr_xY_{0.1}O_{2.95}$ systems, Solid State Ionics 178(3) (2007) 213-220.

[46] N. Nasani, P.A.N. Dias, J.A. Saraiva, D.P. Fagg, Synthesis and conductivity of $Ba(Ce,Zr,Y)O_{3-\delta}$ electrolytes for PCFCs by new nitrate-free combustion method, Int. J. Hydrogen Energy 38(20) (2013) 8461-8470.

[47] S. Nikodemski, J. Tong, R. O'Hayre, Solid-state reactive sintering mechanism for proton conducting ceramics, Solid State Ionics 253 (2013) 201-210.

[48] M.N. Rahaman, Ceramic processing and sintering, CRC press2017.

[49] E. Jud, L.J. Gauckler, Sintering behavior of cobalt oxide doped ceria powders of different particle sizes, Journal of electroceramics 14(3) (2005) 247-253.

[50] D.S. Yun, J. Kim, S.-J. Kim, J.-H. Lee, J.-N. Kim, H.C. Yoon, J.H. Yu, M. Kwak, H. Yoon, Y. Cho, Structural and electrochemical properties of dense yttria-doped barium zirconate prepared by solid-state reactive sintering, Energies 11(11) (2018) 3083.

[51] J. Tong, D. Clark, L. Bernau, A. Subramaniyan, R. O'Hayre, Proton-conducting yttrium-doped barium cerate ceramics synthesized by a cost-effective solid-state reactive sintering method, Solid State Ionics 181(33) (2010) 1486-1498.

[52] Y. Yamazaki, R. Hernandez-Sanchez, S.M. Haile, High total proton conductivity in large-grained yttrium-doped barium zirconate, Chemistry of Materials 21(13) (2009) 2755-2762.

[53] M. Shirpour, B. Rahmati, W. Sigle, P.A. van Aken, R. Merkle, J. Maier, Dopant Segregation and Space Charge Effects in Proton-Conducting $BaZrO_3$ Perovskites, The Journal of Physical Chemistry C 116(3) (2012) 2453-2461.

[54] D.R. Clark, H. Zhu, D.R. Diercks, S. Ricote, R.J. Kee, A. Almansoori, B.P. Gorman, R.P. O'Hayre, Probing Grain-Boundary Chemistry and Electronic Structure in Proton-Conducting Oxides by Atom Probe Tomography, Nano Lett. 16(11) (2016) 6924-6930.

[55] A. Uthayakumar, A. Pandiyan, S.B. Krishna Moorthy, Yttrium dependent space charge effect on modulating the conductivity of barium zirconate electrolyte for solid oxide fuel cell, Int. J. Hydrogen Energy 43(52) (2018) 23488-23499.

[56] A. Uthayakumar, A. Pandiyan, S. Mathiyalagan, A.K. Keshri, S.B. Krishna Moorthy, The Effect of Space Charge on Blocking Grain Boundary Resistance in an Yttrium-Doped Barium Zirconate Electrolyte for Solid Oxide Fuel Cells, The Journal of Physical Chemistry C 124(10) (2020) 5591-5599.

[57] S. Ricote, N. Bonanos, A. Manerbino, W.G. Coors, Conductivity study of dense $BaCe_xZr_{(0.9-x)}Y_{0.1}O_{(3-\delta)}$ prepared by solid state reactive sintering at 1500 °C, Int. J. Hydrogen Energy 37(9) (2012) 7954-7961.

[58] R. Costa, N. Grünbaum, M.-H. Berger, L. Dessemond, A. Thorel, On the use of NiO as sintering additive for $BaCe_{0,9}Y_{0,1}O_{3-\alpha}$, Solid State Ionics 180(11-13) (2009) 891-895.

[59] F. Yu, J. Xiao, L. Lei, W. Cai, Y. Zhang, J. Liu, M. Liu, Effects of doping alumina on the electrical and sintering performances of yttrium-stabilized-zirconia, Solid State Ionics 289 (2016) 28-34.

[60] S. Li, L. Wang, Special Ceramic Technology, Wuhan Institute of Technology Press, Wuhan 132 (1990).

[61] Y. Huang, R. Merkle, J. Maier, Effect of NiO addition on proton uptake of $BaZr_{1-x}Y_xO_{3-x/2}$ and $BaZr_{1-x}Sc_xO_{3-x/2}$ electrolytes, Solid State Ionics 347 (2020) 115256.

[62] R.M. German, P. Suri, S.J. Park, Liquid phase sintering, Journal of materials science 44(1) (2009) 1-39.

[63] D. Han, Y. Otani, Y. Noda, T. Onishi, M. Majima, T. Uda, Strategy to improve phase compatibility between proton conductive $BaZr_{0.8}Y_{0.2}O_{3-\delta}$ and nickel oxide, RSC Advances 6(23) (2016) 19288-19297.

[64] M. Knight, D. Jennings, S. Ricote, I. Reimanis, Estimating Ni valence with magnetometry in solid-state reactive sintered yttrium-doped barium zirconate, J. Am. Ceram. Soc. 105(1) (2022) 159-168.

[65] F. Iguchi, T. Yamada, N. Sata, T. Tsurui, H. Yugami, The influence of grain structures on the electrical conductivity of a $BaZr_{0.95}Y_{0.05}O_3$ proton conductor, Solid State Ionics 177(26) (2006) 2381-2384.

[66] S. Ricote, N. Bonanos, A. Manerbino, N.P. Sullivan, W.G. Coors, Effects of the fabrication process on the grain-boundary resistance in $BaZr_{0.9}Y_{0.1}O_{3-\delta}$, Journal of Materials Chemistry A 2(38) (2014) 16107-16115.

[67] L.P. Wendler, K. Ramos, D.M.P.F. Souza, Investigation about the reason of limited grain growth of Y-doped barium zirconate, Ceram. Int. 45(15) (2019) 19120-19126.

[68] C.A. Goulart, L.A.V. Boas, M.R. Morelli, D.P.F.d. Souza, Reactive sintering of yttrium-doped barium zirconate ($BaZr_{0.8}Y_{0.2}O_{3-\delta}$) without sintering aids, Ceram. Int. 47(2) (2021) 2565-2571.

[69] A. Lacz, Effect of microstructure on chemical stability and electrical properties of $BaCe_{0.9}Y_{0.1}O_{3-\delta}$, Ionics 22(8) (2016) 1405-1414.

[70] E.T. Park, K.C. Goretta, A.R. de Arellano-López, J. Guan, U. Balachandran, S.E. Dorris, J.L. Routbort, High-temperature deformation of $BaCe_{1-x}Y_xO_{3-y}$ ($0.05 \leqslant x \leqslant 0.2$), Solid State Ionics 117(3) (1999) 323-330.

Appendix A2

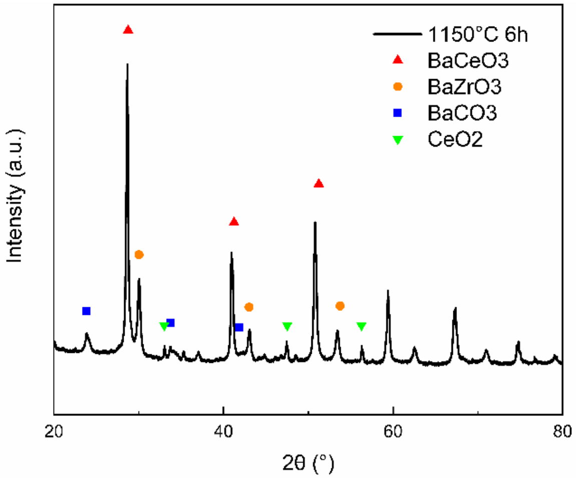

Figure A2.1 XRD pattern of the powder after a calcination at 1150 °C for 6 h

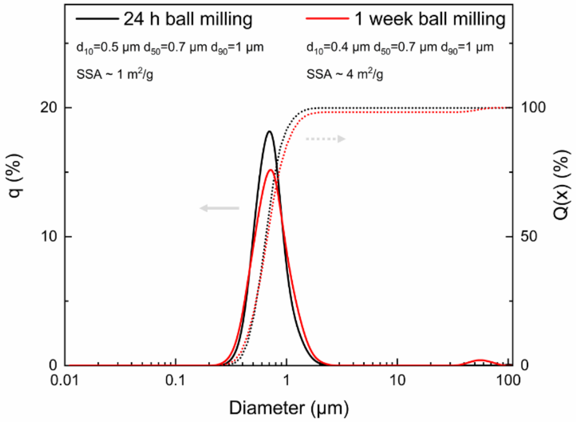

Figure A2.2 Particle size distribution and specific surface area after a further 24 h and 1 week ball-milling, q representing particle amount and Q(x) representing the accumulated amount.

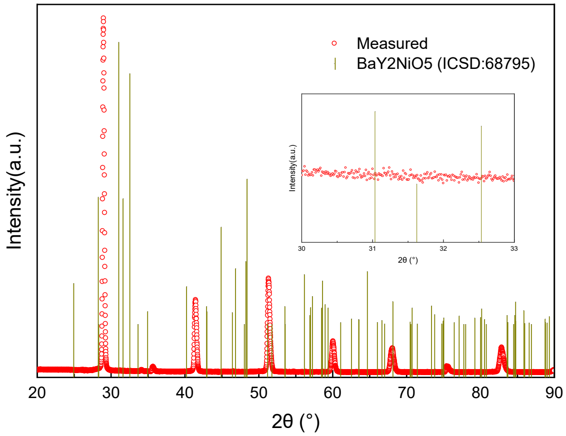

Figure A2.3 Comparison between the reference pattern of BaY_2NiO_5 and the measured XRD pattern of the sample sintered at 1500 °C for 5 h (with 0.5 wt.% NiO as sintering aid).

CHAPTER 3

Mechanical properties of $BaCe_{0.65}Zr_{0.2}Y_{0.15}O_{3-\delta}$ proton-conducting material determined using different nanoindentation methods

Abstract

Proton-conducting membranes have great potential for applications in proton conducting membrane reactors for the production of commodity chemicals or synthetic fuels as well as for use in solid oxide fuel cells. However, to ensure the long-term structural stability under operation relevant conditions, the mechanical properties of the membrane materials need to be characterized. $BaCe_{0.65}Zr_{0.2}Y_{0.15}O_{3-\delta}$ is of particular interest due to its proven functional properties. In this research work, the mechanical properties of $BaCe_{0.65}Zr_{0.2}Y_{0.15}O_{3-\delta}$ were determined on different length scales using different methods including impulse excitation, indentation testing, and micro-pillar splitting. A detailed microstructural analysis of pillars revealed that irregular results are caused by pores causing crack deflection and complex crack patterns.

This chapter has been published as: W. Zhou, J. Malzbender, F. Zeng, W. Deibert, O. Guillon, R. Schwaiger, W.A. Meulenberg, Mechanical properties of $BaCe_{0.65}Zr_{0.2}Y_{0.15}O_{3-\delta}$ proton-conducting material determined using different nanoindentation methods, Journal of the European Ceramic Society 40(15) (2020) 5653-5661.
DOI: 10.1016/j.jeurceramsoc.2020.07.044.

3.1 Introduction

Already the works by Iwahara et al. [1-3] on perovskite-type oxide solid solutions based on cerate or zirconate, in particular $SrCeO_3$ and $BaCeO_3$. generated worldwide interest regarding applications related to hydrogen separation at intermediate temperatures. Especially Perovskite-based oxides showed remarkable proton conductivities [4]. In fact, $BaCeO_{3-\delta}$-based materials revealed the highest proton conductivity of all the competing materials under a water-containing atmosphere in the temperature range of 400 - 800 °C [4]. It has been reported that particularly Y and Zr doping can enhance proton conductivity and reduce the problem of poor chemical resistance to H_2O, CO_2 and H_2S, which has long been an unsolved challenge [4-13]. Recent reports have shown that $BaCe_{0.65}Zr_{0.2}Y_{0.15}O_{3-\delta}$ (BCZ20Y15) exhibits both good chemical stability and protonic conductivity [14-17]. BCZ20Y15 has, therefore, been considered as a promising material, which can form, in particular in a composite with $Ce_{0.85}Gd_{0.15}O_{2-\delta}$ (GDC15), a dual-phase proton-conducting membrane with a remarkable H_2 permeation [17].

Under application relevant conditions, a hydrogen separation membrane is operated at intermediate temperatures (600 – 800 °C) and is potentially exposed to high pressure differences across its thickness. Under these conditions, the membrane must maintain its structural and geometrical stability, ideally over an operation period of several years. Hence, the mechanical reliability is of critical concern. Despite the progress regarding conductivity and chemical stability, no systematic investigation of the mechanical properties of BCZ20Y15 has yet been reported. Elastic modulus, hardness and fracture toughness of similar materials, such as $BaCeO_3$-based perovskite materials with different stoichiometries have been reported as ~ 110 GPa, ~ 7 GPa and ~ 1 $MPa\cdot\sqrt{m}$, respectively [18-20]. These materials usually have the unsolved problem, though, of forming carbonates in a CO_2-containing environment leading to poor thermochemical stability [15, 21-23].

Elastic modulus, hardness and fracture toughness values are often derived via indentation testing [24-26]. However, for the determination of the elastic modulus, impulse excitation testing is suggested to be more representative of macroscopic long-range behavior, while deriving of the data from the geometry-specific resonance frequency [27] requires specimens with specific shape and dimensions. Fracture toughness data derived on the basis of conventional indentation testing typically show significant deviations related to specimen preparation and testing as well as analysis procedure, rendering alternative characterization methods very important. As an alternative, the micro-pillar indentation splitting test was recently developed by Sebastiani et al. [28-30] on the basis of sharp indentations into micro-pillars prepared via focused ion beam (FIB) milling. The pillar splitting method was developed with the aim of characterizing microscale intrinsic fracture toughness on the basis of the critical load values visible as pop-in effects in the load-displacement curves acquired during the indentation process.

Compared to the conventional Vickers-indentation-based fracture toughness test method (VIF) and other currently available microscale mechanical testing methods, e.g., single and double cantilever testing [31], the micro-pillar test method offers several advantages including its ease of application. Note, post-test measurement of the crack length, a factor that is critical for VIF and highly dependent on the image acquisition, is not necessary [32, 33]. Any potential residual stress, that might be induced by stoichiometric gradients or differences in thermal expansion in the case of a thin film on a substrate, is fully released and do not affect the test if the pillars have an aspect ratio of height to diameter between 1 and 4 [34]. Compared to FIB-machined micro-cantilever fracture geometries, difficulties related to friction coefficient calibration and possible Ga^+ ion implantation at the root of the stress-concentrating notch can be avoided [30, 31]. However, also in the case of pillar-splitting size effects were observed, which were related to the FIB-preparation [34]. Although it is not necessary to determine the crack length, the validity of the splitting experiment needs to be confirmed since inaccuracies in the indenter tip positioning can result in an underestimation of the fracture toughness [34].

In this work, investigations of the mechanical properties of BCZ20Y15 are reported. The study involved testing at different length scales, which yielded consistent results for the elastic modulus and hardness, confirming the overall uniformity of the processed material. The fracture experiments at the macro- and microscales exhibit differences, which can be explained by the presence of pores causing irregular crack patterns.

3.2 Experimental

BCZ20Y15 samples were prepared by a solid state reaction method (SSR). $BaCO_3$ (99%, Sigma Aldrich), CeO_2 (99.9%, Sigma Aldrich), ZrO_2 (99%, Sigma Aldrich), and Y_2O_3 (99%, Sigma Aldrich) were used as starting materials. In the process, precursor powders were mixed in stoichiometric ratios and ball-milled in ethanol for 24 hours. The resultant mixtures were dried at 80 °C and then calcined at 1300 °C for 5 h in air. 0.5 wt. % NiO (99%, Sigma Aldrich) [17] was added as sintering aid after pre-calcination in order to obtain dense samples. In order to obtain powders with a fine and homogeneous grain size, calcined BCZ20Y15 powders were ball-milled (ZrO_2 balls, 3.5 mm diameter, weight ratio powder : balls : ethanol = 1 : 2 : 3) in ethanol for 24 h. Afterwards, the mixtures were dried and sieved through a 160 µm mesh.

Bulk membranes were then uniaxially pressed into a disc shape under a pressure of ~ 20 MPa for 5 minutes to obtain pellets with green density of ~ 60%, and diameter and thickness of ~ 27 mm and ~ 1 mm, respectively. The samples were subsequently sintered at 1500 °C for 5 hours in air with a constant heating / cooling rate of 5 $K \cdot min^{-1}$.

The crystal structure and phase purity of the sintered samples was characterized using an EMPYREAN (PANalytical) diffractometer with parafocusing Bragg-Brentano geometry, employing a Cu-LFF-tube (40 kV / 40 mA), a BBHD mirror, 0.04 rad soller slits, and a PIXcel3D detector. X-ray diffraction (XRD) patterns were recorded at room temperature using a step scan procedure (0.4 s per step, 0.013 ° per step size) in the 2θ range of 5 – 90 °.

The microstructures and topographies were assessed by a Zeiss SUPRA 50VP field emission scanning electron microscope (SEM, Zeiss Microscopy GmbH, Oberkochen, Germany). Before observations were made, the respective specimen was embedded in epoxy resin, ground sequentially using SiO_2 sandpaper with 400 and 2000 grit size and then polished using 6 μm and 1 μm diamond suspension. The final polishing was conducted using 50 nm colloidal silica polishing suspension. The image analysis software Image J [35] was used to determine the grain size and porosity from the SEM images. An Archimedes method was used to determine the density of the BCZ20Y15 specimens. The theoretical density was calculated from the observed lattice parameters and the unit cell contents of the current composition. The results were compared with the theoretical density of the parent compound $BaCeO_3$ from Springer database [36].

An impulse excitation test was conducted following the procedures outlined in the ASTM standard [37]. Depth-sensing indentation testing was carried out using a Nano Test Vantage system (MicroMaterials, Ltd., Wrexham, UK) equipped with a diamond Berkovich tip. Elastic modulus and hardness were determined from the load-displacement curves under load control following the procedure developed by Oliver and Pharr [38, 39]. The reduced modulus (E_r) was calculated using:

$$E_r = \frac{\sqrt{\pi} \cdot S}{2 \cdot \beta \cdot \sqrt{A_p(h_c)}} \tag{3.1}$$

where S is the contact stiffness determined from the unloading slope, β a tip-dependent geometry factor assumed as 1.034, A_p the projected contact area, and h_c the contact depth at the maximum load P_{max}. The plane strain modulus (E^*) then corresponds to:

$$E^* = \frac{1}{\frac{1}{E_r} - \frac{1-\nu_i^2}{E_i}} \tag{3.2}$$

where E_i is the elastic modulus and ν_i Poisson's ratio of the diamond indenter tip assuming 1141 GPa and 0.07, respectively. Young's modulus E_{IT} was then calculated from E^* using Poisson's ratio of the sample ν_s, which is typically 0.3 for ceramics, using:

$$E_{IT} = E^* \cdot (1 - \nu_s^2) \tag{3.3}$$

The hardness H_{IT} was determined from the maximum load and the corresponding contact area:

$$H_{IT} = \frac{P_{max}}{A_p} \tag{3.4}$$

30 indents were performed at a loading rate of 2 mN/s to the maximum loads of 20 and 200 mN. Both thermal drift and frame compliance corrections were applied. The distance between indents was 15 µm and 90 µm at 20 mN and 200 mN, respectively.

Fracture toughness data were derived using the conventional Vickers-indentation-based fracture toughness method [40] at applied loads of 3 N, 5 N and 10 N and by the micro-pillar indentation splitting test utilizing a Berkovich tip indenter [28-30]. The crack length induced by the Vickers indentation impression was measured immediately after the test to avoid subcritical crack growth effects [41]. The empirical Equation 5, which was developed for the half-penny crack mode, was used to calculate the apparent fracture toughness K_{IC} [42]:

$$K_{IC} = 0.016 \left(\frac{E}{H}\right)^{\frac{1}{2}} \left(\frac{P}{c^{3/2}}\right) \tag{3.5}$$

where c is the crack length determined from micrographs, E and H from nanoindentation.

Pillars with nominal diameters of 5 µm, 10 µm and 15 µm were FIB-milled using an Auriga Crossbeam workstation (Zeiss Microscopy GmbH, Oberkochen, Germany) operated at 30 kV, 4 nA. A typical pillar is shown in Figure 3.1.

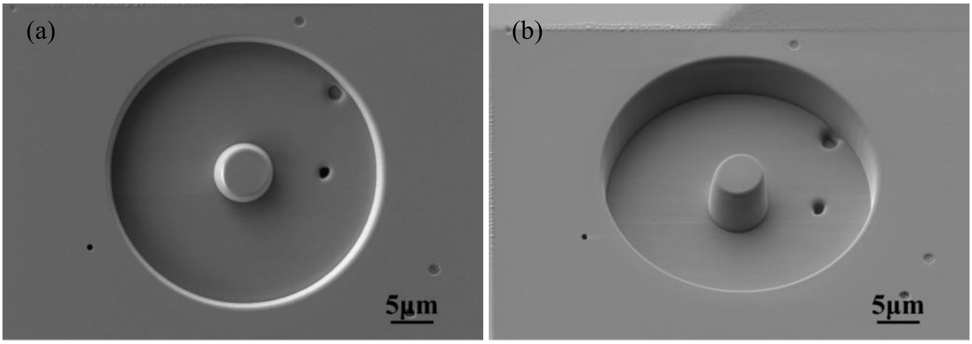

Figure 3.1 Scanning electron micrographs of a FIB-milled pillar in BCZ20Y15 before testing, (a) top view of a 5 µm pillar, (b) side view of the same pillar, tilt angle 56°.

In total 17 pillars were prepared, six each for the diameters of 10 and 15 µm and five with a nominal diameter of 5 µm. The pillars were not ideal cylinders but rather exhibited a slight taper (approximately 7 degrees) being comparable to values reported in the literature [41]. For the further analysis, the diameter of the pillar top was used [28-30, 41, 43]. Table 3.1 summarizes the actual pillar diameters, which were used for evaluation of the fracture toughness values.

Table 3.1 Measured pillar diameters.

	Pillar No.					
Nominal diameter [µm]	A	B	C	D	E	F
5	6.0	6.0	6.0	5.9	5.9	-
10	11.7	11.6	11.5	11.7	11.6	11.6
15	16.2	16.2	15.9	16.1	14.9	15.0

For the sake of clarity, the nominal diameter will be used for the discussion of the results, e.g., 5 µm group. The trench around the pillars was ~ 5 µm wide to allow for observation of cracks on the side surface of the pillars after testing. The load was applied at a loading rate of 2.5 mN/s and pop-ins reflect the pillar splitting.

The fracture toughness values are then calculated using the following equation [30]:

$$K_{IC} = \gamma \cdot \frac{P_c}{R^{3/2}} \tag{3.6}$$

where P_c is the critical load at pop-in, γ is a dimensionless coefficient that includes the influence of elastic-plastic properties and R is the radius of the pillar. The coefficient γ (Equation 3.6) was initially calculated by means of the finite element method [30], while in later works a linear relationship between γ and E / H was derived, which holds as long as $7 \leq E / H \leq 21$ [44, 45]:

$$\gamma = 0.0149\frac{E}{H} + 0.057 \tag{3.7}$$

Using this equation along with the experimentally determined elastic modulus and hardness from nanoindentation, γ takes a value of ~ 0.32.

3.3 Results and discussion

3.3.1 Phase constituents and microstructure

The material's crystalline structure was verified by XRD and the mean grain size was ~ 13 µm (Figure 3.2b). The porosity was less than 1% as estimated based on the SEM micrographs using Image J [35]. The Archimedes density was divided by the theoretical density [36] to obtain the relative density, which was more than 99%, corroborating the result based on the image analysis.

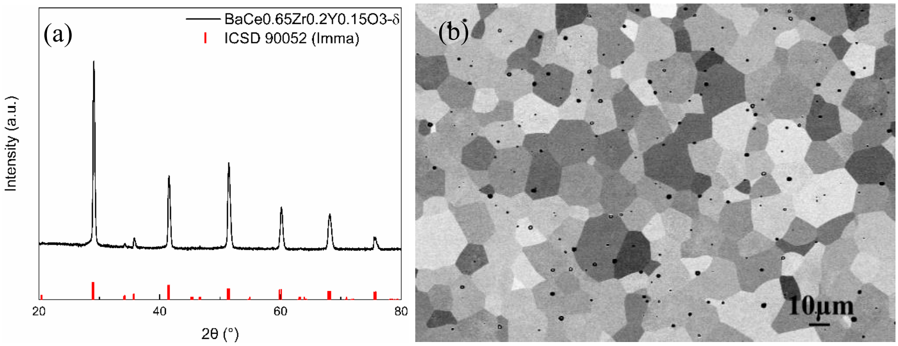

Figure 3.2 (a) XRD pattern of BCZ20Y15. All peaks are related to BCZ20Y15. (b) SEM image (back-scattered mode) of BCZ20Y15. The contrast differences are due to different crystal orientations and the black spots are pores, which took up less than 1% of the surface area.

The XRD results indicate that, with 0.5 wt% NiO as sintering aid, after sintering at 1500 °C for 5 h, the sample corresponds to single-phase BCZ20Y15 with an orthorhombic structure identified according to the ICSD 90052 (red markers in Figure 2a). Peaks related to NiO were not observed in the XRD pattern, very likely due to the small amount of NiO. Alternatively, NiO might be dissolved in the perovskite lattice or form a BaY_2NiO_5 phase [46]. The detected orthorhombic crystal structure with the space group *Imma* at room temperature for BCZ20Y15 is consistent with that reported by Rebollo et al. [17, 47, 48].

3.3.2 Elastic modulus and hardness

As a global property of BCZ20Y15, the elastic modulus was determined by an impulse excitation test (IET). The frequencies of the first and second natural vibration mode were analyzed from the amplitude-time relationship, yielding ~ 16000 Hz and ~ 28000 Hz, respectively, which served as a basis for the elastic modulus calculation using the relationships given in [37]. The IET results yielded a global elastic modulus of 118 ± 4 GPa, which agrees well with the value determined from the nanoindentation tests. The microscale elastic modulus of BCZ20Y15 determined from nanoindentation did not show a load dependence and was determined to be 117 ± 6 GPa and 116 ± 2 GPa for 20 mN and 200 mN, respectively. Similarly, no load effect was observed for the hardness, which corresponded to 6.8 ± 0.6 GPa and 6.4 ± 0.2 GPa, respectively, for the two applied loads (Figure 3.3).

The good agreement of the modulus values determined from the two independent methods supports the validity of the results and also confirms the high quality of the sample since often elastic modulus values are affected by porosity or material inhomogeneities.

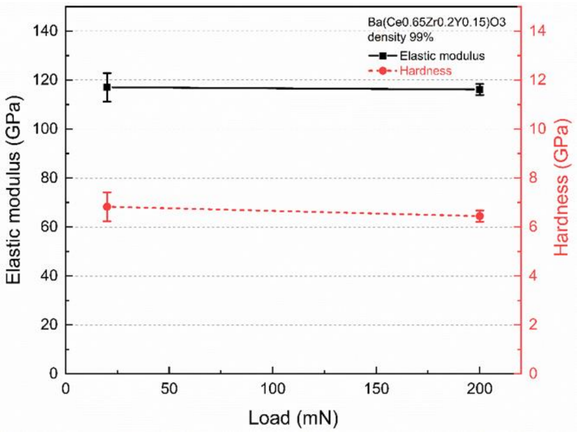

Figure 3.3 Elastic modulus and hardness of BCZ20Y15 for applied loads of 20 mN and 200 mN.

3.3.3 Fracture toughness

The fracture toughness was determined from micrographs of Vickers indents and micropillar splitting (Figure 3.4).

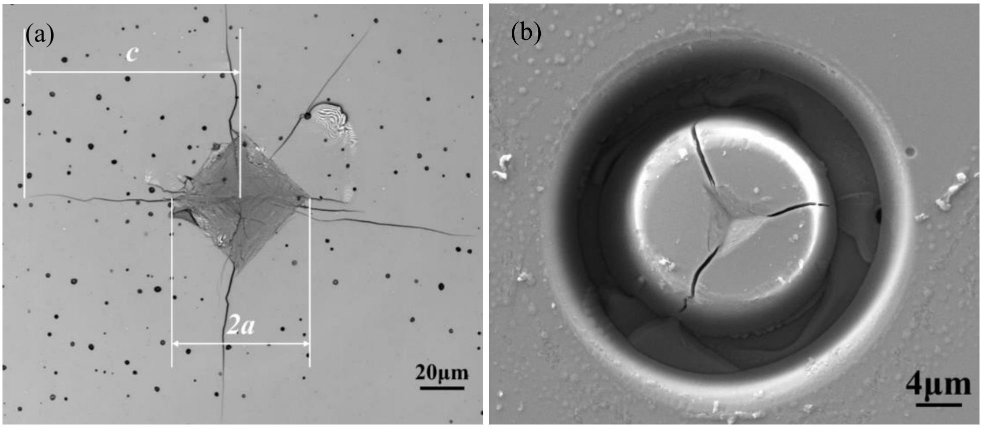

Figure 3.4 The fracture toughness was determined by the VIF approach and micropillar splitting. (a) Laser scanning microscope micrograph of a Vickers indent into BCZ20Y15 after loading with 10 N. The crack length *c* was used to determine the fracture toughness following the methodology outlined in [42]. (b) FIB machined micropillar with 15 µm diameter after testing showing the typical three-fold symmetry of the crack patterns.

The ratio of *c*/*a* (Figure 4.4 (a)), where *c* is the length from the indentation center point to the end of the crack tip and *a* half of the length of the indentation impression diagonal, was verified to be larger than 2.5 for all loads, which usually corresponds to a half-penny crack mode [42]. For the loads of 3, 5, and 10 N, the fracture toughness was determined to be ~ 0.6 MPa·√m (see also Figure 3.7 below), with only a slight dependency on the applied load that is within the limits of experimental uncertainty.

Representative load-displacement curves of the pillar splitting tests, along with post-test observation micrographs, are presented in Figure 3.5. In general, there is good agreement between the curves of the three different pillar sizes and with the loading curve of an indent into the bulk of the sample (Figure 3.5 (a)), which is critical to ensure the validity of the results [41, 44]. The slight deviation between these curves and the reference curve results is probably a result of thermal drift correction, which could not be performed for the pillar splitting tests due to the fracture preventing the hold period needed upon unloading. However, the thermal drift only affects the displacement measurement, which is not needed to determine the fracture toughness. The load signal is not affected by thermal fluctuations. The fracture toughness averaged over all pillar tests is 0.93 ± 0.15 MPa·√m, which is in the range typical of ceramics [18, 19, 49].

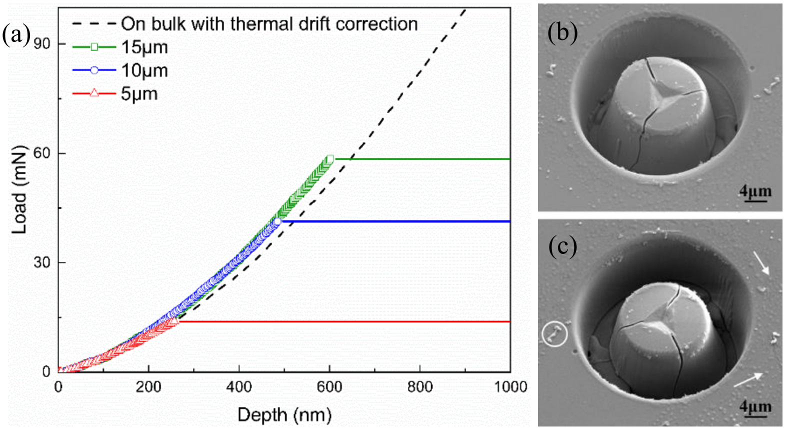

Figure 3.5 (a) Representative load-displacement curves obtained for the three groups of pillars and on bulk (as reference). (b, c) SEM images a split 15 µm diameter pillar imaged at a tilt angle of 26° and at different rotation angles). Residue on the surface (marked by arrows in c) indicates Ga+ contamination from the FIB preparation. Before imaging in the SEM but post-testing, the sample was coated with Ir, which presents as ribbons on the surface (circle in c).

The indents were all positioned within the central 10% region of the pillars, as exemplified in Figure 3.4 (b). Therefore, any unusual behavior related to positioning inaccuracies can be ruled out [34]. All pillars exhibited the typical 3-way splitting (angle of 120° required) with the cracks going straight down to the substrate as shown in Figures 3.5 (b) and (c). No obvious secondary crack or crack deflection was observed. The residue on the surface surrounding the pillars (marked by arrows in Figure 3.5 (c)) indicates surface contamination from Ga^+ implantation into the surface resulting from the FIB preparation. In the case of Si, the presence of a ~ 20 – 30 nm thick amorphous layer was observed after FIB preparation, which was reported to have caused a ~ 50% increase of the fracture toughness for single-crystalline Silicon [34]. Our elemental analysis by energy-dispersive X-ray spectroscopy (EDX) revealed that the Ga+ was mainly concentrated at the edge of pillar (see Figure 3.6) similar as reported in [41]. Hence, the indentation position appears to be at a sufficiently large distance away from the region affected by the Ga^+.

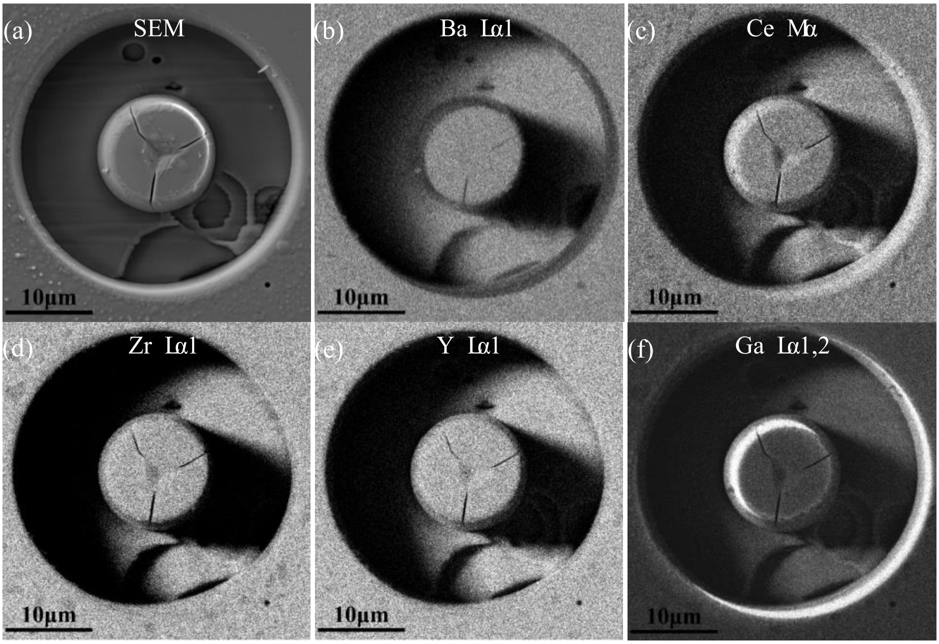

Figure 3.6 EDX element mapping of a 10 µm pillar after testing showing (a) the SEM micrograph and the elemental distributions (b) Ba, (c) Ce, (d) Zr, (e) Y, (f) Ga. The shadow, which exists in every element mapping, is a result of the topography of the sample surface. Due to the trench surrounding the pillar, no signal from the shadow region can be received by the EDX detector. If an EDX analysis is performed only for selected points on a sample rather than in the form of mappings, the selected location needs to be carefully chosen to avoid erroneous results due to this shadowing effect.

The fracture toughness values of BCZ20Y15 from the different methods are summarized in Figure 3.7.

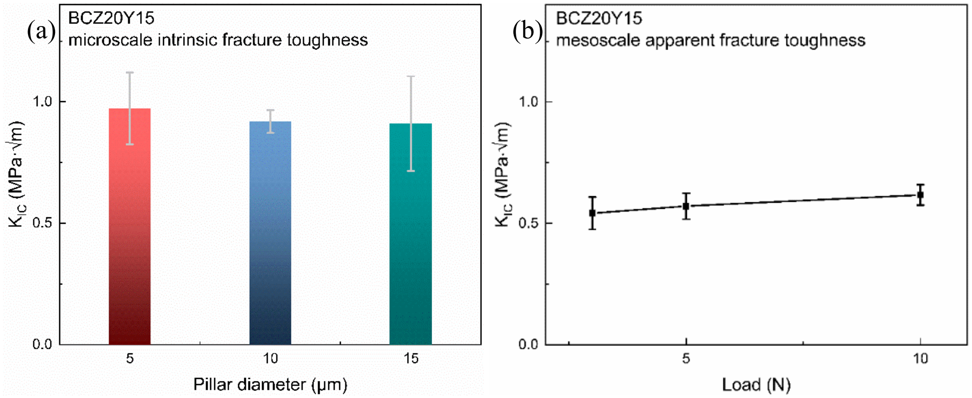

Figure 3.7 Comparison of the fracture toughness values determined by micropillar splitting and Vickers indentation, which yield values for the microscale intrinsic (a) and mesoscale apparent (b) fracture toughness, respectively.

The fracture toughness determined from pillar splitting is almost independent of the pillar size and therefore unaffected by the FIB preparation. According to the investigation by Lauener et al. [34], the increase in fracture toughness with decreasing pillar size is more pronounced when the pillar diameter is smaller than a critical value of ~ 10 μm. However, in the current case, even the 5 μm pillars showed only a very small increase of the average value compared to the 10 μm and 15 μm pillars. When the error bars are taken into consideration, this difference appears to be negligible.

A clear difference between the fracture toughness values determined by the two methods that probe the material on different length scales can be seen. The mesoscale values based on Vickers indentation are significantly lower than the microscale ones determined from micropillar splitting. R-curve behavior as basis of the difference obtained between these two methods is ruled out since within the range of pillar sizes (micro-pillar test) and applied loads (VIF), within each individual test method, no difference was observed. The BCZ20Y15 is isotropic and homogeneous, and no differences are expected. Therefore, the fracture patterns were investigated in more detail. As already indicated in Figure 4a, the crack paths appear irregular indicating that the VIF results should be viewed as an estimate. A series of Vickers impressions with a load of 1 N was placed along a line and the BCZ20Y15 sample was split manually to assess the crack patterns underneath the impressions (Figure 3.8).

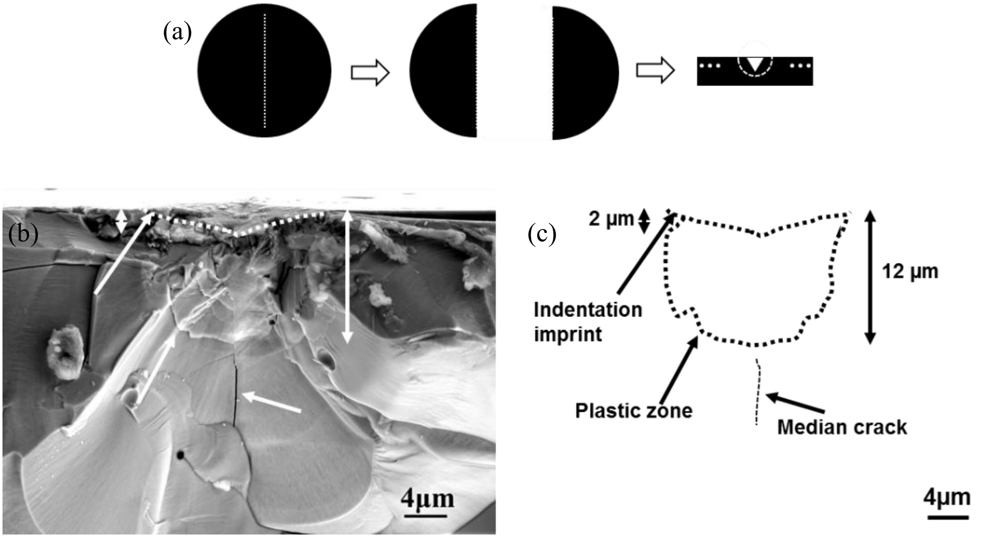

Figure 3.8 The crack mode was investigated by characterization of the cross section underneath Vickers impressions. (a) Schematic drawing of the preparation procedure. (b) SEM micrograph showing the fracture zone underneath a Vickers impression. (c) Drawing of the characteristic features in the deformed zone.

A clear plastic zone pattern was observed underneath the Vickers impression and an obvious median crack was found, which is a characteristic of the half-penny crack mode [42]. Figure 3.8 also confirms that the crack propagation mode is trans-granular since no grains or grain boundaries can be observed in the cross-section. The irregular crack patterns, bifurcation and delamination might be responsible for the lower mesoscale values. The VIF method indeed gives a rough estimate of the fracture toughness, which allows for any easy comparison of different materials. The determination of the crack length and the actual crack patterns represent uncertainties and the values determined of course need to be interpreted with caution. In this case, the irregular crack patterns occurred due to the presence of pores, which very likely led to fracture occur more readily.

Since the pillar splitting method only takes into account the necessary energy and load to propagate the cracks, additional secondary cracks, which might form above a critical load, will not influence the derived fracture toughness [41], which is a clear advantage of the pillar splitting method.

We would like to discuss one pillar in more detail, though, since it exhibited a comparably low fracture toughness of ~ 0.7 MPa·√m in contrast to ~ 0.9 MPa·√m averaged over all tested pillars. The pillar had a nominal diameter of 15 µm and exhibited the expected three-fold crack pattern resulting from a well-positioned indent (Figure 3.9).

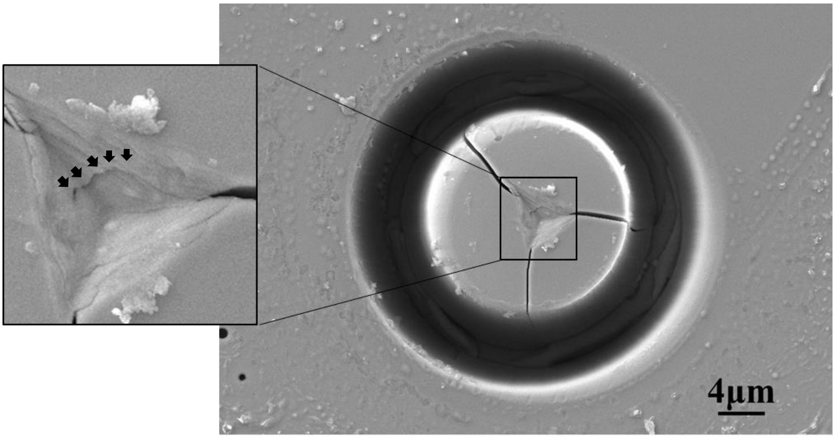

Figure 3.9 Detailed SEM investigation of the 15 µm pillar No. D (Table 3.1). The arrows indicate the positions of the crack-like feature inside the indent.

The microstructural analysis revealed a faint crack-like feature inside the indent (marked by arrows in Figure 3.9), which was apparently caused by pores right underneath the surface as revealed by FIB milling of sequential cross-sections (Figure 3.10). In the outer part of the pillar (Figure 3.10 (a)), the crack can clearly be seen (marked as 1 in Figure 3.10 (a)) with the expected appearance. Crack-like features (marked as 2 in Figure 3.10 (a)) are curtaining artifacts resulting from the FIB preparation. Towards the center, a more varied pattern is observed. The cross-section through the center of the pillar (Figure 3.10 (b)), exhibits a well-defined plastic zone (3 in Figure 3.10 (b)) and a median crack directly underneath the plastic zone (4 in Figure 3.10 (b)). This observation is in consistent with the expected half-penny crack mode for a Vickers-indentation-based fracture mechanism [42]. Based on the theory developed by Lawn et al. [50], the initial crack nucleation location for this crack type should be a median crack starting at the region edge of the plastic zone. In general, no crack should be observed in the plastic zone, which is also the case in the current study. However, in the high magnification micrograph in Figure 3.10 (c), a round crack-like feature in the surface (5 in Figure 3.10 (c)) can be seen, which likely is the trace of a pore collapsed during the indentation test but likely showing more ready cracking (reduced fracture load) resulting in a lower fracture toughness value. Evidence for crack deflection at pores can be observed at the bottom of a pillar cross-section (6 in Figure 3.10 (d)). While the pillar splitting is affected less by inhomogeneities in the volume of the material, pores close to the surface can reduce the value of the fracture toughness determined and, in general, the surface of the pillars needs to be inspected.

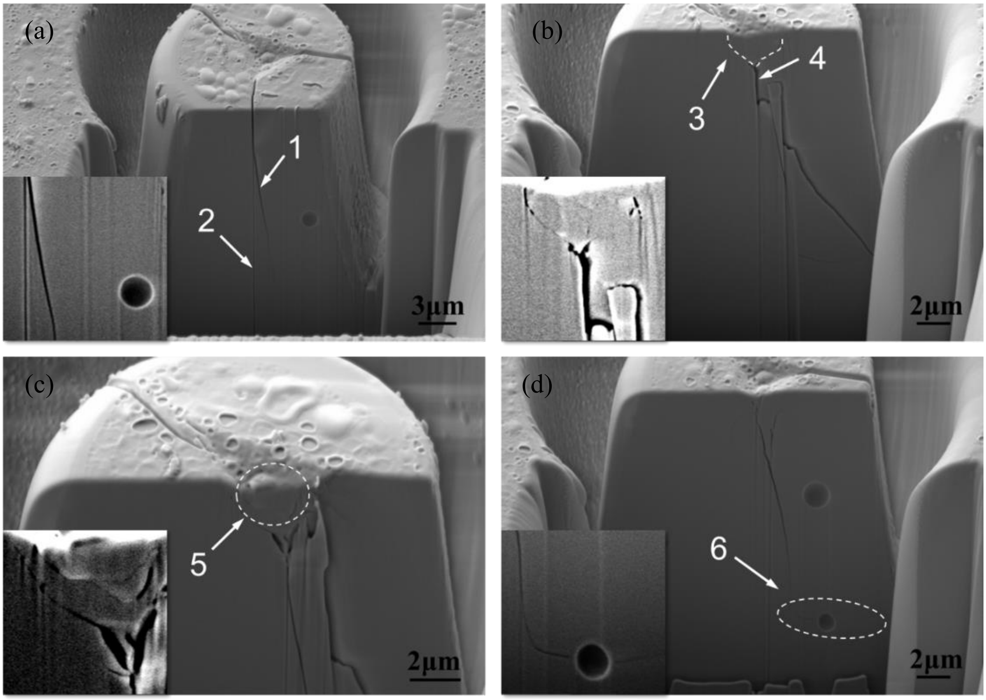

Figure 3.10 SEM micrographs of sequential FIB cross sections through the 15 µm diameter pillar D reveal the details of the fracture process. (a) Cross-section in the outer region with a straight crack (1) and curtaining artifacts (2), (b) cross-section through the center of the pillar showing the plastic zone (3) and the median crack (4), (c) cross-section through the crack-like feature shown in Figure 3.9 indicating the collapse of a pore (5). (d) pore at the bottom of cross section through the pillar showing clear crack deflection (6). Brightness and contrast of the SEM micrographs were adjusted to emphasize the subtle features of the fracture patterns.

3.4 Conclusions

The mechanical properties of the proton conducting ceramic BCZ20Y15 were determined applying different micro and macroscale testing methods. Consistent values of the elastic modulus were determined on different length scales corroborating the validity of the values determined. The hardness determined using different maximum loads did not show a dependence on the depth, which reflects the high quality and homogeneity of the material tested. The values of approximately 120 GPa and 7 GPa for the elastic modulus and the hardness, respectively, are in a range typical of ceramic materials and comparable to the properties of similar materials used as transport membranes [18-20]. The microscale intrinsic fracture toughness determined by micropillar splitting yielded higher values than the Vickers indentation based analysis, which probes a larger volume of the material. A detailed microstructural analysis clearly revealed the existence of pores and crack deflection. The presence of a pore close to the surface of one of the pillars is likely responsible for the lower fracture toughness value derived in the pillar splitting test. The VIF based apparent fracture toughness represents a rough estimate due to irregular crack patterns, bifurcation and delamination affecting the derived mesoscale values [51].

BCZ20Y15 appears to be suitable for further studies related to its application relevant properties. In addition to permeation and long-term chemical as well as operational stability, the long-term deformation behavior at elevated temperatures and failure probabilities as well as subcritical crack growth are of particular interest. Furthermore, in the real application, usually a “sandwich” structure rather than a single thin membrane is used and the support will likely affect the whole component’s mechanical stability. In addition, potential stoichiometric changes, degradation effects, and the interplay with mechanical characteristics will have to be studied.

References

[1] H. Iwahara, Technological challenges in the application of proton conducting ceramics, Solid State Ionics 77 (1995) 289-298.

[2] H. Iwahara, H. Uchida, K. Morimoto, High Temperature Solid Electrolyte Fuel Cells Using Perovskite-Type Oxide Based on $BaCeO_3$, Journal of the Electrochemical Society 137(2) (1990) 462-465.

[3] H. Iwahara, H. Uchida, K. Ono, K. Ogaki, Proton conduction in sintered oxides based on BaCeO3, Journal of the Electrochemical Society 135(2) (1988) 529-533.

[4] K. Kreuer, Proton-conducting oxides, Annual Review of Materials Research 33(1) (2003) 333-359.

[5] G. Chiodelli, L. Malavasi, C. Tealdi, S. Barison, M. Battagliarin, L. Doubova, M. Fabrizio, C. Mortalo, R. Gerbasi, Role of synthetic route on the transport properties of $BaCe1\text{-}xYxO_3$ proton conductor, Journal of Alloys and Compounds 470(1-2) (2009) 477-485.

[6] E. Fabbri, A. D'Epifanio, E. Di Bartolomeo, S. Licoccia, E. Traversa, Tailoring the chemical stability of Ba $(Ce_{0.8-x}Zr_x)$ $Y_{0.2}O_{3-\delta}$ protonic conductors for intermediate temperature solid oxide fuel cells (IT-SOFCs), Solid State Ionics 179(15-16) (2008) 558-564.

[7] S. Haile, G. Staneff, K. Ryu, Non-stoichiometry, grain boundary transport and chemical stability of proton conducting perovskites, Journal of Materials Science 36(5) (2001) 1149-1160.

[8] J. Li, J.-L. Luo, K.T. Chuang, A.R. Sanger, Chemical stability of Y-doped Ba (Ce, Zr) O_3 perovskites in H_2S-containing H_2, Electrochimica Acta 53(10) (2008) 3701-3707.

[9] A. Magrez, T. Schober, Preparation, sintering, and water incorporation of proton conducting $Ba_{0.99}Zr_{0.8}Y_{0.2}O_{3-\delta}$: comparison between three different synthesis techniques, Solid State Ionics 175(1-4) (2004) 585-588.

[10] S. Stotz, C. Wagner, Die löslichkeit von wasserdampf und wasserstoff in festen oxiden, Berichte der Bunsengesellschaft für physikalische Chemie 70(8) (1966) 781-788.

[11] C.W. Tanner, A.V. Virkar, Instability of $BaCeO_3$ in H_2O-Containing Atmospheres, Journal of The Electrochemical Society 143(4) (1996) 1386-1389.

[12] S. Tao, J.T. Irvine, Conductivity studies of dense yttrium-doped BaZrO3 sintered at 1325 C, Journal of Solid State Chemistry 180(12) (2007) 3493-3503.

[13] L. Yang, S. Wang, K. Blinn, M. Liu, Z. Liu, Z. Cheng, M. Liu, Enhanced sulfur and coking tolerance of a mixed ion conductor for SOFCs: $BaZr_{0.1}Ce_{0.7}Y_{0.2-x}Yb_xO_{3-\delta}$, Science 326(5949) (2009) 126-129.

[14] S. Barison, M. Battagliarin, T. Cavallin, S. Daolio, L. Doubova, M. Fabrizio, C. Mortalo, S. Boldrini, R. Gerbasi, Barium Non-Stoichiometry Role on the Properties of $Ba_{1+x}Ce_{0.65}Zr_{0.20}Y_{0.15}O_{3-\delta}$ Proton Conductors for IT-SOFCs, Fuel cells 8(5) (2008) 360-368.

[15] S. Barison, M. Battagliarin, T. Cavallin, L. Doubova, M. Fabrizio, C. Mortalo, S. Boldrini, L. Malavasi, R. Gerbasi, High conductivity and chemical stability of $BaCe_{1-x-y}Zr_xY_yO_{3-\delta}$ proton conductors prepared by a sol–gel method, Journal of Materials Chemistry 18(42) (2008) 5120-5128.

[16] L. Doubova, S. Barison, S. Boldrini, M. Fabrizio, C. Mortalo, C. Pagura, Conductivity studies of sol-gel prepared $BaCe_{0.85-x}Zr_xY_{0.15}O_{3-\delta}$ solid electrolytes using impedance spectroscopy, Journal of applied electrochemistry 39(11) (2009) 2129-2141.

[17] E. Rebollo, C. Mortalo, S. Escolástico, S. Boldrini, S. Barison, J.M. Serra, M. Fabrizio, Exceptional hydrogen permeation of all-ceramic composite robust membranes based on $BaCe_{0.65}Zr_{0.20}Y_{0.15}O_{3-\delta}$ and Y-or Gd-doped ceria, Energy & Environmental Science 8(12) (2015) 3675-3686.

[18] Y.-P. Fu, C.-S. Weng, Effect of rare-earth ions doped in $BaCeO_3$ on chemical stability, mechanical properties, and conductivity properties, Ceramics International 40(7) (2014) 10793-10802.

[19] R. Sažinas, C. Bernuy-López, M.A. Einarsrud, T. Grande, Effect of CO_2 Exposure on the Chemical Stability and Mechanical Properties of $BaZrO_3$-Ceramics, Journal of the American Ceramic Society 99(11) (2016) 3685-3695.

[20] Z. Zhang, J. Koppensteiner, W. Schranz, J.B. Betts, A. Migliori, M.A. Carpenter, Microstructure dynamics in orthorhombic perovskites, Physical Review B 82(1) (2010) 014113.

[21] K. Katahira, Y. Kohchi, T. Shimura, H. Iwahara, Protonic conduction in Zr-substituted $BaCeO_3$, Solid State Ionics 138(1-2) (2000) 91-98.

[22] X. Ma, J. Dai, H. Zhang, D.E. Reisner, Protonic conductivity nanostructured ceramic film with improved resistance to carbon dioxide at elevated temperatures, Surface and Coatings Technology 200(5-6) (2005) 1252-1258.

[23] P. Sawant, S. Varma, B. Wani, S. Bharadwaj, Synthesis, stability and conductivity of $BaCe_{0.8-x}Zr_xY_{0.2}O_{3-\delta}$ as electrolyte for proton conducting SOFC, international journal of hydrogen energy 37(4) (2012) 3848-3856.

[24] R.O. Silva, J. Malzbender, F. Schulze-Küppers, S. Baumann, O. Guillon, Mechanical properties and lifetime predictions of dense $SrTi_{1-x}Fe_xO_{3-\delta}$ ($x = 0.25, 0.35, 0.5$), Journal of the European Ceramic Society 37(7) (2017) 2629-2636.

[25] V. Stournari, W. Deibert, M. Ivanova, C. Krautgasser, R. Bermejo, J. Malzbender, Mechanical properties of tape casted Lanthanum Tungstate for membrane substrate application, Ceramics International 42(14) (2016) 15177-15182.

[26] L. Wang, R. Dou, G. Wang, Y. Li, M. Bai, D. Hall, Y. Chen, A case study of mechanical properties of perovskite-structured $Ba_{0.5}Sr_{0.5}Co_{0.8}Fe_{0.2}O_{3-\delta}$ oxygen transport membrane, Journal of the European Ceramic Society 38(2) (2018) 647-653.

[27] J. Wei, G. Pećanac, J. Malzbender, Review of mechanical characterization methods for ceramics used in energy technologies, Ceramics international 40(10) (2014) 15371-15380.

[28] M. Sebastiani, E. Bemporad, F. Carassiti, N. Schwarzer, Residual stress measurement at the micrometer scale: Focused ion beam (FIB) milling and nanoindentation testing, Philosophical Magazine 91(7-9) (2011) 1121-1136.

[29] M. Sebastiani, C. Eberl, E. Bemporad, G.M. Pharr, Depth-resolved residual stress analysis of thin coatings by a new FIB–DIC method, Materials Science and Engineering: A 528(27) (2011) 7901-7908.

[30] M. Sebastiani, K. Johanns, E.G. Herbert, F. Carassiti, G.M. Pharr, A novel pillar indentation splitting test for measuring fracture toughness of thin ceramic coatings, Philosophical Magazine 95(16-18) (2015) 1928-1944.

[31] M. Sebastiani, K. Johanns, E.G. Herbert, G.M. Pharr, Measurement of fracture toughness by nanoindentation methods: Recent advances and future challenges, Current Opinion in Solid State and Materials Science 19(6) (2015) 324-333.

[32] A. Davydok, B.N. Jaya, O. Robach, O. Ulrich, J.-S. Micha, C. Kirchlechner, Analysis of the full stress tensor in a micropillar: Ability of and difficulties arising during synchrotron based μLaue diffraction, Materials & Design 108 (2016) 68-75.

[33] Q. Liu, A. Roy, V.V. Silberschmidt, Size-dependent crystal plasticity: From micro-pillar compression to bending, Mechanics of Materials 100 (2016) 31-40.

[34] C.M. Lauener, L. Petho, M. Chen, Y. Xiao, J. Michler, J.M. Wheeler, Fracture of Silicon: Influence of rate, positioning accuracy, FIB machining, and elevated temperatures on toughness measured by pillar indentation splitting, Materials & Design 142 (2018) 340-349.

[35] C.A. Schneider, W.S. Rasband, K.W. Eliceiri, NIH Image to ImageJ: 25 years of image analysis, Nature methods 9(7) (2012) 671-675.

[36] https://materials.springer.com/isp/crystallographic/docs/sd_1414391 (the database was accessed on 10.07.2019).

[37] ASTM, E. (1876). Standard test method for dynamic young’s modulus, shear modulus, and poisson’s ratio by impulse excitation of vibration. Annual Book of ASTM Standards, 3, 1876.

[38] W.C. Oliver, G.M. Pharr, An improved technique for determining hardness and elastic modulus using load and displacement sensing indentation experiments, Journal of materials research 7(6) (1992) 1564-1583.

[39] W.C. Oliver, G.M. Pharr, Measurement of hardness and elastic modulus by instrumented indentation: Advances in understanding and refinements to methodology, Journal of materials research 19(1) (2004) 3-20.

[40] J. Gong, Determining indentation toughness by incorporating true hardness into fracture mechanics equations, Journal of the European Ceramic Society 19(8) (1999) 1585-1592.

[41] A.-N. Wang, J.F. Nonemacher, G. Yan, M. Finsterbusch, J. Malzbender, M. Krüger, Mechanical properties of the solid electrolyte Al-substituted $Li_7La_3Zr_2O_{12}$ (LLZO) by utilizing micro-pillar indentation splitting test, Journal of the European Ceramic Society 38(9) (2018) 3201-3209.

[42] C.B. Ponton, R.D. Rawlings, Vickers indentation fracture toughness test Part 1 Review of literature and formulation of standardised indentation toughness equations, Materials Science and Technology 5(9) (1989) 865-872.

[43] A.M. Korsunsky, M. Sebastiani, E. Bemporad, Residual stress evaluation at the micrometer scale: Analysis of thin coatings by FIB milling and digital image correlation, Surface and Coatings Technology 205(7) (2010) 2393-2403.

[44] M. Ghidelli, M. Sebastiani, K.E. Johanns, G.M. Pharr, Effects of indenter angle on micro‐scale fracture toughness measurement by pillar splitting, Journal of the American Ceramic Society 100(12) (2017) 5731-5738.

[45] A.J. Lunt, G. Mohanty, T.K. Neo, J. Michler, A.M. Korsunsky, Microscale resolution fracture toughness profiling at the zirconia-porcelain interface in dental prostheses, Micro+ Nano Materials, Devices, and Systems, International Society for Optics and Photonics, 2015, p. 96685S.

[46] J. Tong, D. Clark, L. Bernau, A. Subramaniyan, R. O'Hayre, Proton-conducting yttrium-doped barium cerate ceramics synthesized by a cost-effective solid-state reactive sintering method, Solid State Ionics 181(33-34) (2010) 1486-1498.

[47] C. Mortalò, E. Rebollo, S. Escolástico, S. Deambrosis, K. Haas-Santo, M. Rancan, R. Dittmeyer, L. Armelao, M. Fabrizio, Enhanced sulfur tolerance of $BaCe_{0.65}Zr_{0.20}Y_{0.15}O_{3-\delta}$-

$Ce_{0.85}Gd_{0.15}O_{2-\delta}$ composite for hydrogen separation membranes, Journal of Membrane Science 564 (2018) 123-132.

[48] C. Mortalò, A. Santoru, C. Pistidda, E. Rebollo, M. Boaro, C. Leonelli, M. Fabrizio, Structural evolution of $BaCe_{0.65}Zr_{0.20}Y_{0.15}O_{3-\delta}$-$Ce_{0.85}Gd_{0.15}O_{2-\delta}$ composite MPEC membrane by in-situ synchrotron XRD analyses, Materials Today Energy 13 (2019) 331-341.

[49] P.-F. Yang, D.-L. Chen, S.-R. Jian, S.-W. Lee, C.-J. Tseng, Mechanical Properties of $Ba_{1x}K_xCe_{0.6}Zr_{0.2}Y_{0.2}O_{3-\delta}$ Oxides by Nanoindentation, Procedia Engineering 79 (2014) 599-605.

[50] B. Lawn, A. Evans, A model for crack initiation in elastic/plastic indentation fields, Journal of Materials Science 12(11) (1977) 2195-2199.

[51] G.D. Quinn, R.C. Bradt, On the Vickers indentation fracture toughness test, Journal of the American Ceramic Society 90(3) (2007) 673-680.

CHAPTER 4

High temperature compressive creep behaviour of $BaCe_{0.65}Zr_{0.2}Y_{0.15}O_{3-\delta}$ in air and 4% H_2/Ar

Abstract

The proton conductive material $BaCe_{0.65}Zr_{0.2}Y_{0.15}O_{3-\delta}$ has great potential for the separation and purification of hydrogen. However, due to the demanding application conditions regarding both temperature and atmosphere, the elevated temperature structural stability needs to be characterized and warranted. Hence, in this research work, the elevated temperature compressive creep behavior of $BaCe_{0.65}Zr_{0.2}Y_{0.15}O_{3-\delta}$ in the temperature regime of 850 °C to 1200 °C was studied in both air and 4% H_2/Ar as a function of the applied stress. The results indicate different creep mechanisms depending on atmosphere and temperature range. While dislocation creep was observed in 4% H_2/Ar over the full range, a dislocation creep mechanism was observed in air at temperatures $\leq$ 1050 °C and a diffusional creep mechanism at temperature $\geq$ 1100 °C. A detailed microstructural analysis of the post-creep test specimens revealed that the exposure to oxygen leads to localized stoichiometric changes and a decomposition at the surface.

This chapter has been published as: W. Zhou, J. Malzbender, W. Deibert, O. Guillon, R. Schwaiger, A. Nijmeijer, W.A. Meulenberg, High temperature compressive creep behavior of $BaCe_{0.65}Zr_{0.2}Y_{0.15}O_{3-\delta}$ in air and 4% H_2/Ar, Journal of the American Ceramic Society 104(6) (2021) 2730-2740.

DOI: 10.1111/jace.17715.

4.1 Introduction

$BaCeO_3$-based materials have raised considerable interest due to their high protonic conductivity [1-7]. In particular, when Zr is partially substituted into the parent material $BaCeO_3$, enhanced chemical resistances against H_2O, CO_2 and H_2S are observed [8-14]. Hence, $BaCe_{0.65}Zr_{0.2}Y_{0.15}O_{3-\delta}$ (BCZ20Y15) showed both good protonic conductivity and chemical stability [8, 14-16] and is therefore considered to be a promising material for hydrogen separation applications. BCZ20Y15, when combined with Gd-doped CeO_2, forms a dual-phase proton conductive membrane with a remarkably high H_2 permeance [14].

Under application relevant conditions, these proton conducting membranes are operated at an intermediate temperature (~ 600 – 800 °C) and are potentially exposed to high pressure differences across the membrane [14, 17]. Under such harsh conditions, the membrane must maintain its structural and geometrical stability, ideally over an operation period of many years, which means that the mechanical stability is a matter of concern.

During operation of these membranes, stresses acting on the membrane components [17, 18], combined with the elevated temperature, potentially lead to the occurrence of creep. Creep becomes noticeable for ceramics typically when the temperature is higher than around half of the melting temperature [19]. From an engineering point of view, the membrane material should not creep more than 1% per year in a compressive creep mode (corresponding to $\sim 3 \times 10^{-10}$ /s) to warrant reliable long-term operation [20]. Creep behavior of the material at elevated temperature under constant loads can be used to demonstrate the material's thermomechanical reliability and creep resistance [21-24], which can potentially guide membrane component design.

The aim of this work is to characterize the creep behavior of BCZ20Y15 at elevated temperatures from 850 °C to 1200 °C, in both air and 4% H_2/Ar. Based on the observed creep behaviors, a detailed investigation of the creep mechanisms was carried out. Based on post-creep microstructure investigation, the main factors that are critical to the mechanical and operational stability are discussed.

4.2 Experimental

BCZ20Y15 samples were prepared by a solid state reaction method (SSR). $BaCO_3$ (99%, Sigma Aldrich), CeO_2 (99.9%, Sigma Aldrich), ZrO_2 (99%, Sigma Aldrich), and Y_2O_3 (99%, Sigma Aldrich) were used as starting materials. In the process, precursor powders were mixed in stoichiometric ratios and ball-milled in ethanol for 24 h. The resultant mixtures were dried at 80 °C and then calcined at 1300 °C for 5 h in air. 0.5 wt. % NiO (99%, Sigma Aldrich) [14] was added as sintering aid after pre-calcination in order to obtain dense samples. In order to obtain powders with a fine and homogeneous grain size, calcined BCZ20Y15 powders were ball-milled (ZrO_2 balls, 3.5 mm diameter, weight ratio powder : balls : ethanol = 1 : 2 : 3) in ethanol for 24 h. Afterwards, the mixtures were dried and sieved through a 160 μm mesh.

Bar-shaped samples were then uniaxially pressed under a pressure of ~ 20 MPa for 5 minutes to obtain a green density of ~ 60%, with a specimen geometry of ~ 5 × 5 × 40 mm^3. The samples were subsequently sintered at 1500 °C for 5 h in air at constant heating / cooling rates of 5 $K\cdot min^{-1}$.

Detailed information regarding the material preparation, crystal structure and phase purity of the sintered samples can be found in [25].

The microstructures were assessed by a Zeiss SUPRA 50VP field emission scanning electron microscope (SEM, Zeiss Microscopy GmbH, Oberkochen, Germany). Prior to the microstructural analysis, the specimen was embedded in epoxy resin, ground sequentially using SiO_2 sandpaper with 400 and 2000 grit size and then polished using 6 μm and 1 μm diamond suspensions. The final polishing was conducted using 50 nm colloidal silica polishing suspension. The image analysis software Image J [26] was used to determine the grain size and porosity from the SEM images. Energy dispersive X-ray (EDX) spectroscopy was carried out at 10 kV accelerating voltage using a X-Max 80 detector and the AZtec data acquisition and analysis software package (Oxford Instruments Nanoanalysis, High Wycombe, United Kingdom).

For creep testing, BCZ20Y15 samples were cut by an electrical discharge machine into specimens with the dimension of ~ 4 × 4 × 10 mm^3. Similar as reported in [27-30], the steady-state creep rates were obtained by the application of long-term compressive tests at different temperatures and applied stresses. The details of the setup used for creep testing can be found in [27, 29, 30]. The creep tests in 4% H_2/Ar were carried out in the temperature range from 850 °C to 1000 °C (maximum temperature limited by the experimental setup) and in air from 1000 °C to 1200 °C under uniaxial compressive loads. The chosen test temperatures were higher than the material application temperature for a reliably creep behavior observation. A further extrapolation based on Arrhenius plot can help to estimate the creep condition of the material in the application temperature. The temperature was increased at a rate of 8 K/min, and kept constant after reaching the test temperature for two hours in order to allow the specimen to reach thermal equilibrium. A preload of ~ 2 N was applied during heating and thermal equilibrium to keep the specimen fixed in position. Stresses ranging from 30 to 80 MPa were applied to determine the creep rates. A maximum applied stress of ~ 95 MPa, at which the specimens fractured, had been determined beforehand. The minimum applied stress was fixed according to simulation results reported in literature [31] indicating that 30 MPa will likely occur under realistic gas separation operation conditions. The creep analysis was carried out on the basis of data that confirmed steady-state deformation and continued until the integral deformation reached ~ 100 μm or until a maximum test duration of 24 h was reached.

For the tests in 4% H_2/Ar, the chamber was firstly purged at room temperature with the gas until the oxygen partial pressure in the chamber was lower than 1 mbar (several hundred ppm oxygen content). During heating to the test temperature, the remaining oxygen in the chamber reacted with the H_2 resulting in ~ 0 ppm O_2 content at the test temperature. For the tests in air, the oxygen partial pressure was ~ 0.2 bar, which is distinctly different compared to the condition in the 4% H_2/Ar tests.

Every specimen was examined in subsequent steps of a defined testing scheme in one atmosphere, i.e. 850 °C / 30 MPa → 850 °C / 60 MPa → 850 °C / 80 MPa → 900 °C / 30 MPa …, which means that one specimen was tested under multiple thermal and mechanical load cycles at different temperatures in one atmosphere. This test scheme has proven successful as described in [32]. Some selected tests were additionally carried out with a separate specimen for one stress (80 MPa) at only two temperatures (1000 °C and 1200 °C) that verified the suitability of the test scheme.

The creep rate was determined from the slope in the secondary creep stage via linear regression fitting. Figure 4.1 shows a representative compressive creep deformation curve of BCZ20Y15 at 80 MPa and 1200 °C.

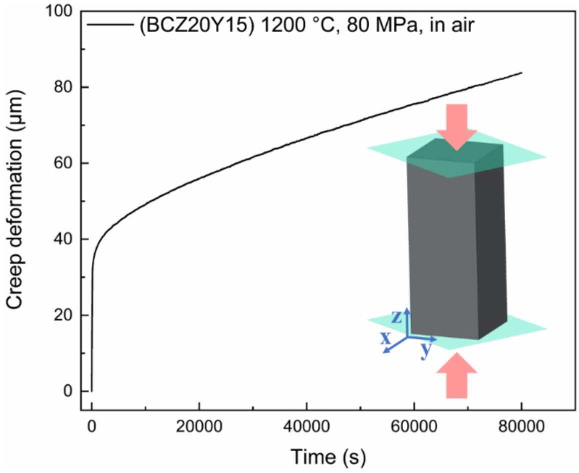

Figure 4.1 Representative creep deformation curve of BCZ20Y15 at a test temperature of 1200 °C and an applied stress of 80 MPa in air.

Steady state creep in the secondary stage (simply termed “creep rate” hereafter) is usually thermally activated. The resulting creep rate $\dot{\varepsilon}$ depends on the temperature T

and the applied compressive stress σ, and can be described by the following equation [27, 32, 33]:

$$\dot{\varepsilon} = \dot{\varepsilon_0} \cdot A \cdot \left(\frac{\sigma}{\sigma_0}\right)^n \cdot exp\left(-\frac{E_a}{RT}\right) \tag{4.1}$$

where A, n, E_a and R are the stress-independent constant (Dorn constant), stress exponent, activation energy for creep and gas constant, respectively. $\dot{\varepsilon_0}$ and σ_0 are 1 s^{-1} and 1 MPa, used for defining the dimensions of strain rate and stress.

The creep activation energy and stress exponent were obtained via global linear fitting of all results using the software “Origin”.

4.3 Results and discussion

4.3.1 Creep behaviour in 4% H_2/Ar

Figure 4.2 shows an Arrhenius plot of the creep rates of BCZ20Y15 versus the reciprocal absolute temperature in the temperature range from 850 °C to 1000 °C in 4% H_2/Ar for stresses ranging from 30 MPa to 80 MPa.

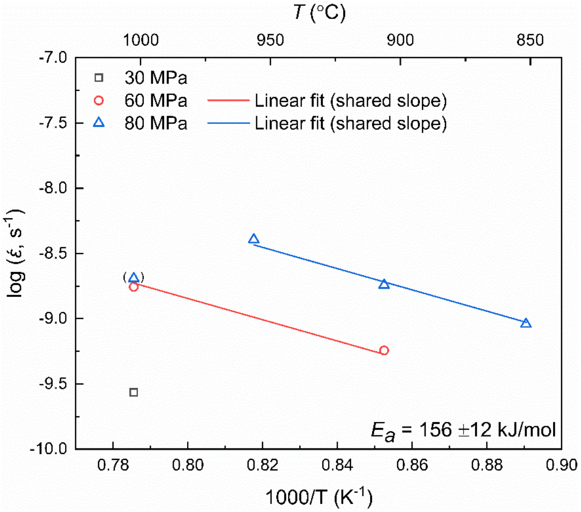

Figure 4.2 Arrhenius plot of the creep rates of BCZ20Y15 in 4% H_2/Ar for applied stresses ranging from 30 MPa to 80 MPa as a function of the inverse temperature. The data point of

1000 °C, 80 MPa (marked by the braces) was not included in the fit and the reasons will be discussed further down in the article.

The temperature limit of the furnace in 4% H_2/Ar was 1000 °C. Compared with the available phase diagrams of $BaCeO_3$ [34] and $BaZrO_3$ [35] for a rough estimation of BCZ20Y15's T_m (~ 2100 K), the applied temperatures are ~ 50% of the melting point, so it is reasonable that rather low creep rates were observed.

The creep activation energy was obtained via global linear fitting of all results using the software "Origin", meaning that the fitting lines in Figure 4.2 share a same slope. In another word, 5 points together were linear fitted to get their shared slope, rather than 2 points and 3 points being linear fitted separately. The derived activation energy is ~ 160 kJ/mol, indicating a rather weak temperature dependency for the temperature range of 850 – 1000 °C. It should be noted that the 1000 °C, 80 MPa data point was excluded from the activation energy calculation. This data point is associated with an unexpected behavior which will be discussed in more detail below. At the lowest applied compressive stress of 30 MPa, only at a temperature of 1000 °C creep was observed. Thus, this isolated data point was not included in the global linear fitting. However, it can still be mathematically evaluated to check if it fits the global linear fitting results. Furthermore, the consistency between the mathematical description and the experimentally derived creep rates indicates the reliability of the results. However, for very low creep rates, thermal drift and noise may affect the reliability of the data.

Figure 4.3 shows the logarithmic plot of the creep rates of BCZ20Y15 as a function of applied stresses for temperatures ranging from 850 – 1000 °C in 4% H_2/Ar.

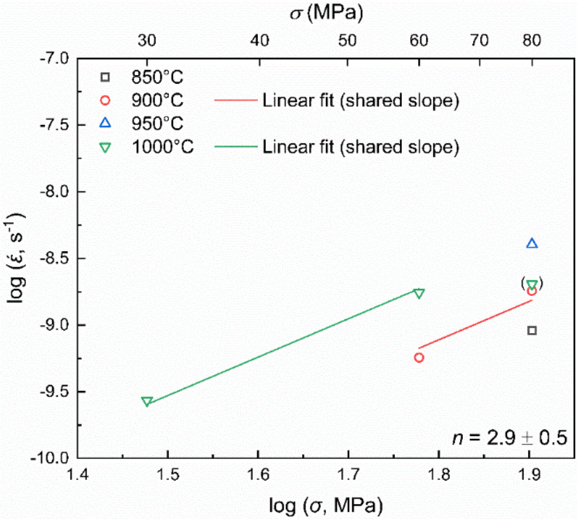

Figure 4.3 A double-logarithmic plot of the creep rates of BCZ20Y15 in 4% H_2/Ar as a function of applied compressive stresses for the temperature range of 850 – 1000 °C. The data point of 1000 °C, 80 MPa (marked by the braces) was not included in the fit and the reasons will be discussed further down in the article.

Since global linear fitting was performed to analyze the slope, 4 points were analyzed together to get the slope rather than 2 groups of 2 points. The derived stress exponent is $n \approx 3$, which usually indicates a dislocation creep mechanism [36]. Such a mechanism commonly occurs in metals but has also been reported for ceramics [19, 37]. This mechanism has been observed in particular for ceramic membrane materials such as LSCF [38] and STF [22]. The dislocation creep mechanism occurs typically under high stress and sufficiently high temperature enhancing the dislocation motion, which appears to be in agreement with the current testing conditions. The 850 °C, 80 MPa and 950 °C, 80 MPa data points can also be mathematically described by Equation 4.1, as mentioned above. Combined with the weak temperature dependency, the results from Figure 4.2 and 4.3 corroborate that the creep of BCZ20Y15 in 4% H_2/Ar, in the temperature and compressive stress ranges of 850 – 1000 °C, 30 MPa to 80 MPa, respectively, is governed by a dislocation creep mechanism. Note that, in case of a dislocation creep mechanism, the grain size will not influence the creep rate [36].

4.3.2 Microstructural investigations

Figure 4.4 shows the microstructures of BCZ20Y15 before and after creep in a 4% H_2/Ar atmosphere.

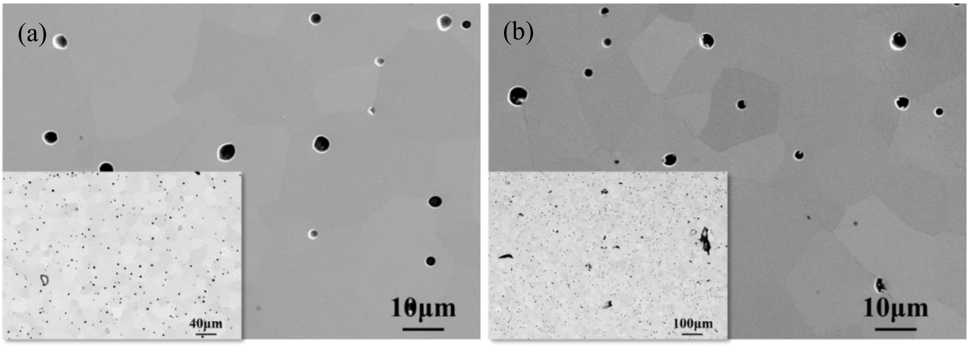

Figure 4.4 SEM micrographs of BCZ20Y15: (a) as-sintered specimen, and (b) specimen post-creep in 4% H_2/Ar. The insets show the polished sample surfaces at lower magnification, which were used for determining the density of the materials. The black spots on the polished surfaces are pores in the materials.

For both, the 4% H_2/Ar post-creep tested specimen and the as-sintered reference specimen, the densities were ~ 98%. The grain sizes were also similar and in both cases ~ 20 μm, indicating that there was no pronounced grain growth or densification during the creep test. Therefore, the observed deformation during creep tests can be attributed completely to the creep deformation of BCZ20Y15.

XRD based investigations were performed for post-creep test specimens after being exposed to the test series under H_2/Ar and air. There was no indication of secondary phase formation within the limitation of the sensitivity of XRD. Hence, complementary detailed EDX characterizations in particular for post-creep specimens surface region was considered to be necessary. The respective results are shown in Figure 4.5 and 4.13. These EDX results also support the XRD results obtained in the current work, i.e. only for the post-creep specimen, that was tested in air, a very thin decomposed layer in the proximity of the surface was observed.

For a detailed microstructural analysis, the material in the center of a specimen was characterized (Figure 4.5).

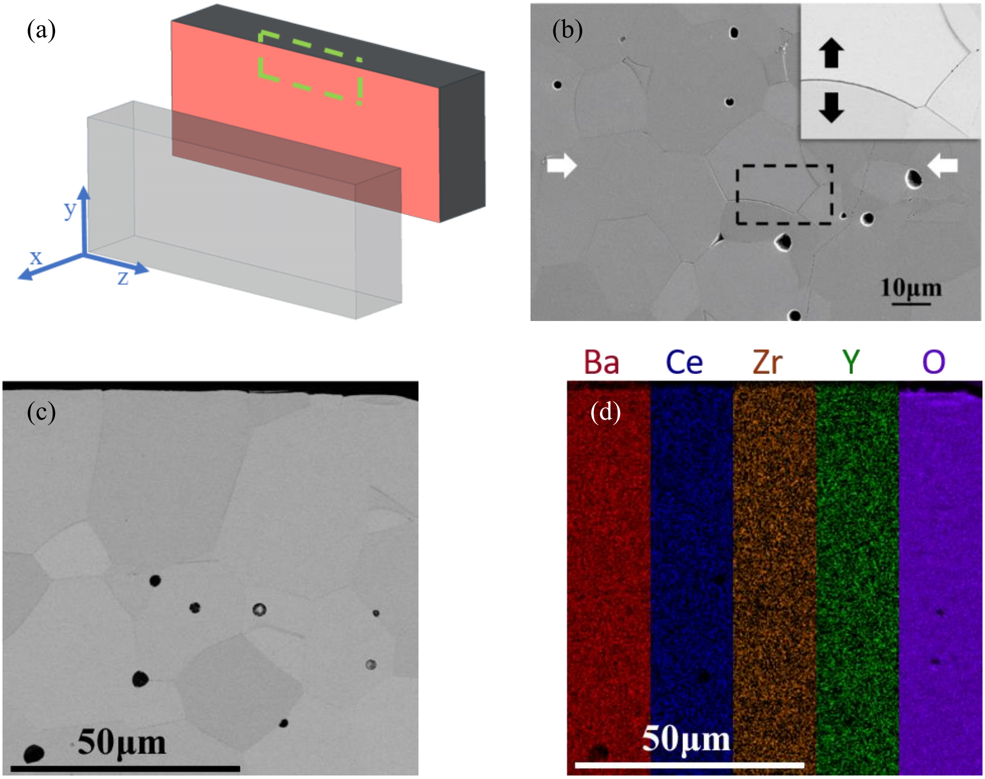

Figure 4.5 BCZ20Y15 was analyzed in more detail after creep in 4% H_2/Ar. (a) Schematic indicating the location in the sample, (b) SEM micrograph revealing grain boundary opening (marked by the black arrows) and loading direction (marked by the white arrows), (c) BSEM micrograph of a selected region which will be further analyzed via EDX in (d), (d) elemental analysis by EDX showing that all elements distribution homogeneous indicating no trace of decomposition.

A clear grain boundary opening was observed (Figure 4.5 (b)) at the location indicated in Figure 4.5 (a), similar as also reported in [24]. The gaping grain boundary is aligned with the direction of the compressive load applied, which was the longitudinal direction in Figure 4.5 (a), and agrees well with the observations in [24]. The stress tensor is complicated, but from a simplified stress model point of view, the specimen experienced compressive stress in the longitudinal direction (Z-direction) and tensile stress in transversal direction (Y-direction) in Figure 4.5 (a). The corresponding loading direction is marked by the white arrows on Figure 4.5 (b). EDX investigation was performed in the near surface region, since decomposition usually starts at the surface and then spreads deeper into the bulk of the specimen [32]. As shown in Figure 4.5 (c) and (d), comparison between topography and elemental mapping indicates that no noticeable decomposition.

4.3.3 Creep behaviour in air

Figure 4.6 shows an Arrhenius plot of the creep rates of BCZ20Y15 versus reciprocal absolute temperature from 1000 °C to 1200 °C in air for stresses of 30, 60 and 80 MPa.

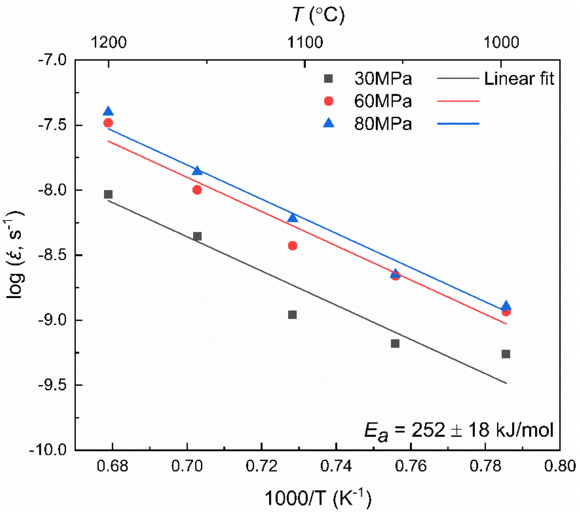

Figure 4.6 Arrhenius plot of the creep rates of BCZ20Y15 in air for applied compressive stresses ranging from 30 MPa to 80 MPa as a function of inverse temperature. All data points at different stress levels over the temperature range of 1000 °C – 1200 °C were included in the linear fit. Coefficient of determination (R^2) of the global linear fitting is ~ 0.96.

Since the creep tests in air were performed at higher temperatures, i.e. at ~ 70% of the melting point of BCZ20Y15 [34, 35], higher creep rates are expected compared to the 4% H_2/Ar case, as indeed observed in Figure 4.6. The derived activation energy is ~ 250 kJ/mol, which is significantly higher than the derived activation energy in the 4% H_2/Ar case (Figure 4.2), revealing a stronger temperature dependency.

Figure 4.7 shows the logarithmic plot of the creep rates of BCZ20Y15 as a function of applied stresses for the temperature ranging from 1000 – 1200 °C in air.

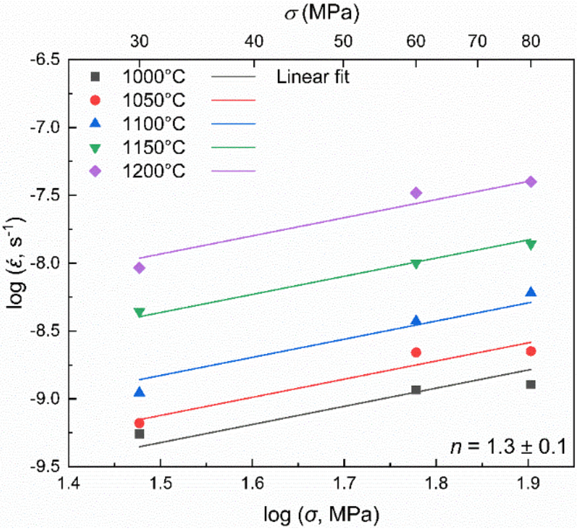

Figure 4.7 Double-logarithmic plot of the creep rates of BCZ20Y15 in air as function of the applied compressive stresses in the temperature range of 1000 – 1200 °C.

The derived stress exponent for the creep tests in air is ~ 1, which is usually associated with a diffusional creep mechanism [36]. In the case of diffusional creep, the creep rate depends on the diffusivity of the slowest ion moving along the shortest diffusion path [38, 39]. This mechanism typically occurs at very high temperature and relatively low applied stresses. While based on the data presented in Figure 4.6, diffusional creep might be predominant in the temperature and stress range. Upon closer inspection of Figure 4.6, a division into two regimes can be suggested, as shown in Figure 4.8.

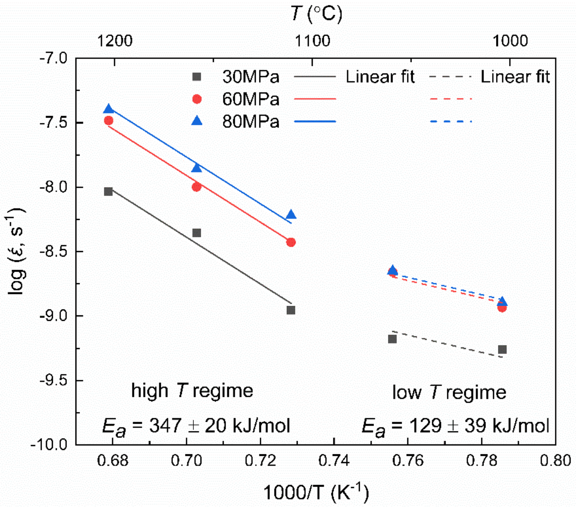

Figure 4.8 Arrhenius plot divided into a higher *T* and lower *T* regions according to the slopes of the creep rates of BCZ20Y15 in air for applied stress from 30 MPa to 80 MPa as a function of inverse temperature. It should be noted that global linear fitting was performed to analyze the slopes, 6 points in low *T* range being analyzed together to get their shared slope. This is where the errors of straight lines fitting coming from, especially in low *T* regime. Coefficient of determination (R^2) of high *T* regime fitting and low *T* regime fitting are ~ 0.99 and ~ 0.97, respectively.

The higher temperature region and lower temperature region have different slopes in the Arrhenius plot and thus the corresponding activation energies are significantly different, i.e. ~ 350 kJ/mol and ~ 130 kJ/mol, respectively.

The activation energy determined for the low *T* regime is close to the activation energy determined in the creep tests under 4% H_2/Ar atmosphere (Figure 4.2), also indicating a weak temperature dependency. Further analysis of the stress exponent also indicates that the creep mechanism in the high *T* and low *T* regimes might be different, as shown in Figure 4.9.

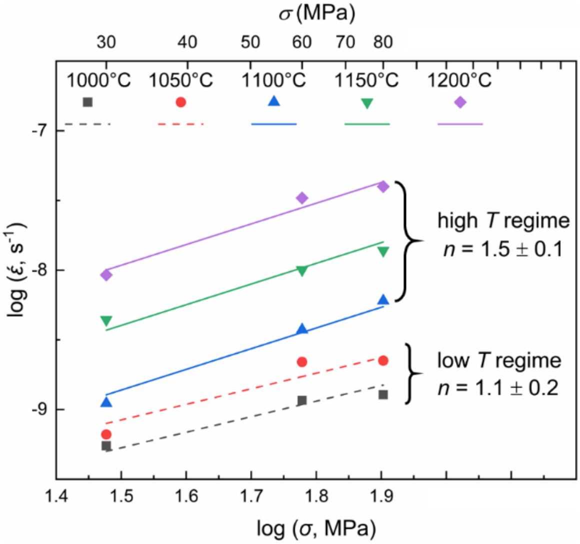

Figure 4.9 The double-logarithmic plot of the creep rate of BCZ20Y15 in air versus applied compressive stress indicates a sub division into a high *T* and low *T* regime, i.e. ≥ 1100 °C and ≤ 1050 °C, according to the slopes of the creep rates.

The stress exponent *n* is ~ 1 for the lower temperature regime. Combined with the corresponding activation energy, the temperature dependency appears to be weak in this regime and as does the load dependency. Therefore, in the regime of ~ 1050 and 1100 °C, the predominant creep mechanism might change. As discussed above, the temperature range from 850 °C to 1000 °C is associated with a dislocation creep mechanism, while diffusional creep determines the behavior at temperatures ≥ 1100 °C. It is therefore reasonable to assume that a transition regime exists, in which two mechanisms occur simultaneously. The presentation of the data in Figure 4.10 supports our assumption as further discussed below. In Figure 4.10, the creep behavior of BCZ20Y15 in air and in 4%H_2/Ar (indicated by full and open symbols, respectively) at ~ 1000 °C is shown.

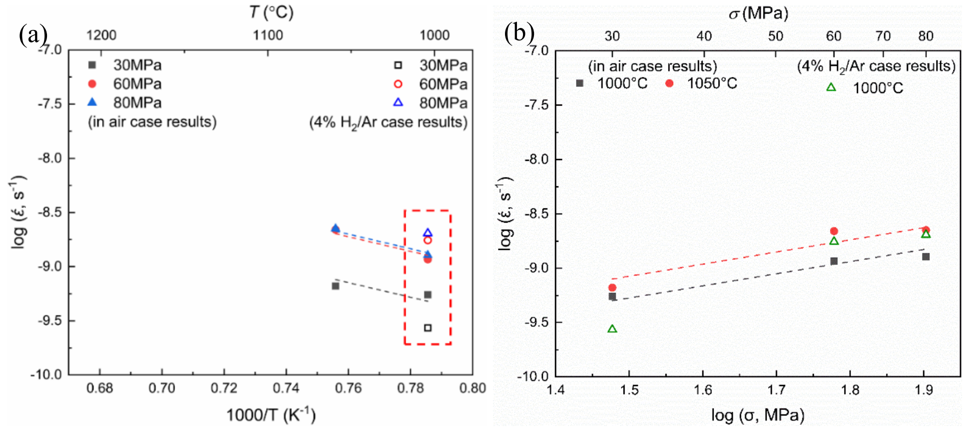

Figure 4.10 Combination and comparison of BCZ20Y15's creep behavior of both in air case results and in 4% H_2/Ar case results at ~ 1000 °C to reveal the transition regime of the predominant creep mechanism. (a) Arrhenius plot, (b) double-logarithmic plot. The red dash line box marked data reveals an identical relatively high/low relationship of creep behavior in different atmospheres.

In both atmospheres, the creep rates at 80 MPa and 60 MPa are almost equal and distinctly higher than at 30 MPa (data points inside the box in Figure 4.10 (a)). In other words, at 1000 °C the creep behaviors under different atmospheres are almost identical. From the double-logarithmic plot, it can be observed that for the 4% H_2/Ar case, at 1000 °C, the load dependency becomes weak when the applied stress is higher than 60 MPa, indicating that the data point of 80 MPa belongs to a regime where two mechanisms exist simultaneously. This provides additional evidence for the change of the creep mechanism and supports our decision to exclude the creep data at 1000 °C, 80 MPa, in 4% H_2/Ar, from the analysis in Figure 4.2. While the creep rate at 1000 °C, 30 MPa is rather low, and therefore more affected by noise and thermal drift, the parallel lines shown in Figure 4.3 confirm the reliability of the analysis.

Figure 4.11 combines the data shown in Figure 4.2 and Figure 4.8, presenting the creep behavior of BCZ20Y15 for the temperature range from 850 °C to 1200 °C, tested under applied compressive stresses ranging from 30 MPa to 80 MPa, in both 4% H_2/Ar atmosphere and in air.

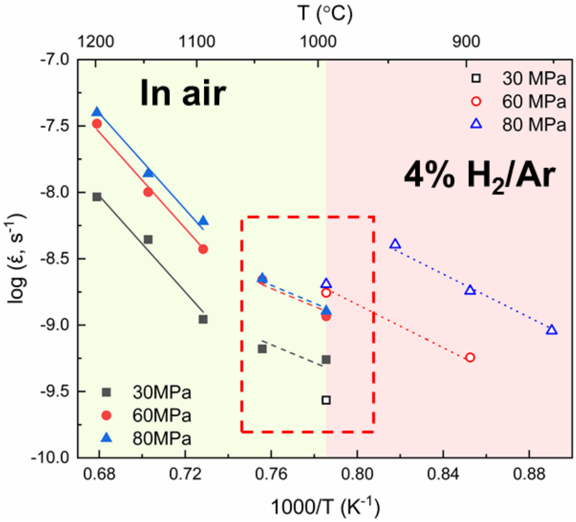

Figure 4.11 Arrhenius plot of the creep rates of BCZ20Y15 versus the reciprocal absolute temperature in both 4% H_2/Ar atmosphere and air, for the temperature range of 850 – 1200 °C, under compressive applied stress ranging from 30 MPa to 80 MPa. The red frame marked data indicates the transition regime of predominant creep mechanism, as also shown in Figure 4.10 (a).

Different regimes can be distinguished in Figure 4.11. At temperatures lower than ~ 1000 °C, in 4% H_2/Ar, dislocation creep mechanism is the predominant mechanism, while at temperatures higher than ~ 1100 °C, in air, a regime associated with diffusional creep is observed. At intermediate temperatures (~ 1000 °C, marked by the red frame), irrespective of the atmosphere, a shift in creep mechanism can be observed, as also shown in Figure 4.12.

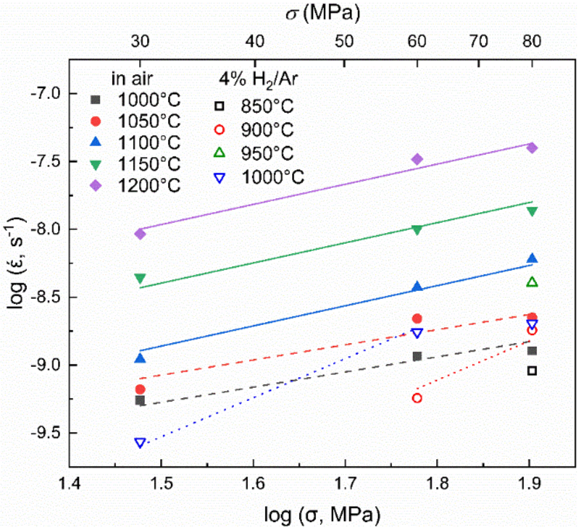

Figure 4.12 Double-logarithmic plot of the creep rate of BCZ20Y15 versus the applied compressive stress in both 4% H_2/Ar atmosphere and in air, at temperatures ranging from 850 to 1200 °C.

The three different slopes can be clearly observed in Figure 4.12, which is consistent with the three temperature regimes indicating different creep mechanisms in Figure 4.11.

The compressive creep behavior in Ar of a similar material, $BaCe_{0.8}Y_{0.2}O_{3-\alpha}$ (BCY20), at temperatures from 1200 °C to 1450 °C indicated a diffusional creep mechanism with a stress exponent of 1.1 ± 0.1 and an activation energy of 343 ± 30 kJ/mol [39]. These results are in good agreement with our findings regarding the creep behavior in air in the temperature range from 1100 °C to 1200 °C. The activation energy values are comparable, in particular when the error bars are taken into account.

4.3.4 Decomposition investigation

Figure 4.13 presents the microstructural observation of the post-creep specimen for the air case.

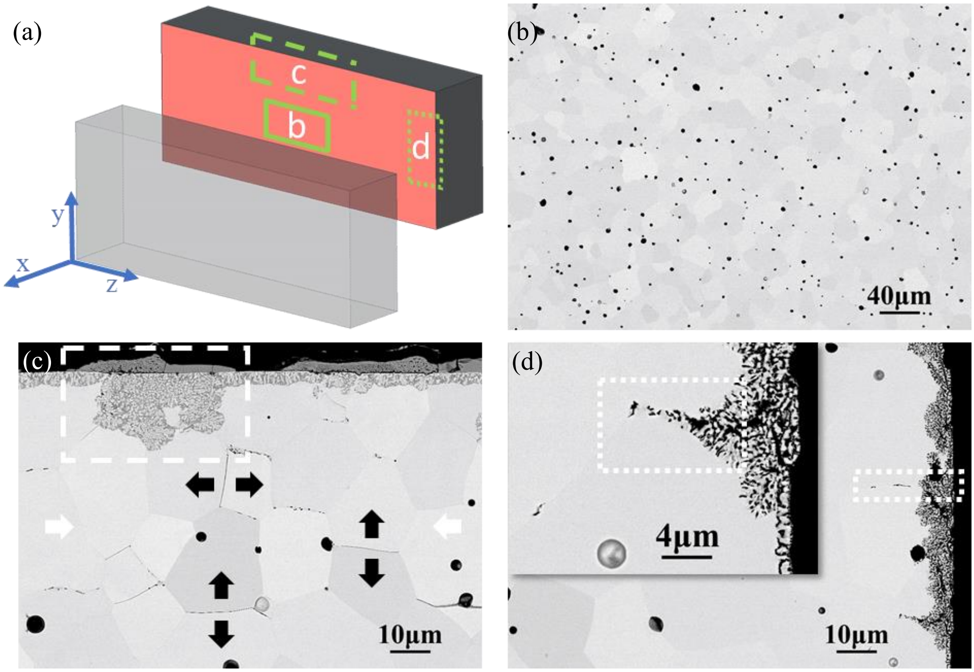

Figure 4.13 Microstructural observations after creep in air. (a) schematic of the location of the microstructural investigation on the polished post-creep specimen, (b) SEM micrograph of the central region showing porosity and grain structure, and (c, d) SEM micrographs of the near surface regions demonstrating the opening of the grain boundaries (marked by the black arrows; the white arrows indicate the loading direction) and material decomposition.

The density and grain size of the specimen after creep in air are ~ 98% and ~ 20 µm, respectively, and the same as determined for the as-sintered specimen Figure 4.4 (a). Hence, no indication of grain growth or densification during the creep test was observed and the deformation can be associated purely with the creep behavior. Moreover, since the grain size of the material in this work is significantly larger than the grain size (~ 9 µm) of BCY20 studied in [39], i.e. ~ 20 µm vs. ~ 9 µm, also the grain size exponent was considered for a comparison of the creep rates, as shown in Equation 4.2 [20].

$$\dot{\varepsilon} = \dot{\varepsilon_0} \cdot A \cdot \left(\frac{d}{d_0}\right)^{-m} \cdot \left(\frac{\sigma}{\sigma_0}\right)^{n} \cdot exp\left(-\frac{E_a}{RT}\right) \tag{4.2}$$

where *d* is the grain size and *m* the inverse grain size exponent, which has typically a value of 2 to 3 for a diffusional creep mechanism [19].

The creep rate of BCY20 in [39] is ~ 10^{-6} /s at 1200 °C under a compressive stress of ~ 80 MPa, as estimated from the data presented. Thus, the creep rate reported is two orders of magnitude higher compared to ~ 10^{-8} /s obtained in our work for the same stress/temperature combination. The distinct difference can be partially explained by the grain size, since the grain size of the material studied in this work is ~ 2 to 3 times larger than the one in [39]. Considering Equation 4.2, it is therefore reasonable that the creep rate obtained in this work is some orders of magnitude lower than reported in [39].

In addition to the grain size, differences in density might also contribute to the observed difference in the creep rates. The density of the BCY20 [39] appears lower (~ 90%) than the density of our material which has a density of ~ 98%, when comparing the image analysis results of the SEM micrographs. Under identical test conditions, the specimen with higher porosity will likely exhibit a higher creep rate as discussed in detail on the basis of the Minimum Solid Area (MSA) concept in [40, 41]. Moreover, the difference between creep rates for different porosities tend to become larger with increasing temperature [24].

As shown in Figure 4.13 (c), grain boundary opening can be clearly observed in the near-surface region (region c, marked in Figure 4.13 (a)), while the grain boundaries appeared to be intact in the central bulk region (region b in Figure 4.13 (a)) and close to the edge (region d in Figure 4.13 (a)) as can be seen in Figure 4.13 (b, d). The differences regarding microstructural changes are likely related to the different stress states in the three locations. The central bulk region shows no decomposition, as can be seen, but in both near-surface regions (Figure 4.13 (c, d)), the decomposition can be clearly seen.

In the region marked in Figure 4.13 (d), both decomposition and grain boundary opening can be observed. The decomposition spreads into the specimen starting from the surface and is enhanced by the presence of the grain boundaries. The opening of the grain boundaries might accelerate the decomposition, since oxygen can more easily reach sample regions located in the bulk. While based on Figure 4.13 (d), the decomposition might in turn also enhance the grain boundary opening, a more detailed investigation of the process would be needed to describe the synergistic interplay of decomposition and grain boundary opening.

After the creep test in 4% H_2/Ar atmosphere over the temperature range of 850 – 1000 °C, no decomposition was observed, while it had clearly occurred after creep in air at 1000 – 1200 °C. Apparently, the combination of temperature and oxygen partial pressure has a distinct effect on the decomposition behavior of the material. For BCY20, which was tested in Ar atmosphere at 1200 – 1450 °C [39], no decomposition was reported. Oxygen partial pressure might, thus, be responsible for the decomposition rather than temperature, since no enhanced decomposition was observed at higher temperature in [39].

Figure 4.14 shows a detailed elemental analysis of the degradation zone observed in our work.

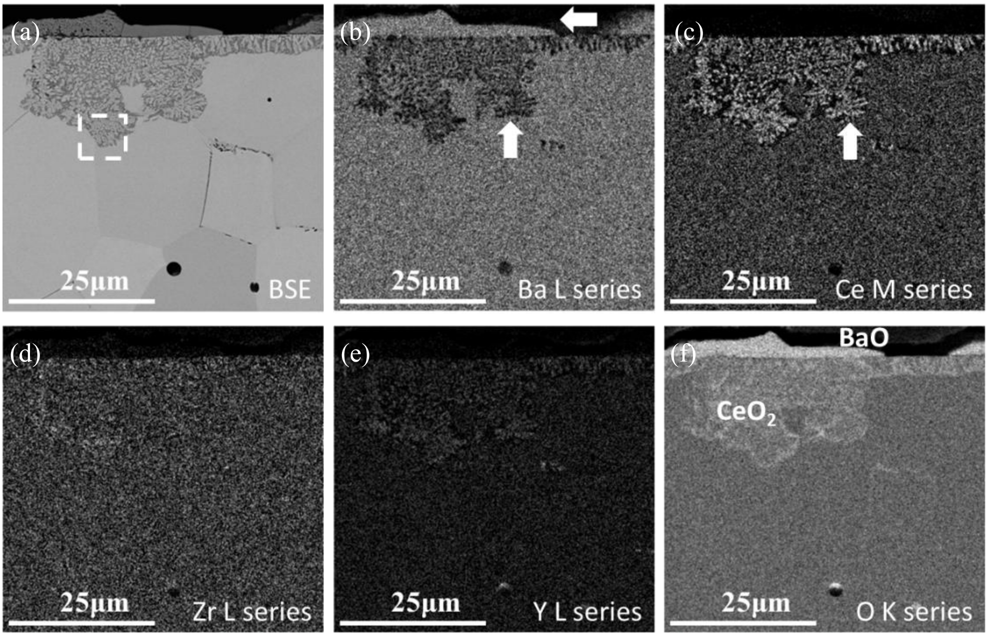

Figure 4.14 EDX element mapping of the degradation region on the post-creep in air specimen showing (a) the SEM micrograph indicating the decomposition spreading deeper following the grain boundary, and elemental distributions of (b) Ba (indicating Ba migration, as marked by the arrows, from dark contrast region to surface bright contrast region), (c) Ce (indicating Ce enrichment in the decomposition region, marked by arrow), (d) Zr (distributed homogeneously), (e) Y (showing slight compositional changes), (f) O (which indicates three different O levels in the region, i.e. the presence of additional two different phases with different O content).

The decomposition zone appears to propagate along the grain boundary, as shown in Figure 4.14 (a), marked by the frame, which is consistent with the micrographs in Figure 4.13 (d). EDX elemental mappings show contrast variations in the different regions indicating local differences in the elemental composition. The loss of Ba underneath the surface and the migration to the specimen surface can be clearly observed in Figure 4.14 (b). In the region of Ba loss, Ce enrichment has occurred, as shown in Figure 4.14 (c). Zr is distributed homogeneously exhibiting high stability against the decomposition, which is consistent with previous findings that Zr has high stability against chemical and thermal erosion [1-3, 11, 13, 15], while some local redistribution of Y can be noticed (Figure 4.14 (d) and (e)). Figure 4.14 (f) shows the distribution of O; combining Figure 4.14 (f) with Figure 4.14 (b) and (c), it is shown that the decomposition of the sample leads to the formation of BaO and CeO_2. Based on the above analysis, it can be concluded that the decomposition observed after creep in air at temperatures from 1000 to 1200 °C is induced by the oxygen partial pressure, as also reported for the degradation of, for example, Cr_2AlC [32].

4.4 Conclusions

The elevated temperature compressive creep behavior of BCZ20Y15 in different atmospheres was studied. From 850 °C to 1000 °C, in 4% H_2/Ar atmosphere, the stress exponent is ~ 3 and the activation energy ~ 160 kJ/mol, indicating a dislocation creep mechanism. For creep in the temperature range 1100 – 1200 °C, in air, the stress exponent is ~ 1 and the activation energy ~ 350 kJ/mol, corresponding to a diffusional creep mechanism. At ~1000 °C, a change of the predominant creep mechanism is observed in air. Grain growth and densification during the creep tests can be ruled out, which indicates that the observed deformation represents solely the creep behavior. After the creep tests in both atmospheres, gaping grain boundaries were observed near the surfaces, while decomposition was only observed for the specimen that was tested in air. The oxygen partial pressure is responsible for the observed decomposition rather than the temperature, which is important for the technical application, since as a material candidate for H_2 permeation, BCZ20Y15 will not be exposed to oxygen under realistic working conditions.

The observed creep rate of BCZ20Y15 in 4% H_2/Ar at 850 °C is somewhat higher than the suggested critical compressive creep rate for commercial use of the membrane materials (1% per year). However, since the application temperature (~ 600 – 800 °C) is lower than the test temperature, a rough extrapolation of the creep rate of BCZ20Y15 to the application temperature can be made, which results in a creep rate close to the envisaged 1% per year. Therefore, for the design of reliable membrane components, the thermomechanical stability and in particular the creep behavior need to be considered.

References

[1] K. Katahira, Y. Kohchi, T. Shimura, H. Iwahara, Protonic conduction in Zr-substituted $BaCeO_3$, Solid State Ionics 138(1-2) (2000) 91-98.

[2] X. Ma, J. Dai, H. Zhang, D.E. Reisner, Protonic conductivity nanostructured ceramic film with improved resistance to carbon dioxide at elevated temperatures, Surface and Coatings Technology 200(5-6) (2005) 1252-1258.

[3] P. Sawant, S. Varma, B. Wani, S. Bharadwaj, Synthesis, stability and conductivity of $BaCe_{0.8-x}Zr_xY_{0.2}O_{3-\delta}$ as electrolyte for proton conducting SOFC, international journal of hydrogen energy 37(4) (2012) 3848-3856.

[4] M. Yano, A. Tomita, M. Sano, T. Hibino, Recent advances in single-chamber solid oxide fuel cells: a review, Solid State Ionics 177(39-40) (2007) 3351-3359.

[5] N. Radenahmad, A. Afif, P.I. Petra, S.M. Rahman, S.-G. Eriksson, A.K. Azad, Proton-conducting electrolytes for direct methanol and direct urea fuel cells–A state-of-the-art review, Renewable and Sustainable Energy Reviews 57 (2016) 1347-1358.

[6] K. Kreuer, Proton-conducting oxides, Annual Review of Materials Research 33(1) (2003) 333-359.

[7] J. Phair, S. Badwal, Review of proton conductors for hydrogen separation, Ionics 12(2) (2006) 103-115.

[8] S. Barison, M. Battagliarin, T. Cavallin, S. Daolio, L. Doubova, M. Fabrizio, C. Mortalo, S. Boldrini, R. Gerbasi, Barium Non-Stoichiometry Role on the Properties of $Ba_{1+x}Ce_{0.65}Zr_{0.20}Y_{0.15}O_{3-\delta}$ Proton Conductors for IT-SOFCs, Fuel cells 8(5) (2008) 360-368.

[9] J. Li, J.-L. Luo, K.T. Chuang, A.R. Sanger, Chemical stability of Y-doped Ba (Ce, Zr) O_3 perovskites in H_2S-containing H_2, Electrochimica Acta 53(10) (2008) 3701-3707.

[10] J. Lv, L. Wang, D. Lei, H. Guo, R. Kumar, Sintering, chemical stability and electrical conductivity of the perovskite proton conductors $BaCe_{0.45}Zr_{0.45}M_{0.1}O_{3-\delta}$ (M= In, Y, Gd, Sm), Journal of alloys and compounds 467(1-2) (2009) 376-382.

[11] Y. Yoo, N. Lim, Performance and stability of proton conducting solid oxide fuel cells based on yttrium-doped barium cerate-zirconate thin-film electrolyte, Journal of Power Sources 229 (2013) 48-57.

[12] Z. Zhong, Stability and conductivity study of the $BaCe_{0.9-x}Zr_xY_{0.1}O_{2.95}$ systems, Solid State Ionics 178(3-4) (2007) 213-220.

[13] C. Mortalò, E. Rebollo, S. Escolástico, S. Deambrosis, K. Haas-Santo, M. Rancan, R. Dittmeyer, L. Armelao, M. Fabrizio, Enhanced sulfur tolerance of $BaCe_{0.65}Zr_{0.20}Y_{0.15}O_{3-\delta}$-$Ce_{0.}$

$_{85}Gd_{0.15}O_{2-\delta}$ composite for hydrogen separation membranes, Journal of Membrane Science 564 (2018) 123-132.

[14] E. Rebollo, C. Mortalo, S. Escolástico, S. Boldrini, S. Barison, J.M. Serra, M. Fabrizio, Exceptional hydrogen permeation of all-ceramic composite robust membranes based on $BaCe_{0.65}Zr_{0.20}Y_{0.15}O_{3-\delta}$ and Y-or Gd-doped ceria, Energy & Environmental Science 8(12) (2015) 3675-3686.

[15] S. Barison, M. Battagliarin, T. Cavallin, L. Doubova, M. Fabrizio, C. Mortalo, S. Boldrini, L. Malavasi, R. Gerbasi, High conductivity and chemical stability of $BaCe_{1-x-y}Zr_{x}Y_{y}O_{3-\delta}$ proton conductors prepared by a sol–gel method, Journal of Materials Chemistry 18(42) (2008) 5120-5128.

[16] L. Doubova, S. Barison, S. Boldrini, M. Fabrizio, C. Mortalo, C. Pagura, Conductivity studies of sol-gel prepared $BaCe_{0.85-x}Zr_{x}Y_{0.15}O_{3-\delta}$ solid electrolytes using impedance spectroscopy, Journal of applied electrochemistry 39(11) (2009) 2129-2141.

[17] W. Deibert, M.E. Ivanova, S. Baumann, O. Guillon, W.A. Meulenberg, Ion-conducting ceramic membrane reactors for high-temperature applications, Journal of membrane science 543 (2017) 79-97.

[18] W.A. Meulenberg, F. Schulze-Küppers, W. Deibert, T.V. Gestel, S. Baumann, Ceramic Membranes: Materials–Components–Potential Applications, ChemBioEng Reviews 6(6) (2019) 198-208.

[19] J. Pelleg, Creep in ceramics, Creep in Ceramics, Springer2017, pp. 41-61.

[20] J. Yi, H. Lein, T. Grande, S. Yakovlev, H. Bouwmeester, High-temperature compressive creep behaviour of the perovskite-type oxide $Ba_{0.5}Sr_{0.5}Co_{0.8}Fe_{0.2}O_{3-\delta}$, Solid State Ionics 180(36-39) (2009) 1564-1568.

[21] M. Radovic, M. Barsoum, T. El-Raghy, S. Wiederhorn, Tensile creep of fine grained (3–5 μm) Ti_3SiC_2 in the 1000–1200° C temperature range, Acta materialia 49(19) (2001) 4103-4112.

[22] S. Ten Donkelaar, V. Stournari, J. Malzbender, A. Nijmeijer, H.J. Bouwmeester, High-temperature compressive creep behaviour of perovskite-type oxides $SrTi_{1-x}Fe_{x}O_{3-\delta}$, Journal of the European Ceramic Society 35(15) (2015) 4203-4209.

[23] J. Wei, J. Malzbender, Steady state creep of Ni-8YSZ substrates for application in solid oxide fuel and electrolysis cells, Journal of Power Sources 360 (2017) 1-10.

[24] Y. Zou, F. Schulze-Küppers, M. Balaguer, J. Malzbender, M. Krüger, Creep behavior of porous $La_{0.6}Sr_{0.4}Co_{0.2}Fe_{0.8}O_{3-\delta}$ substrate material for oxygen separation application, Journal of the European Ceramic Society 38(4) (2018) 1702-1710.

[25] W. Zhou, J. Malzbender, F. Zeng, W. Deibert, O. Guillon, R. Schwaiger, W.A. Meulenberg, Mechanical properties of $BaCe_{0.65}Zr_{0.2}Y_{0.15}O_{3-\delta}$ proton-conducting material determined using different nanoindentation methods, Journal of the European Ceramic Society 40(15) (2020) 5653-5661.

[26] C.A. Schneider, W.S. Rasband, K.W. Eliceiri, NIH Image to ImageJ: 25 years of image analysis, Nature methods 9(7) (2012) 671-675.

[27] X. Li, J. Gonzalez-Julian, J. Malzbender, Fabrication and mechanical performance of Ti_2AlN prepared by FAST/SPS, Journal of the European Ceramic Society (2020).

[28] W. Deibert, V. Stournari, M.E. Ivanova, S. Escolástico, J.M. Serra, J. Malzbender, T. Beck, L. Singheiser, O. Guillon, W.A. Meulenberg, Effect of microstructure on electrical and mechanical properties of $La_{5.4}WO_{12-\delta}$ proton conductor, Journal of the European Ceramic Society 38(10) (2018) 3527-3538.

[29] Y. Zou, F. Schulze-Küppers, J. Malzbender, Creep behavior of porous $La_{0.6}Sr_{0.4}Co_{0.2}Fe_{0.8}O_{3-\delta}$ oxygen transport membrane supports, Ceramics International 41(3) (2015) 4064-4069.

[30] B. Rutkowski, J. Malzbender, T. Beck, R. Steinbrech, L. Singheiser, Creep behaviour of tubular $Ba_{0.5}Sr_{0.5}Co_{0.8}Fe_{0.2}O_{3-\delta}$ gas separation membranes, Journal of the European Ceramic Society 31(4) (2011) 493-499.

[31] M. Schulz, R. Kriegel, W. Burckhardt, Modeling of oxygen flux and stress distribution for $Ba_{0.5}Sr_{0.5}Co_{0.8}Fe_{0.2}O_{3-\delta}$ membranes at application conditions, Intern. Conf. Inorg. Membranes, Japan, 2008.

[32] W. Araki, J. Gonzalez-Julian, J. Malzbender, High temperature compressive creep of dense and porous Cr_2AlC in air, Journal of the European Ceramic Society 39(13) (2019) 3660-3667.

[33] M. Radovic, M. Barsoum, T. El-Raghy, S. Wiederhorn, Tensile creep of coarse-grained Ti_3SiC_2 in the 1000–1200° C temperature range, Journal of Alloys and compounds 361(1-2) (2003) 299-312.

[34] https://phaseonline.ceramics.org/ped_figure_search PED Fig. No. 5134 (the database was accessed on 10.12.2019).

[35] https://phaseonline.ceramics.org/ped_figure_search PED Fig. No. 14154 (the database was accessed on 10.12.2019).

[36] D.J. Green, An introduction to the mechanical properties of ceramics, Cambridge university press1998.

[37] M.E. Kassner, Fundamentals of creep in metals and alloys, Butterworth-Heinemann2015.

[38] B. Huang, R. Steinbrech, S. Baumann, J. Malzbender, Creep behavior and its correlation with defect chemistry of $La_{0.58}Sr_{0.4}Co_{0.2}Fe_{0.8}O_{3-\delta}$, Acta materialia 60(6-7) (2012) 2479-2484.

[39] K. Goretta, E. Park, J. Guan, U. Balachandran, S. Dorris, J. Routbort, Diffusional creep of $BaCe_{0.8}Y_{0.2}O_{3-\alpha}$ mixed conductors, Solid State Ionics 111(3-4) (1998) 295-299.

[40] R. Rice, Evaluation and extension of physical property-porosity models based on minimum solid area, Journal of materials science 31(1) (1996) 102-118.

[41] R.W. Rice, Porosity of ceramics: properties and applications, CRC Press1998.

CHAPTER 5

Mechanical properties of $BaCe_{0.65}Zr_{0.2}Y_{0.15}O_{3-\delta}$-$Ce_{0.85}Gd_{0.15}O_{2-\delta}$ dual-phase proton-conducting material with emphasis on micro-pillar splitting

Abstract

$BaCe_{0.65}Zr_{0.2}Y_{0.15}O_{3-\delta}$-$Ce_{0.85}Gd_{0.15}O_{2-\delta}$ (BCZ20Y15-GDC15) dual-phase material revealed potential for H_2 production technologies due to its exceptional H_2 permeation and chemical resistance. In this article, mechanical properties of BCZ20Y15-GDC15 dual-phase material were investigated to evaluate the mechanical behavior and develop strategies to warrant structural stability. Elastic modulus, hardness and fracture toughness values were studied using different indentation-based methods. The fracture experiments at different length-scales both revealed that the introduction of GDC15 makes the material significantly tougher, facilitating the further design of robust and reliable components.

This chapter has been published as: W. Zhou, J. Malzbender, F. Zeng, W. Deibert, L. Winnubst, A. Nijmeijer, O. Guillon, R. Schwaiger, W.A. Meulenberg, Mechanical properties of $BaCe_{0.65}Zr_{0.2}Y_{0.15}O_{3-\delta}$–$Ce_{0.85}Gd_{0.15}O_{2-\delta}$ dual-phase proton-conducting material with emphasis on micro-pillar splitting, Journal of the European Ceramic Society 42(9) (2022) 3948-3956.

DOI: 10.1016/j.jeurceramsoc.2022.03.020.

5.1 Introduction

$BaCeO_3$-based protonic conductor materials [1-6] revealed the highest reported proton conductivities, in particular when doped with 15% Y [7, 8]. Furthermore, doping levels exceeding 20% Zr enhance the chemical stability against CO_2, H_2O and H_2S [9-13]. However, the poor electronic conductivity of BCZ20Y15 limits the ambipolar conductivity, thus reducing or even precluding the H_2 permeation across the membrane [13-15]. Although further doping with metals of variable oxidation states on the B-site of the ABO_3 perovskite (BCZ20Y15) could be a strategy to enhance the electronic conductivity but this could be detrimental to the protonic transport depending on the dopant [16]. The introduction of an electronic conducting secondary phase forming a dual-phase composite [17] represents another promising option. In this context, ceramic-metal (cer-met) composite membranes have been successfully investigated [18-23]. All-ceramic (ceramic-ceramic) systems have already demonstrated significant advantages regarding mechanical and chemical stabilities [24-31].

Studies on all-ceramic $BaCe_{0.65}Zr_{0.2}Y_{0.15}O_{3-\delta} – Ce_{0.85}Gd_{0.15}O_{2-\delta}$ (BCZ20Y15-GDC15) have revealed its exceptional hydrogen permeation [17], enhanced sulfur tolerance [32], good chemical stability in moist CO_2 environments [17, 32] and structural stability [33, 34] and indicate its potential for the technological application.

Despite the progress with respect to conductivity and chemical stability, only few studies have focused on the mechanical properties of all-ceramic dual phase gas transport membranes [35-41]. To the best of our knowledge, no systematic investigation was conducted to understand the mechanical properties of BCZ20Y15-GDC15.

Elastic modulus and hardness can be determined using indentation testing [42-44], while the validity of conventional indentation testing-based fracture toughness investigations is still under discussion [45]. Recently, Sebastiani et al. [46-49] developed fracture toughness assessment based on a micro-pillar indentation splitting test based on sharp indentations into micro-pillars prepared via focused ion beam (FIB) milling. The pillar splitting method was developed with the aim of characterizing microscale intrinsic fracture toughness on the basis of critical load values visible as kink effects [47] in the load-depth curves acquired during the pillar indentation process. Compared to the conventional Vickers-indentation-based fracture toughness test method (VIF) and other currently available microscale mechanical testing methods, e.g., single and double cantilever testing [46], the micro-pillar test method offers several advantages, including its ease of application. Post-test measurement of the crack length, a factor that is critical for the VIF method and highly dependent on the imaging characteristics, is not necessary for the micro-pillar test method [47, 50]. Furthermore, potential residual stress, which might be induced by stoichiometric gradients or differences in thermal expansion in the case of a thin film on a substrate, is fully released and does not affect the test if the pillars have an aspect ratio of height to diameter between 1 and 4 [51]. Difficulties related to friction coefficient calibration and possible Ga^+ ion implantation at the root of the stress-concentrating notch, which complicate the analysis of microcantilever fracture experiments, can be avoided [46, 47]. However, also in the case of pillar-splitting, size effects were observed, which were related to the FIB-preparation [51, 52]. While it is not necessary to determine the crack length, the validity of every splitting experiment needs to be confirmed since inaccuracies in the indenter tip positioning can result in an underestimation of the fracture toughness [51].

In this work, the mechanical properties of dual-phase BCZ20Y15-GDC15 were investigated. The study involved indentation testing at different length scales, yielding elastic modulus and hardness values. Furthermore, micro-pillar splitting tests were performed. A detailed microstructural analysis revealed the mechanism responsible for the toughening effect of GDC15.

5.2 Experimental

BCZ20Y15-GDC15 samples were prepared by a solid state reaction method (SSR). $BaCO_3$ (99%, Sigma Aldrich), CeO_2 (99.9%, Sigma Aldrich), ZrO_2 (99%, Sigma Aldrich), Y_2O_3 (99%, Sigma Aldrich), and Gd_2O_3 (99%, Sigma Aldrich) were used as starting materials. In the process, BCZ20Y15 and GDC15 were prepared separately. Precursor powders were mixed according to the stoichiometry and ball-milled (Rollermill RM1, Zoz GmbH, Wenden, Germany. ZrO_2 balls, 3.5 mm diameter, weight ratio powder : balls : ethanol = 1 : 2 : 3) in ethanol for 24 h. The resultant mixtures were dried at 80 °C for two to three days. Then, the BCZ20Y15 mixtures were calcined at 1300 °C for 5 h, and the GDC15 mixtures at 1200 °C for 12 h [52, 53]. Afterwards, the two compositions were mixed (shaker mixer TURBULA T2, Willy A. Bachofen GmbH, Nidderau, Germany) in a 50 : 50 volume ratio, with additional 0.5 wt. % (of BCZ20Y15 weight) NiO (99%, Sigma Aldrich) [17] as sintering aid in order to obtain dense samples. In order to obtain powders with a fine and homogeneous grain size, pre-calcined mixture powders were ball-milled in ethanol for 24 h. Finally, the powder mixtures were dried and sieved through a 160 μm mesh.

Bulk membranes were uniaxially pressed into a disc shape under a pressure of ~ 20 MPa for 5 minutes to obtain green samples with diameter and thickness of ~ 27 mm and ~ 1 mm, respectively. The samples were subsequently sintered at 1500 °C for 5 hours in air using a constant heating / cooling rate of 5 $K \cdot min^{-1}$.

The crystal structure and phase purity of the sintered samples was characterized using an EMPYREAN (PANalytical) diffractometer with parafocusing Bragg-Brentano geometry, employing a Cu-LFF-tube (40 kV / 40 mA), a BBHD mirror (Bragg-BrentanoHD mirror, manufactured by Malvern Panalytical, Ltd., Malvern, UK), 0.04 rad Soller slits, and a PIXcel3D detector. X-ray diffraction (XRD) patterns were recorded at room temperature using a step scan procedure (0.4 s per step, 0.013 ° per step size) in the 2θ range of 5 – 90 °.

The microstructures and topographies of the samples were assessed by a Zeiss SUPRA 50VP field emission scanning electron microscope (SEM, Zeiss Microscopy GmbH, Oberkochen, Germany). The respective specimen was first embedded in epoxy resin, ground sequentially using SiO_2 sandpaper with 400 and 2000 grit size and then polished using 6 µm and 1 µm diamond suspension. The final polishing was conducted using 50 nm colloidal silica polishing suspension. The image analysis software Image J [54] was used to determine the grain size and porosity from the electron backscatter diffraction (EBSD, HKL Nordlys model, Oxford Instruments, High Wycombe, UK.) phase mapping. Energy dispersive X-ray (EDX) spectroscopy was carried out at 10 kV accelerating voltage using a X-Max 80 detector and the AZtec data acquisition and analysis software package (Oxford Instruments Nanoanalysis, High Wycombe, United Kingdom).

Depth-sensing indentation testing was carried out using an indentation system (MicroMaterials, Ltd., Wrexham, UK), equipped with a diamond Berkovich tip. Elastic modulus and hardness were determined from the load-depth curves under load control following the procedure developed by Oliver and Pharr [55, 56]. The reduced modulus (E_r) was calculated using:

$$E_r = \frac{\sqrt{\pi} \cdot S}{2 \cdot \beta \cdot \sqrt{A_p(h_c)}} \tag{5.1}$$

where S is the contact stiffness determined from the unloading slope, β a tip-dependent geometry factor assumed as 1.034 , A_p the projected contact area, and h_c the contact depth at the maximum load P_{max}. The plane strain modulus (E^*) then corresponds to:

$$E^* = \frac{1}{\frac{1}{E_r} - \frac{1 - v_i^2}{E_i}} \tag{5.2}$$

where E_i is the elastic modulus and v_i Poisson's ratio of the diamond indenter tip assuming 1141 GPa and 0.07, respectively. Young's modulus E_{IT} was then calculated from E^* using a Poisson's ratio of the sample of $v_s = 0.3$, which is typical of ceramics [57]:

$$E_{IT} = E^{*} \cdot (1 - \nu_s^2) \tag{5.3}$$

The hardness H_{IT} was determined from the maximum load and the corresponding contact area:

$$H_{IT} = \frac{P_{max}}{A_p} \tag{5.4}$$

The indentation experiments were conducted to different maximum loads of 20, 200 mN, 1 N and 2 N. Thirty indents at each load were performed at a loading rate of 2 mN/s. The distances between indents were 15 µm and 90 µm at 20 mN and 200 mN, respectively. For higher loads of 1 N and 2 N, the distances between indents were 150 µm and 210 µm, respectively.

The fracture toughness evaluated using the conventional Vickers-indentation-based fracture toughness method [58] at applied loads of 3 N, 5 N and 10 N. Crack length induced by the Vickers indentation was measured immediately after the test to avoid subcritical crack growth effects [59]. The following empirical equation, which was developed for the half-penny crack mode, was used to calculate the apparent fracture toughness K_{IC} [60, 61]:

$$K_{IC} = 0.016 \left(\frac{E}{H}\right)^{\frac{1}{2}} \left(\frac{P}{c^{3/2}}\right) \tag{5.5}$$

where c is the crack length determined from micrographs, E and H derived from indentation were used.

For the micropillar-based fracture toughness characterization, 8 pillars with nominal diameters of 15 µm were FIB-milled using an Auriga Crossbeam workstation (Zeiss Microscopy GmbH, Oberkochen, Germany) operated at 30 kV and 4 nA. Table 5.1 summarizes the actual (real) pillar diameters, which were used for the subsequent evaluation of the fracture toughness values.

Table 5.1 Nominal and actual pillar diameters.

	Pillar No./Real diameter [μm]							
Nominal diameter [μm]	P1	P2	P3	P4	P5	P6	P7	P8
15	15.9	16.2	16.7	15.1	14.9	16.1	15.9	15.4

The load was applied at a loading rating of 2.5 mN/s and kinks indicate the pillar splitting. The fracture toughness values were then calculated from the kink loads using the following equation [47]:

$$K_{IC} = \gamma \cdot \frac{P_c}{R^{3/2}} \tag{5.6}$$

where P_c is the critical load at kink, γ is a dimensionless coefficient that includes the influence of elastic-plastic properties and R is the radius of the pillar. The coefficient γ (Equation 5.6) was initially calculated by means of the finite element method [47], while in later works a linear relationship between γ and E / H was derived, which holds as long as $7 \leq E / H \leq 21$ [62, 63]:

$$\gamma = 0.0149\frac{E}{H} + 0.057 \tag{5.7}$$

Using this equation along with the experimentally determined indentation elastic modulus and hardness, γ thus a value of ~ 0.33.

5.3 Results and discussion

5.3.1 Phase and microstructure characterizations

The dual-phase material's crystal structure was verified by XRD (see Figure 5.1).

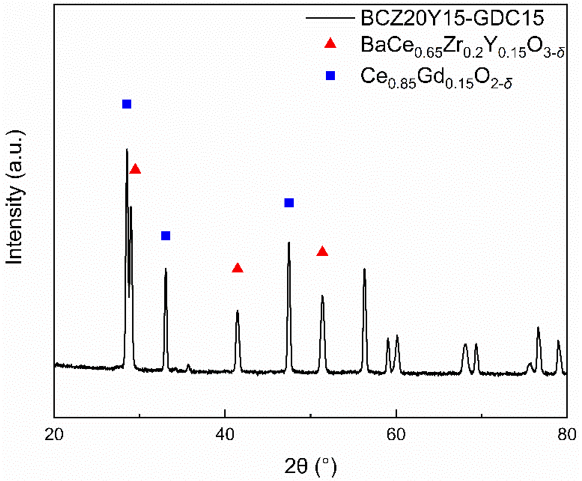

Figure 5.1 XRD pattern of BCZ20Y15-GDC15, identified according to ICSD 90052 and ICSD 28795. The three strongest peaks corresponding to BCZ20Y15 and GDC15 are marked by the red triangles and the blue squares, respectively. There is no indication of the presence of a 3rd phase.

No third phase was observed in the XRD results, indicating that with 0.5 wt% NiO as sintering aid, after 1500 °C / 5 h sintering, the sample contained only BCZ20Y15 (identified according to ICSD 90052) and GDC15 (identified according to ICSD 28795). From the XRD pattern, no peaks corresponding to NiO can be observed, due to the very low amount of NiO, similar as reported in [52]. The detected room temperature orthorhombic and cubic crystal structures of BCZ20Y15 and GDC15 are in agreement with those reported in [17, 32, 33].

The dual-phase material's microstructure was characterized using SEM (see Figure 5.2).

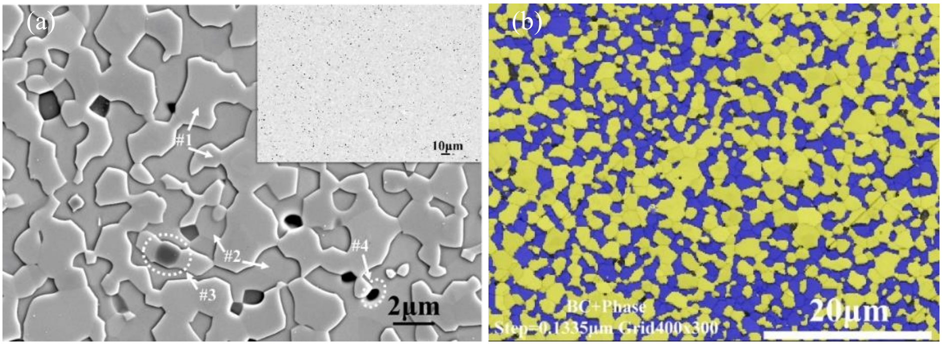

Figure 5.2 (a) SEM images of BCZ20Y15-GDC15. The black spots in the inset are pores, corresponding to less than 2% of the surface area. The topographically higher (#1) and lower phase (#2) are GDC15 and BCZ20Y15, respectively. Local Ni enrichment (#3) within GDC15 was observed (see Figure A5.1). Pores (#4) with typical round shape. (b) EBSD phase mapping combined with band contrast. The yellow areas correspond to GDC15, the blue to BCZ20Y15, with area ratios of ~ 60% and 40%, respectively.

The SEM micrographs indicate a porosity of less than 2% (using Image J [54]). The topographically (Figure 5.2 (a)) clearly elevated phase (Figure 5.2 (a) #1) and lowered phase (Figure 5.2 (a) #2) were observed, corresponding to GDC15 and BCZ20Y15, respectively, as confirmed by EDX and EBSD. Such variation of the topography in a dual-phase ceramic material was also reported in [35, 64], which was explained by large hardness differences of the individual phases.

Local Ni enrichment (Figure 5.2 (a) #3) was observed inside the GDC15 phase, similar as reported in [65], indicating that there is no reaction or solubility of Ni and GDC15 [65]. After ball-mixing, NiO exists in the mixture powder. During sintering a small amount of NiO was trapped inside the GDC15, thus not affecting the GDC15 phase sintering process. However, it could not be detected by XRD due to its limited quantity. The observed pores having a round shape (Figure 5.2 (a) #4) are similar to those reported in [36, 52, 66-68].

From the EBSD phase mapping combined with band contrast (Figure 5.2 (b)), the distribution of two individual phases can be observed. Their actual area ratio

(GDC15 - yellow : BCZ20Y15 - blue) is ~ 60:40 Vol. %. For the sake of clarity, in the further discussion, the materials will be termed with the nominal phase ratio. Individual phases' connection, which is extremely important in dual-phase ceramics and has been discussed in detail in [69-71], appears to have been achieved for both phases. The EBSD analysis also yielded the grain sizes, being for both BCZ20Y15 and GDC15 ~ 1 µm. Considering the authors' previous work on single phase BCZ20Y15 [52], whose grain size is ~ 13 µm, it seems that GDC15 limits the grain growth of BCZ20Y15.

5.3.2 Mechanical properties

The elastic modulus and hardness values of BCZ20Y15-GDC15 are summarized in Table 5.2.

Table 5.2 Elastic modulus and hardness of BCZ20Y15-GDC15.

Load [mN]	20	200	1000	2000
Elastic modulus [GPa]	166 ± 17	163 ± 9	168 ± 10	164 ± 10
Hardness [GPa]	8.5 ± 1.1	9.3 ± 0.7	7.8 ± 0.4	7.2 ± 0.4

Both elastic modulus and hardness determined from the indentation tests are independent of the applied loads, as shown in the Table 5.2. At loads of 20 and 200 mN, the elastic modulus and the hardness are higher than those determined for single phase BCZ20Y15 (~ 120 GPa and ~ 7 GPa) [52], at the same applied loads. This indicates that after introduction of GDC15 into the material, forming the dual-phase BCZ20Y15-GDC15, both the apparent elastic and plastic properties are enhanced. Since the elastic modulus and hardness of GDC are ~ 230 GPa and ~ 14 GPa, respectively [36, 40], which are significantly higher than the values of single phase BCZ20Y15 [52], it is reasonable to assume that the mechanical response to indentation testing of the material is enhanced when a phase with higher elastic modulus and hardness exists in the composite [40, 72].

Different from the elastic modulus, the noticeably decreases when the load is increased from 200 mN to 1 N, and remains approximately constant with increasing loads. When the applied load is ≥ 1 N, the results apparently reflect the global properties of material and the hardness decrease may result from the formation of radial/median cracks at higher loads [60].

The diameter of the micro-pillar was ~ 15 µm, which is distinctly larger than the grain size. Therefore, the micro-pillar splitting test can be used to investigate the material global mechanical properties, as reported in [73-75]. Representative load-depth curves of the BCZ20Y15-GDC15 micro-pillar splitting tests, together with the load-depth curve of indentation test on BCZ20Y15-GDC15 into the bulk region as reference are presented in Figure 5.3. Furthermore, a representative load-depth curve of a single-phase BCZ20Y15 micro-pillar splitting test [52] has been added into Figure 5.3.

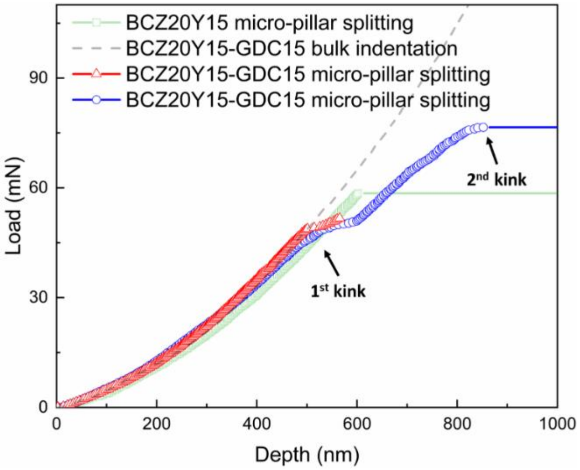

Figure 5.3 Representative load-depth curves obtained from the BCZ20Y15-GDC15 micro-pillar splitting tests (red and blue lines), together with the representative indentation load-depth curve on BCZ20Y15-GDC15, as reference (gray dashed line). A representative load-depth curve of a single-phase BCZ20Y15 micro-pillar (15 µm pillar size) splitting tests [52] is shown by the green symbols.

The good agreement between the dual-phase pillar splitting curves and the indent curve, obtained on the sample bulk region, confirms the validity of the results [52, 59, 62].

Obviously, two kinks are observed during the dual-phase micro-pillar splitting tests. This phenomenon has never been reported in single-phase micro-pillar splitting investigations [46, 47, 51, 52, 59, 62, 63], in which only one kink was observed, corresponding to the critical load for crack initiation [46, 47].

To clarify the origin of the two kinks, a post-test SEM characterization was performed (Figure 5.4).

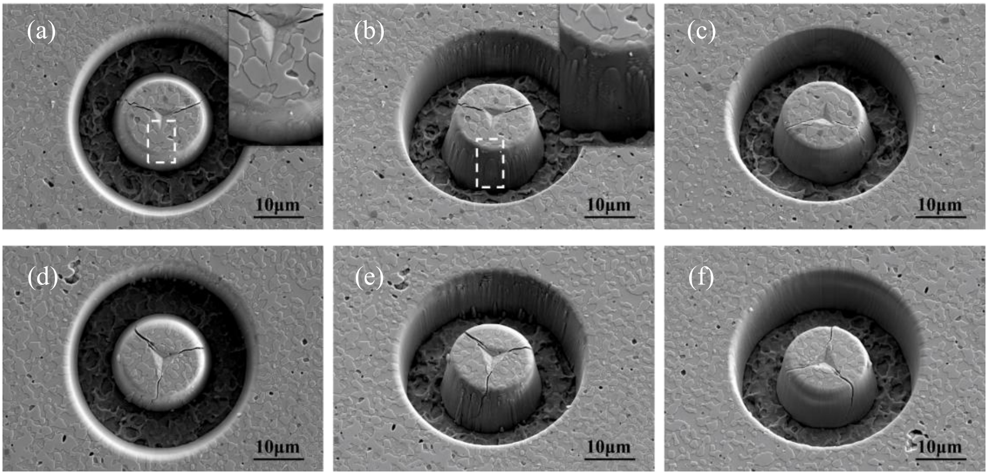

Figure 5.4 SEM investigation of pillars after splitting experiments: (a) Top view, (b) side view (sample tilt 26°) and (c) side view (at 180° rotation) of a pillar exhibiting only one kink in the curve. The inset in (a) shows a very thin "3rd crack", that can't be seen in the inset in (b). The other two cracks (c) reach the pillar bottom. (d) Top view, (e) side view (sample tilt 26°) and (f) side view (at 180° rotation) of a pillar with two kinks.

The indentation locations are all within pillar center 10% region, which ensures test validity and reliability of the derived K_{IC} [51]. In the top view image (Figure 5.4 (a)) showing the pillar test that was terminated after the first kink (Figure 5.3), only two cracks can be clearly observed. The expected 3rd crack is faintly visible in the magnified inset, but appears to be very narrow compared to the other cracks. Such a phenomenon was neither observed in our previous work [52] on single-phase BCZ20Y15, nor reported in other micro-pillar splitting investigations on single-phase materials [51, 59, 63, 76-80]. Potential reason for this effect can be the large difference of the mechanical properties of GDC15 and BCZ20Y15 [36, 40, 52], in particular the higher fracture toughness of GDC15. An observation of the side surface (Figure 5.4 (b)) reveals no trace of the 3rd crack, whereas the other two cracks (Figure 5.4 (c)) could clearly be confirmed, indicating that the pillar did not split completely in this test.

After the occurrence of two kinks, the pillar (Figure 5.4 (d)) shows clearly the typical, expected 3-way-split [51]. Cracks propagate on the pillar side walls (Figure 5.4 (e, f)) directly down to the bottom of the pillar, similar as observed for single-phase BCZ20Y15 [52], indicating that the pillar entirely splits.

Based on the post-test observation, the “1st kink” corresponds to the pillar splitting partially, and the crack propagated mainly through BCZ20Y15 phase. The “2nd kink” corresponds to the pillar splitting completely, and during this splitting the crack proceeds through the tougher GDC15 phase. According to the classical theory developed by Lawn et al. [81], regarding the initial crack nucleation, and the FEM analysis on crack geometries of pillar by Sebastiani et al. [47], a series of FIB cuts on the selected pillars was performed to gain further insight on microstructural effects (Figure 5.5).

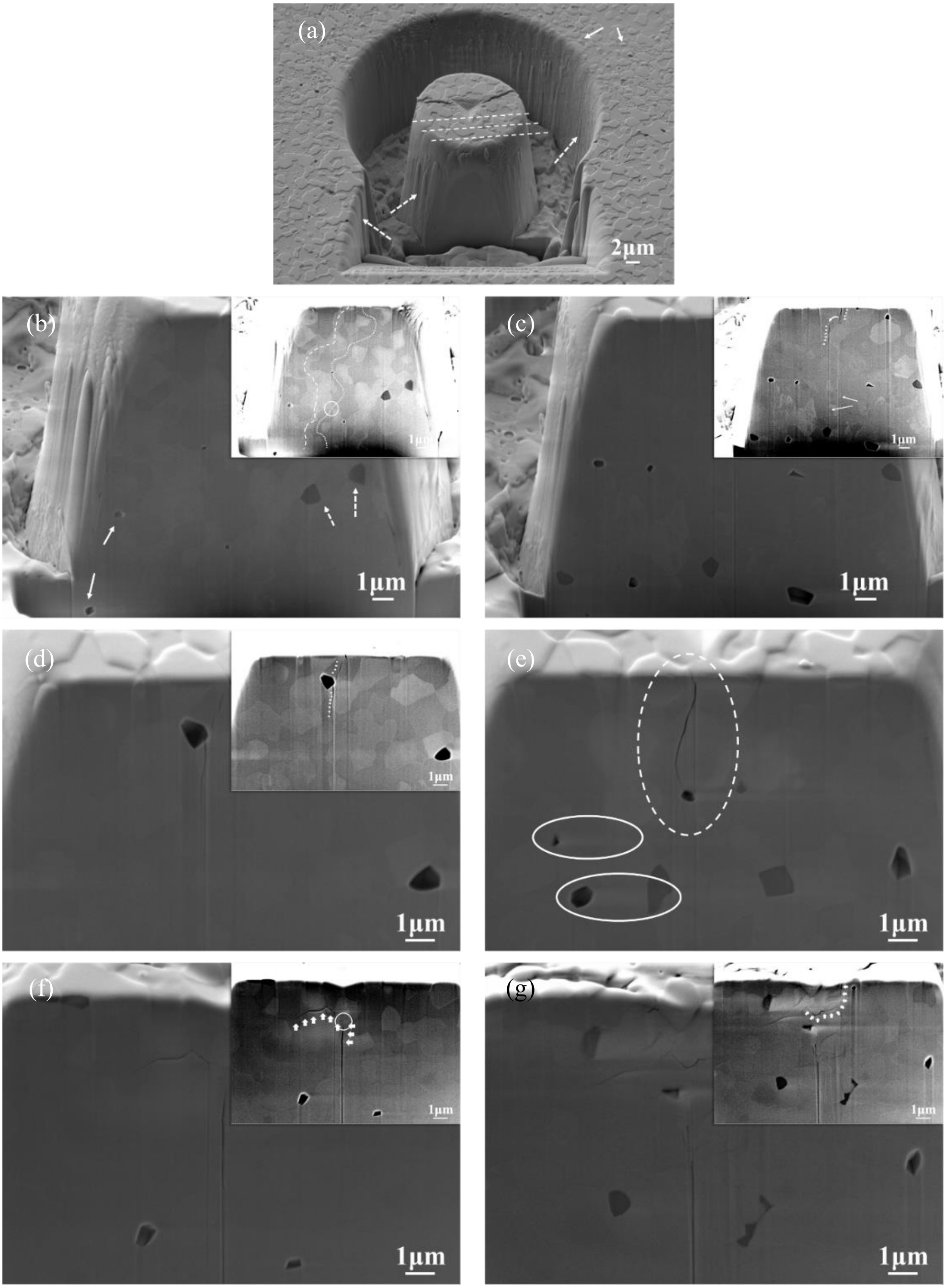

Figure 5.5 Slice-by-slice FIB milling of pillar with one kink. (a) A window was milled. The solid arrows mark blister-like morphologies. The curtain artifacts is marked by dashed arrows.

Further FIB milling follow the dashed lines. (b) The solid arrows indicate pores, and the dashed arrows mark Ni exsolution. The dashed and the dotted line mark the individual phases' connections. The circle marked region in the line demonstrates a narrow path. (c) The long arrows mark the FIB curtaining artifact. The short arrows and the curved arrow mark the "crack jump". (d) Crack deflection. (e) Crack deflection due to pores (dashed circle). Fuzzy bands, marked by the solid circles. (f) The median and radial cracks. (g) The plastic zone.

To perform the slice-by-slice FIB milling for further observation, as a first step, a window was cut (Figure 5.5 (a)), see also [52, 59, 80]. The solid arrows mark some blister-like morphologies, being surface contaminations induced by the Ga^+ implanted into the materials' surface region during FIB milling. A ~ 20 - 30 nm thickness amorphous layer has been reported in case of Si [51] and Ga^+ substitution in case of $Li_7La_3Zr_2O_{12}$ [82], potentially leading to local fracture toughness increase in particular when pillar sizes are less than 10 μm [51]. These effects will be discussed below regarding Figure A5.2.

In order to observe the 3rd crack inside the pillar, slice-by-slice FIB milling followed the dashed lines marked direction (Figure 5.5 (a)). It should be noted that there was no trace of a 3rd crack on the sidewall, as discussed with respect to Figure 5.4 (b).

The solid arrows in Figure 5.5 (b) show pores inside the pillar, and the dashed arrows indicate Ni exsolution, which has been discussed above (Figure 5.2 (a)). Although from the original SEM graphs different contrast can already be observed, an inset with adjusted brightness/contrast was added to highlight the sub-features, see also [52]. There is obviously a brighter phase and a darker phase. As already discussed above (Figure 5.2 (a)) the topographically higher phase corresponds to GDC15 and lower phase to BCZ20Y15, and hence it can be concluded that the brighter phase is GDC15 and the darker phase is BCZ20Y15.

The long arrows in Figure 5.5 (c) mark FIB curtaining artifacts, as discussed above (Figure 5.5 (a)). Crack propagation stopped in front of GDC15 and then it re-propagated in BCZ20Y15, as marked by the short arrows, indicating the existence of “crack jump” marked by the curved arrow, which can be a crack bridging effect [83] reducing the stress field, or another kind of crack deflection [84] in the 3rd dimension, which can’t be observed in this cross-section.

The short arrows in Figure 5.5 (d) highlight that the crack proceeds through the weaker phase (BCZ20Y15) [36, 40, 52], towards the weakest phase (pores) [85], and then deflect after encountering the pores, which is similar as reported in [86] and the crack deflection model, developed for porous ceramic interlayers, [87] can explain this behavior.

The 3rd crack indeed exists inside the pillar, as marked by the dashed circle in Figure 5.5 (e), but shallow and narrow, which is consistent with the crack geometry for a “just prior to instability load” [47], indicating that the pillar’s “3rd crack” side did not entirely split, which exactly confirms the above interpretation regarding Figure 5.4 (b). Besides, crack deflection due to pores was observed, similar as observed in [52]. Fuzzy bands, marked by solid circles, were observed as a result of long-time under FIB and SEM leading to charging and drift.

Median and radial cracks, marked by short arrows in Figure 5.5 (f), indicate a half-penny crack mode [60]. It should be noted that the marked region is indeed a median crack rather than FIB curtaining artifact, since it is deep and tilts rather than being shallow and straight down to the bottom, which can be distinguished in the original SEM graph. The initial crack nucleation, marked by the circle, is on the interface of plastic zone and elastic region, according to the classical theory developed by Lawn et al. [81].

The plastic zone, marked by the short arrows in Figure 5.5 (g), is not very typical, especially when compared with what observed in the case of single phase BCZ20Y15 [52], potentially due to the large differences of GDC15 and BCZ20Y15 mechanical properties [36, 40, 52]. Besides, pores and associated charging effects lead to fuzzy bands rendering microstructural observation difficult.

Similar to the “1st kink stop” pillar, a slice-by-slice FIB milling was also performed on the selected “2nd kink stop” pillar (Figure 5.6).

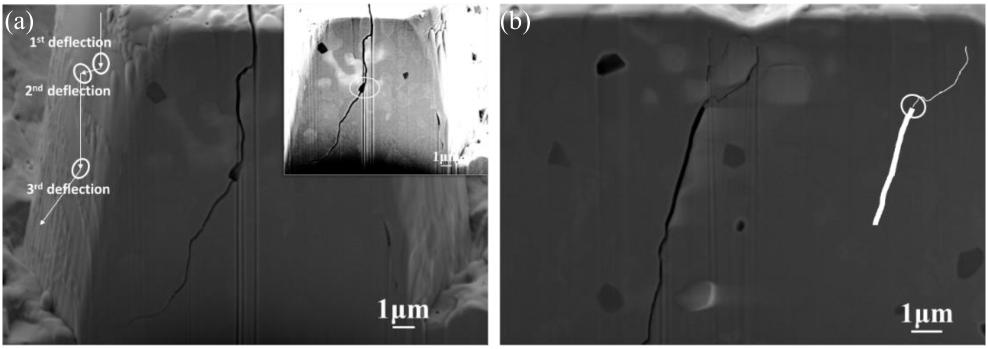

Figure 5.6 Slice-by-slice FIB milling of pillar with two kinks: (a) A series of crack deflections were observed. The inset at adjusted brightness/contrast shows the crack deflection. Pores, marked by the circle. (b) Thin cracks were observed inside the plastic zone, as illustrated in the sketch. The typical median crack (significantly wider). The circle marks the apparent initial crack nucleation position.

Similar as for the “1st kink stop” pillar (Figure 5.5), a slice-by-slice FIB milling was conducted on the selected “2nd kink stop” pillar (Figure 5.6). It’s clear that the 3rd crack exists on the sidewall, similar as in [52, 59], but being different from what is observed on the “1st kink stop” pillar (Figure 5.5 (a, b)), indicating that the “2nd kink stop” pillar indeed entirely split.

A series of three crack deflections were observed (Figure 5.6 (a)) and from the adjusted brightness/contrast inset, it’s clear that the crack deflected to avoid the GDC15 phase, due to the difference between GDC15 and BCZ20Y15 properties [36, 40, 52], similar as reported in [88], in which crack deflect or bifurcate to avoid the tougher layers. The pores, marked by the circle, apparently are responsible for the 3rd crack deflection, as also discussed above (Figure 5.5 (d)).

Due to the different crack growth resistance of GDC15 and BCZ20Y15 [36, 40, 52], some narrow cracks occurred in the plastic zone (Figure 5.6 (b)), as demonstrated by the sketch. Below that, a typical median crack can be seen, which is wider, similar as observed in [52]. An initial crack nucleation can be seen at their interconnection region, as marked by the circle, following Lawn's theory [81].

The above analysis on the selected "1st kink stop" pillar and "2nd kink stop" pillar verifies the former interpretation. After revealing what these two kinks represent, the microscale intrinsic fracture toughness can be derived based on Equation 5.6, resulting in the values shown in Figure 5.7.

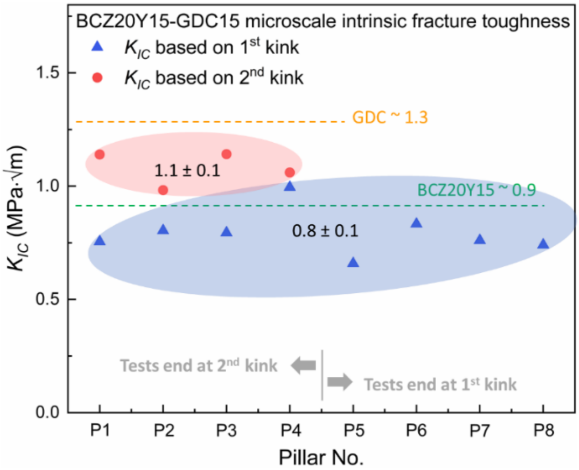

Figure 5.7 Microscale intrinsic fracture toughness of BCZ20Y15-GDC15 determined from pillar splitting. For Pillars P1 to P4, two kinks were observed, yielding ~ 1.1 MPa·√m evaluating the load at the 2nd kink (red circles). For pillars P5 to P8, the tests ended after the 1st kink, yielding ~ 0.8 MPa·√m (blue triangles). Reference lines for single-phase GDC10 and BCZ20Y15 are also added (~ 1.3 MPa·√m [40] and ~ 0.9 MPa·√m [52], respectively).

The pillars 1 to 4 showed curves with 2 kinks, pillars 5 to 8 only 1st kink (the grouping of the pillars with 2 kinks, i.e. 1 to 4, and the ones with 1 kink, i.e. 5 to 8, does not correspond to the order of the tests and was done after the test series to simplify the discussion). The derived 1st kink pillars lead to K_{IC} values of ~ 0.8 ± 0.1 MPa·√m, which agrees well with the single-phase BCZ20Y15 pillar splitting result [52], as marked by the green dashed line in Figure 5.7. This means that the 1st kink indeed corresponds with the pillar weaker side (BCZ20Y15) split, as already discussed in Figure 5.5. The derived 2nd kink corresponding K_{IC} is between the K_{IC} of single-phase BCZ20Y15 [52] and GDC10 [40], with a value of ~ 1.1 ± 0.1 MPa·√m, indicating that the 2nd kink represents a value for the whole pillar split, which is also shown in Figure 5.6.

Although the pillar size is ~ 15 μm, which is significantly larger than the suggested critical pillar size to avoid the Ga^+ ion implantation effects [51], post-test EDX analysis were also performed for verification (Figure A5.2).

The Ga^+ is mainly located (Figure A5.2 (e)) at the edge of the pillar, similar as reported in [52, 59], implying that the indentation position is sufficiently far away from the Ga^+ affected region, which guarantees the validity of the derived K_{IC} values in Figure 5.7.

A mesoscale apparent fracture toughness was also obtained via the VIF method (Figure 5.8).

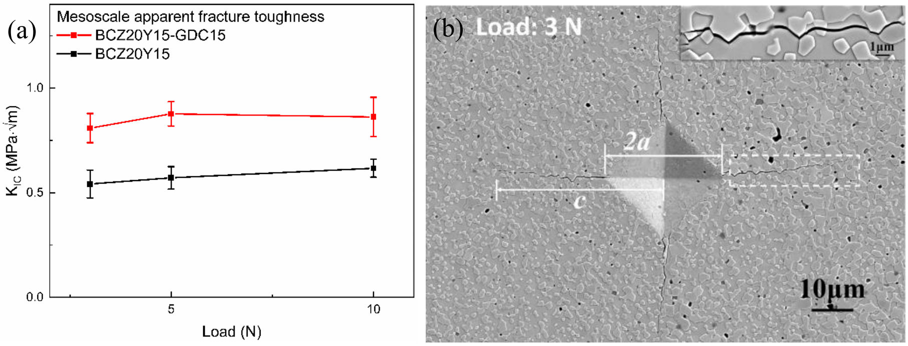

Figure 5.8 (a) Comparison of the Vickers indentation apparent fracture toughness values of BCZ20Y15-GDC15 and BCZ20Y15 [52]. (b) SEM observation on a 3 N Vickers imprint. The crack length *c* was used to determine the fracture toughness following the methodology outlined in [60]. The inset shows the marked region demonstrating the crack deflection to avoid GDC15.

The fracture toughness was determined from the micrographs of Vickers indentation test impressions (Figure 5.8 (b)). The ratio of c/a, where c is the length from the indentation center point to the end of the crack tip and a is half of the length of the indentation impression diagonal, was confirmed to be larger than 2.5 for all loads, which usually corresponds a half-penny crack mode [60]. For the loads of 3 N, 5 N and 10 N, the fracture toughness was determined to be ~ 0.9 ± 0.1 MPa·√m (see Figure 5.8 (a)), with only a negligible dependency on the applied load which is within the limits of experimental uncertainty. The mesoscale apparent fracture toughness values of BCZ20Y15-GDC15 and single-phase BCZ20Y15 [52] are presented in Figure 5.8 (a). The clear difference indicates that the introduction of GDC15 indeed makes the material tougher. The reason is clearly the crack deflection, confirmed in Figure 5.8 (b) inset and Figure A5.3, similar as observed in Figure 5.6 (b). Although the validity of VIF method specifically determined values is still under discussion [45], it can still be used to permit a comparison especially for similar types of materials and crack modes, i.e. both Figure 5.8 (a) and Figure 5.7 indicate that BCZ20Y15-GDC15 is tougher than BCZ20Y15, on a mesoscale and microscale, respectively.

5.4 Conclusions

The mechanical properties of dual-phase proton conducting ceramic BCZ20Y15-GDC15 were studied using different indentation-based methods on different length scales. The elastic modulus did not depend on the applied load and was determined as ~ 170 GPa. The hardness of BCZ20Y15-GDC15 decreases with increasing indentation depth, from ~ 9 GPa at loads lower than 200 mN to ~ 7 GPa at loads higher than 1 N, which might be due to the formation of radial/median cracks at higher loads.

The microscale intrinsic fracture toughness was determined by micropillar splitting. Slice-by-slice FIB milling of tested pillars and a detailed microstructural investigation confirmed that the 1st kink in the load-depth curve indicates the partial split of the pillar (at a lower load), while the 2nd kink corresponds the splitting of the whole pillar, as typically seen in such pillar splitting experiments. Thus, the fracture toughness of ~ 1.1 MPa·√m corresponding to 2nd kink, represents the dual-phase BCZ20Y15-GDC15 intrinsic fracture toughness. Significant toughening associated effects due to crack deflections to avoid GDC15 were observed.

The apparent fracture toughness was also estimated via the VIF method. While it represents only a rough estimate, it can still be used as a means for comparison, in particular when evaluating similar types of material. Both methods confirm that the introduction of GDC15 indeed significantly toughens the material, which can be a guide for further materials and component design.

References

[1] K. Katahira, Y. Kohchi, T. Shimura, H. Iwahara, Protonic conduction in Zr-substituted $BaCeO_3$, Solid State Ionics 138(1-2) (2000) 91-98.

[2] X. Ma, J. Dai, H. Zhang, D.E. Reisner, Protonic conductivity nanostructured ceramic film with improved resistance to carbon dioxide at elevated temperatures, Surface and Coatings Technology 200(5-6) (2005) 1252-1258.

[3] P. Sawant, S. Varma, B. Wani, S. Bharadwaj, Synthesis, stability and conductivity of $BaCe_{0.8-x}Zr_xY_{0.2}O_{3-\delta}$ as electrolyte for proton conducting SOFC, international journal of hydrogen energy 37(4) (2012) 3848-3856.

[4] M. Yano, A. Tomita, M. Sano, T. Hibino, Recent advances in single-chamber solid oxide fuel cells: a review, Solid State Ionics 177(39-40) (2007) 3351-3359.

[5] N. Radenahmad, A. Afif, P.I. Petra, S.M. Rahman, S.-G. Eriksson, A.K. Azad, Proton-conducting electrolytes for direct methanol and direct urea fuel cells–A state-of-the-art review, Renewable and Sustainable Energy Reviews 57 (2016) 1347-1358.

[6] J. Phair, S. Badwal, Review of proton conductors for hydrogen separation, Ionics 12(2) (2006) 103-115.

[7] K. Kreuer, Proton-conducting oxides, Annual Review of Materials Research 33(1) (2003) 333-359.

[8] G. Chiodelli, L. Malavasi, C. Tealdi, S. Barison, M. Battagliarin, L. Doubova, M. Fabrizio, C. Mortalo, R. Gerbasi, Role of synthetic route on the transport properties of $BaCe_{1-x}Y_xO_3$ proton conductor, Journal of Alloys and Compounds 470(1-2) (2009) 477-485.

[9] E. Fabbri, A. D'Epifanio, E. Di Bartolomeo, S. Licoccia, E. Traversa, Tailoring the chemical stability of $Ba(Ce_{0.8-x}Zr_x)Y_{0.2}O_{3-\delta}$ protonic conductors for intermediate temperature solid oxide fuel cells (IT-SOFCs), Solid State Ionics 179(15-16) (2008) 558-564.

[10] A. Magrez, T. Schober, Preparation, sintering, and water incorporation of proton conducting $Ba_{0.99}Zr_{0.8}Y_{0.2}O_{3-\delta}$: comparison between three different synthesis techniques, Solid State Ionics 175(1-4) (2004) 585-588.

[11] S. Tao, J.T. Irvine, Conductivity studies of dense yttrium-doped $BaZrO_3$ sintered at 1325 °C, Journal of Solid State Chemistry 180(12) (2007) 3493-3503.

[12] J. Li, J.-L. Luo, K.T. Chuang, A.R. Sanger, Chemical stability of Y-doped $Ba(Ce, Zr)O_3$ perovskites in H_2S-containing H_2, Electrochimica Acta 53(10) (2008) 3701-3707.

[13] K.H. Ryu, S.M. Haile, Chemical stability and proton conductivity of doped $BaCeO_3$–$BaZrO_3$ solid solutions, Solid State Ionics 125(1-4) (1999) 355-367.

[14] S. Barison, M. Battagliarin, T. Cavallin, L. Doubova, M. Fabrizio, C. Mortalo, S. Boldrini, L. Malavasi, R. Gerbasi, High conductivity and chemical stability of $BaCe_{1-x-y}Zr_x Y_yO_{3-\delta}$ proton conductors prepared by a sol–gel method, Journal of Materials Chemistry 18(42) (2008) 5120-5128.

[15] S. Barison, M. Battagliarin, T. Cavallin, S. Daolio, L. Doubova, M. Fabrizio, C. Mortalo, S. Boldrini, R. Gerbasi, Barium Non‐Stoichiometry Role on the Properties of $Ba_{1+x}Ce_{0.65}Zr_{0.20}Y_{0.15}O_{3-\delta}$ Proton Conductors for IT‐SOFCs, Fuel cells 8(5) (2008) 360-368.

[16] T. Norby, R. Haugsrud, Dense ceramic membranes for hydrogen separation, Wiley-VCH Verlag: Weinheim2006.

[17] E. Rebollo, C. Mortalo, S. Escolástico, S. Boldrini, S. Barison, J.M. Serra, M. Fabrizio, Exceptional hydrogen permeation of all-ceramic composite robust membranes based on $BaCe_{0.65}Zr_{0.20}Y_{0.15}O_{3-\delta}$ and Y-or Gd-doped ceria, Energy & Environmental Science 8(12) (2015) 3675-3686.

[18] H. Kim, B. Kim, J. Lee, K. Ahn, H.-R. Kim, K.J. Yoon, B.-K. Kim, Y.W. Cho, H.-W. Lee, J.-H. Lee, Microstructural adjustment of Ni–$BaCe_{0.9}Y_{0.1}O_{3-\delta}$ cermet membrane for improved hydrogen permeation, Ceramics International 40(3) (2014) 4117-4126.

[19] S. Fang, K.S. Brinkman, F. Chen, Hydrogen permeability and chemical stability of Ni–$BaZr_{0.1}Ce_{0.7}Y_{0.1}Yb_{0.1}O_{3-\delta}$ membrane in concentrated H_2O and CO_2, Journal of membrane science 467 (2014) 85-92.

[20] Z. Zhu, W. Sun, L. Yan, W. Liu, W. Liu, Synthesis and hydrogen permeation of Ni–Ba $(Zr_{0.1}Ce_{0.7}Y_{0.2})O_{3-\delta}$ metal–ceramic asymmetric membranes, International journal of hydrogen energy 36(10) (2011) 6337-6342.

[21] S. Fang, L. Bi, C. Yang, L. Yan, C. Chen, W. Liu, H_2S poisoning and regeneration of Ni–$BaZr_{0.1}Ce_{0.7}Y_{0.2}O_{3-\delta}$ at intermediate temperature, Journal of alloys and compounds 475(1-2) (2009) 935-939.

[22] C. Zuo, T. Lee, S. Dorris, U. Balachandran, M. Liu, Composite Ni–$Ba(Zr_{0.1}Ce_{0.7}Y_{0.2})O_3$ membrane for hydrogen separation, Journal of Power Sources 159(2) (2006) 1291-1295.

[23] C. Zuo, S. Dorris, U. Balachandran, M. Liu, Effect of Zr-doping on the chemical stability and hydrogen permeation of the Ni−$BaCe_{0.8}Y_{0.2}O_{3-\alpha}$ mixed protonic−electronic conductor, Chemistry of materials 18(19) (2006) 4647-4650.

[24] W.A. Rosensteel, S. Ricote, N.P. Sullivan, Hydrogen permeation through dense $BaCe_{0.8}Y_{0.2}O_{3\text{-delta}}$-$Ce_{0.8}Y_{0.2}O_{2\text{-delta}}$ composite-ceramic hydrogen separation membranes, International Journal of Hydrogen Energy 41(4) (2016) 2598-2606.

[25] W.A. Rosensteel, N.P. Sullivan, Fabrication and hydrogen permeation through novel $BaZr_{0.9}Y_{0.1}O_{3-\delta}$–Cu composite ceramic-metallic membranes, International Journal of Hydrogen Energy 42(7) (2017) 4216-4223.

[26] Y. Wei, J. Xue, W. Fang, Y. Chen, H. Wang, J. Caro, Enhanced stability of Zr-doped $Ba(CeTb)O_{3-\delta}$-Ni cermet membrane for hydrogen separation, Chemical Communications 51(58) (2015) 11619-11621.

[27] S. Escolastico, C. Solis, C. Kjølseth, J. Serra, Outstanding hydrogen permeation through CO_2-stable dual-phase ceramic membranes, Energy & Environmental Science 7(11) (2014) 3736-3746.

[28] J.M. Polfus, Z. Li, W. Xing, M.F. Sunding, J.C. Walmsley, M.-L. Fontaine, P.P. Henriksen, R. Bredesen, Chemical stability and H_2 flux degradation of cercer membranes based on lanthanum tungstate and lanthanum chromite, Journal of Membrane Science 503 (2016) 42-47.

[29] J.S. Fish, S. Ricote, F. Lenrick, L.R. Wallenberg, T.C. Holgate, R. O'Hayre, N. Bonanos, Synthesis by spark plasma sintering of a novel protonic/electronic conductor composite: $BaCe_{0.2}Zr_{0.7}Y_{0.1}O_{3-\delta}/Sr_{0.95}Ti_{0.9}Nb_{0.1}O_{3-\delta}$ (BCZY27/STN95), Journal of Materials Science 48(18) (2013) 6177-6185.

[30] D. Montaleone, E. Mercadelli, A. Gondolini, P. Pinasco, A. Sanson, On the compatibility of dual phase $BaCe_{0.65}Zr_{0.2}Y_{0.15}O_3$-based membrane for hydrogen separation application, Ceramics International 43(13) (2017) 10151-10157.

[31] E. Mercadelli, D. Montaleone, A. Gondolini, P. Pinasco, A. Sanson, Tape-cast asymmetric membranes for hydrogen separation, Ceramics International 43(11) (2017) 8010-8017.

[32] C. Mortalò, E. Rebollo, S. Escolástico, S. Deambrosis, K. Haas-Santo, M. Rancan, R. Dittmeyer, L. Armelao, M. Fabrizio, Enhanced sulfur tolerance of $BaCe_{0.65}Zr_{0.20}Y_{0.15}O_{3-\delta}$-$Ce_{0.85}Gd_{0.15}O_{2-\delta}$ composite for hydrogen separation membranes, Journal of Membrane Science 564 (2018) 123-132.

[33] C. Mortalò, A. Santoru, C. Pistidda, E. Rebollo, M. Boaro, C. Leonelli, M. Fabrizio, Structural evolution of $BaCe_{0.65}Zr_{0.20}Y_{0.15}O_{3-\delta}$-$Ce_{0.85}Gd_{0.15}O_{2-\delta}$ composite MPEC membrane by in-situ synchrotron XRD analyses, Materials Today Energy 13 (2019) 331-341.

[34] C. Mortalò, M. Boaro, E. Rebollo, V. Zin, E. Aneggi, M. Fabrizio, A. Trovarelli, Insights on the Interfacial Processes Involved in the Mechanical and Redox Stability of the $BaCe_{0.65}Zr_{0.20}Y_{0.15}O_{3-\delta}$–$Ce_{0.85}Gd_{0.15}O_{2-\delta}$ Composite, ACS Applied Energy Materials 3(10) (2020) 9877-9888.

[35] F. Zeng, J. Malzbender, S. Baumann, W. Zhou, M. Ziegner, A. Nijmeijer, O. Guillon, R. Schwaiger, W.A. Meulenberg, Mechanical reliability of $Ce_{0.8}Gd_{0.2}O_{2-\delta}$-$FeCo_2O_4$ dual phase membranes synthesized by one-step solid-state reaction, Journal of the American Ceramic Society 104(4) (2021) 1814-1830.

[36] F. Zeng, J. Malzbender, S. Baumann, F. Schulze-Küppers, M. Krüger, A. Nijmeijer, O. Guillon, W.A. Meulenberg, Micromechanical Characterization of $Ce_{0.8}Gd_{0.2}O_{2-\delta}$–$FeCo_2O_4$ Dual Phase Oxygen Transport Membranes, Advanced engineering materials 22(6) (2020) 1901558.

[37] F. Zeng, J. Malzbender, S. Baumann, A. Nijmeijer, L. Winnubst, O. Guillon, R. Schwaiger, W.A. Meulenberg, Residual stress and mechanical strength of $Ce_{0.8}Gd_{0.2}O_{2-\delta}$-$FeCo_2O_4$ dual phase oxygen transport membranes, Journal of the European Ceramic Society (2021).

[38] F. Zeng, J. Malzbender, S. Baumann, A. Nijmeijer, L. Winnubst, M. Ziegner, O. Guillon, R. Schwaiger, W.A. Meulenberg, Optimization of sintering conditions for improved microstructural and mechanical properties of dense $Ce_{0.8}Gd_{0.2}O_{2-\delta}$-$FeCo_2O_4$ oxygen transport membranes, Journal of the European Ceramic Society 41(1) (2021) 509-516.

[39] T. Nithyanantham, S. Biswas, N. Nagendra, S. Bandopadhyay, Studies on mechanical behavior of LSFT-CGO dual-phase membranes at elevated temperatures in ambient air and slightly reducing environments, Ceramics International 40(6) (2014) 7783-7790.

[40] S. Kim, S.H. Kim, K.S. Lee, J.H. Yu, Y.-H. Seong, I.S. Han, Mechanical properties of LSCF ($La_{0.6}Sr_{0.4}Co_{0.2}Fe_{0.8}O_{3-\delta}$)–GDC ($Ce_{0.9}Gd_{0.1}O_{2-\delta}$) for oxygen transport membranes, Ceramics International 43(2) (2017) 1916-1921.

[41] K. Raju, S. Kim, C.J. Hyung, J.H. Yu, Y.-H. Seong, S.-H. Kim, I.-S. Han, Optimal sintering temperature for $Ce_{0.9}Gd_{0.1}O_{2-\delta}$–$La_{0.6}Sr_{0.4}Co_{0.2}Fe_{0.8}O_{3-\delta}$ composites evaluated through their microstructural, mechanical and elastic properties, Ceramics International 45(1) (2019) 1460-1463.

[42] R.O. Silva, J. Malzbender, F. Schulze-Küppers, S. Baumann, O. Guillon, Mechanical properties and lifetime predictions of dense $SrTi_{1-x}Fe_xO_{3-\delta}$ (x= 0.25, 0.35, 0.5), Journal of the European Ceramic Society 37(7) (2017) 2629-2636.

[43] V. Stournari, W. Deibert, M. Ivanova, C. Krautgasser, R. Bermejo, J. Malzbender, Mechanical properties of tape casted Lanthanum Tungstate for membrane substrate application, Ceramics International 42(14) (2016) 15177-15182.

[44] L. Wang, R. Dou, G. Wang, Y. Li, M. Bai, D. Hall, Y. Chen, A case study of mechanical properties of perovskite-structured $Ba_{0.5}Sr_{0.5}Co_{0.8}Fe_{0.2}O_{3-\delta}$ oxygen transport membrane, Journal of the European Ceramic Society 38(2) (2018) 647-653.

[45] G.D. Quinn, R.C. Bradt, On the Vickers indentation fracture toughness test, Journal of the American Ceramic Society 90(3) (2007) 673-680.

[46] M. Sebastiani, K. Johanns, E.G. Herbert, G.M. Pharr, Measurement of fracture toughness by nanoindentation methods: Recent advances and future challenges, Current Opinion in Solid State and Materials Science 19(6) (2015) 324-333.

[47] M. Sebastiani, K. Johanns, E.G. Herbert, F. Carassiti, G.M. Pharr, A novel pillar indentation splitting test for measuring fracture toughness of thin ceramic coatings, Philosophical Magazine 95(16-18) (2015) 1928-1944.

[48] M. Sebastiani, C. Eberl, E. Bemporad, G.M. Pharr, Depth-resolved residual stress analysis of thin coatings by a new FIB–DIC method, Materials Science and Engineering: A 528(27) (2011) 7901-7908.

[49] M. Sebastiani, E. Bemporad, F. Carassiti, N. Schwarzer, Residual stress measurement at the micrometer scale: Focused ion beam (FIB) milling and nanoindentation testing, Philosophical Magazine 91(7-9) (2011) 1121-1136.

[50] A. Davydok, B.N. Jaya, O. Robach, O. Ulrich, J.-S. Micha, C. Kirchlechner, Analysis of the full stress tensor in a micropillar: Ability of and difficulties arising during synchrotron based µLaue diffraction, Materials & Design 108 (2016) 68-75.

[51] C.M. Lauener, L. Petho, M. Chen, Y. Xiao, J. Michler, J.M. Wheeler, Fracture of Silicon: Influence of rate, positioning accuracy, FIB machining, and elevated temperatures on toughness measured by pillar indentation splitting, Materials & Design 142 (2018) 340-349.

[52] W. Zhou, J. Malzbender, F. Zeng, W. Deibert, O. Guillon, R. Schwaiger, W.A. Meulenberg, Mechanical properties of $BaCe_{0.65}Zr_{0.2}Y_{0.15}O_{3-\delta}$ proton-conducting material determined using different nanoindentation methods, Journal of the European Ceramic Society 40(15) (2020) 5653-5661.

[53] Y.J. Kang, H.J. Park, G.M. Choi, The effect of grain size on the low-temperature electrical conductivity of doped CeO_2, Solid State Ionics 179(27-32) (2008) 1602-1605.

[54] C.A. Schneider, W.S. Rasband, K.W. Eliceiri, NIH Image to ImageJ: 25 years of image analysis, Nature methods 9(7) (2012) 671-675.

[55] W.C. Oliver, G.M. Pharr, Measurement of hardness and elastic modulus by instrumented indentation: Advances in understanding and refinements to methodology, Journal of materials research 19(1) (2004) 3-20.

[56] W.C. Oliver, G.M. Pharr, An improved technique for determining hardness and elastic modulus using load and displacement sensing indentation experiments, Journal of materials research 7(6) (1992) 1564-1583.

[57] A. Atkinson, A. Selcuk, Mechanical behaviour of ceramic oxygen ion-conducting membranes, Solid State Ionics 134(1-2) (2000) 59-66.

[58] J. Gong, Determining indentation toughness by incorporating true hardness into fracture mechanics equations, Journal of the European Ceramic Society 19(8) (1999) 1585-1592.

[59] A.-N. Wang, J.F. Nonemacher, G. Yan, M. Finsterbusch, J. Malzbender, M. Krüger, Mechanical properties of the solid electrolyte Al-substituted $Li_7La_3Zr_2O_{12}$ (LLZO) by utilizing micro-pillar indentation splitting test, Journal of the European Ceramic Society 38(9) (2018) 3201-3209.

[60] C.B. Ponton, R.D. Rawlings, Vickers indentation fracture toughness test Part 1 Review of literature and formulation of standardised indentation toughness equations, Materials Science and Technology 5(9) (1989) 865-872.

[61] C. Ponton, R. Rawlings, Vickers indentation fracture toughness test Part 2 Application and critical evaluation of standardised indentation toughness equations, Materials Science and Technology 5(10) (1989) 961-976.

[62] M. Ghidelli, M. Sebastiani, K.E. Johanns, G.M. Pharr, Effects of indenter angle on micro‐scale fracture toughness measurement by pillar splitting, Journal of the American Ceramic Society 100(12) (2017) 5731-5738.

[63] A.J. Lunt, G. Mohanty, T.K. Neo, J. Michler, A.M. Korsunsky, Microscale resolution fracture toughness profiling at the zirconia-porcelain interface in dental prostheses, Micro+ Nano Materials, Devices, and Systems, International Society for Optics and Photonics, 2015, p. 96685S.

[64] M.E. Ivanova, S. Escolástico, M. Balaguer, J. Palisaitis, Y.J. Sohn, W.A. Meulenberg, O. Guillon, J. Mayer, J.M. Serra, Hydrogen separation through tailored dual phase membranes with nominal composition $BaCe_{0.8}Eu_{0.2}O_{3-\delta}$:$Ce_{0.8}Y_{0.2}O_{2-\delta}$ at intermediate temperatures, Scientific reports 6(1) (2016) 1-14.

[65] P. Datta, P. Majewski, F. Aldinger, Synthesis and reactivity study of gadolinia doped ceria–nickel: A potential anode material for solid oxide fuel cell, Journal of alloys and compounds 455(1-2) (2008) 454-460.

[66] W. Zhou, J. Malzbender, W. Deibert, O. Guillon, R. Schwaiger, A. Nijmeijer, W.A. Meulenberg, High temperature compressive creep behavior of $BaCe_{0.65}Zr_{0.2}Y_{0.15}O_{3-\delta}$ in air and 4% H_2/Ar, Journal of the American Ceramic Society 104(6) (2021) 2730-2740.

[67] X. Li, X. Xie, J. Gonzalez-Julian, J. Malzbender, R. Yang, Mechanical and oxidation behavior of textured Ti_2AlC and Ti_3AlC_2 MAX phase materials, Journal of the European Ceramic Society 40(15) (2020) 5258-5271.

[68] X. Li, J. Gonzalez-Julian, J. Malzbender, Fabrication and mechanical performance of Ti_2AlN prepared by FAST/SPS, Journal of the European Ceramic Society (2020).

[69] F. Zeng, S. Baumann, J. Malzbender, A. Nijmeijer, L. Winnubst, O. Guillon, R. Schwaiger, W.A. Meulenberg, Enhancing oxygen permeation of solid-state reactive sintered $Ce_{0.8}Gd_{0.2}O_{2-\delta}$-$FeCo_2O_4$ composite by optimizing the powder preparation method, Journal of Membrane Science 628 (2021) 119248.

[70] K.-D. Kreuer, S.J. Paddison, E. Spohr, M. Schuster, Transport in proton conductors for fuel-cell applications: simulations, elementary reactions, and phenomenology, Chemical reviews 104(10) (2004) 4637-4678.

[71] J. Sunarso, S. Baumann, J. Serra, W. Meulenberg, S. Liu, Y. Lin, J.D. Da Costa, Mixed ionic–electronic conducting (MIEC) ceramic-based membranes for oxygen separation, Journal of membrane science 320(1-2) (2008) 13-41.

[72] K.S. Lee, G.-H. Jo, Y.-G. Jung, Y. Byeun, Effect of carbon content on the mechanical behavior of MgO–C refractories characterized by Hertzian indentation, Ceramics International 42(8) (2016) 9955-9962.

[73] N.X. Randall, M. Vandamme, F.-J. Ulm, Nanoindentation analysis as a two-dimensional tool for mapping the mechanical properties of complex surfaces, Journal of materials research 24(3) (2009) 679-690.

[74] G. Constantinides, K.R. Chandran, F.-J. Ulm, K. Van Vliet, Grid indentation analysis of composite microstructure and mechanics: Principles and validation, Materials Science and Engineering: A 430(1-2) (2006) 189-202.

[75] L.S. de Vasconcelos, R. Xu, J. Li, K. Zhao, Grid indentation analysis of mechanical properties of composite electrodes in Li-ion batteries, Extreme Mechanics Letters 9 (2016) 495-502.

[76] M. Lilli, E. Rossi, J. Tirillò, F. Sarasini, L. Di Fausto, T. Valente, C. González, A. Fernández, C.S. Lopes, R. Moscatelli, Quantitative multi-scale characterization of single basalt fibres: Insights into strength loss mechanisms after thermal conditioning, Materials Science and Engineering: A 797 (2020) 139963.

[77] J. Ast, M. Ghidelli, K. Durst, M. Göken, M. Sebastiani, A.M. Korsunsky, A review of experimental approaches to fracture toughness evaluation at the micro-scale, Materials & Design 173 (2019) 107762.

[78] M.Z. Mughal, H.-Y. Amanieu, R. Moscatelli, M. Sebastiani, A comparison of microscale techniques for determining fracture toughness of $LiMn_2O_4$ particles, Materials 10(4) (2017) 403.

[79] M.Z. Mughal, R. Moscatelli, H.-Y. Amanieu, M. Sebastiani, Effect of lithiation on micro-scale fracture toughness of $Li_xMn_2O_4$ cathode, Scripta Materialia 116 (2016) 62-66.

[80] G. Yan, J. Malzbender, S. Fu, J.P. Gross, S. Yu, R.-A. Eichel, R. Schwaiger, Fracture behavior of solid electrolyte LATP material based on micro-pillar splitting method, Journal of the European Ceramic Society 41(10) (2021) 5240-5247.

[81] B. Lawn, A. Evans, A model for crack initiation in elastic/plastic indentation fields, Journal of Materials Science 12(11) (1977) 2195-2199.

[82] L. Robben, E. Merzlyakova, P. Heitjans, T.M. Gesing, Symmetry reduction due to gallium substitution in the garnet $Li_{6.43(2)}Ga_{0.52(3)}La_{2.67(4)}Zr_2O_{12}$, Acta Crystallographica Section E: Crystallographic Communications 72(3) (2016) 287-289.

[83] J. Rödel, Interaction between crack deflection and crack bridging, Journal of the European Ceramic Society 10(3) (1992) 143-150.

[84] K.T. Faber, A.G. Evans, Crack deflection processes—I. Theory, Acta metallurgica 31(4) (1983) 565-576.

[85] R.W. Rice, Porosity of ceramics: properties and applications, CRC Press1998.

[86] J.B. Davis, A. Kristoffersson, E. Carlström, W.J. Clegg, Fabrication and crack deflection in ceramic laminates with porous interlayers, Journal of the American Ceramic Society 83(10) (2000) 2369-2374.

[87] K. Blanks, A. Kristoffersson, E. Carlström, W. Clegg, Crack deflection in ceramic laminates using porous interlayers, Journal of the European Ceramic Society 18(13) (1998) 1945-1951.

[88] Y. Chang, R. Bermejo, G.L. Messing, Improved fracture behavior of alumina microstructural composites with highly textured compressive layers, Journal of the American Ceramic Society 97(11) (2014) 3643-3651.

Appendix A5

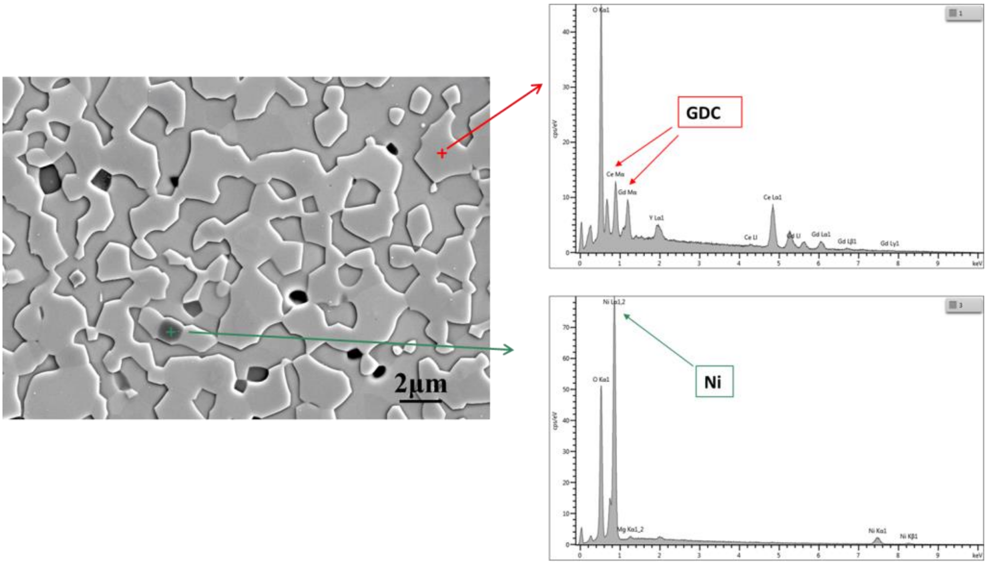

Figure A5.1 EDX investigation results demonstrating Ni enrichment within GDC15.

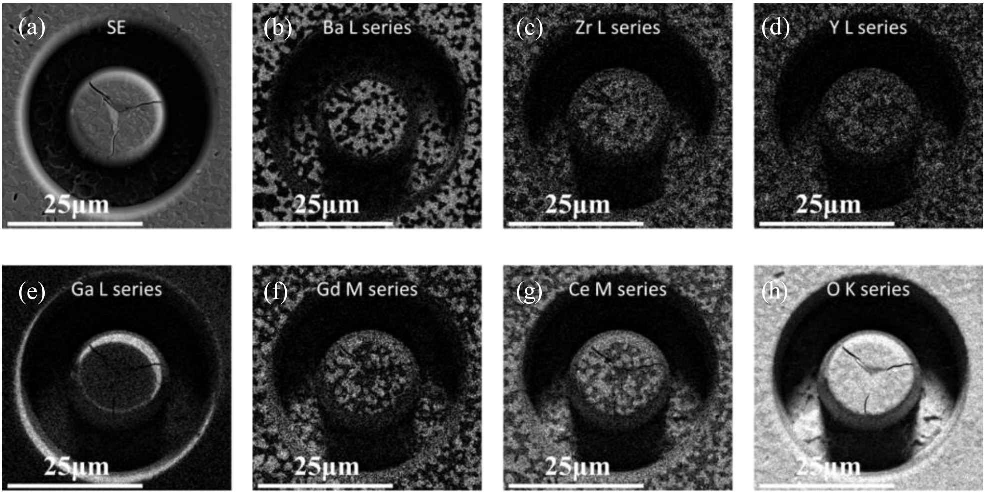

Figure A5.2 EDX element mapping of a post-test pillar presenting (a) the SEM micrograph and the elemental distribution of (b) Ba, (c) Zr, (d) Y, (e) Ga, (f) Gd, (g) Ce, (h) O. The shadow, which exists in every mapping, is a result of the topography of the sample surface.

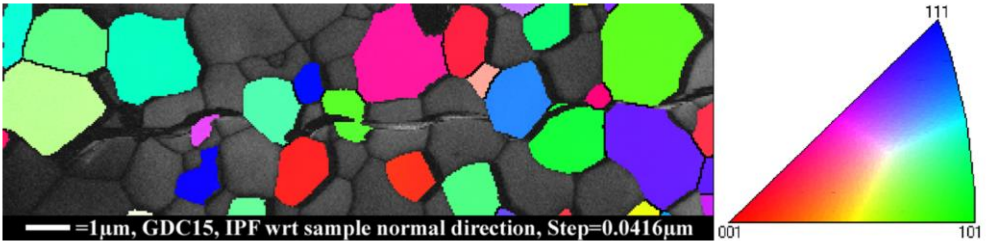

Figure A5.3 EBSD mapping to demonstrate the crack deflections avoiding GDC15 (coloured regions).

CHAPTER 6

Reflections and perspectives

6.1 Introduction

This chapter represents the implications of the overall conclusions on material preparation improvements, the mechanical properties and associated microstructural characteristics of $BaCe_{0.65}Zr_{0.2}Y_{0.15}O_{3-\delta}$ and $BaCe_{0.65}Zr_{0.2}Y_{0.15}O_{3-\delta}$-$Ce_{0.85}Gd_{0.15}O_{2-\delta}$ proton conducting membranes, with suggestions for further improvements in the design of materials and components. Additionally, a couple of aspects which might affect the long-term operational performance of the membrane are proposed for further study.

6.2 Material preparation

As shown in **Chapter 2**, high density and large grain size $BaCe_{0.65}Zr_{0.2}Y_{0.15}O_{3-\delta}$ material can be obtained via improved sintering profile. After pre-calcination, with 0.5 wt.% NiO as sintering aid, single-phase $BaCe_{0.65}Zr_{0.2}Y_{0.15}O_{3-\delta}$ was obtained after 1500 °C / 5 h sintering, with density higher than 99 % and average grain size ~ 13 µm, without secondary phase (BaY_2NiO_5) being observed. Thus, the conductivity, especially the grain boundary conductivity, of the prepared $BaCe_{0.65}Zr_{0.2}Y_{0.15}O_{3-\delta}$ is supposed to be unharmed [1, 2].

However, as shown in **Chapter 5**, when the $Ce_{0.85}Gd_{0.15}O_{2-\delta}$ is introduced into the material forming dual-phase $BaCe_{0.65}Zr_{0.2}Y_{0.15}O_{3-\delta}$-$Ce_{0.85}Gd_{0.15}O_{2-\delta}$, the grain sizes of both phases are reduced to ~ 1 µm. This potentially is a result of $Ce_{0.85}Gd_{0.15}O_{2-\delta}$ limiting the grain growth of $BaCe_{0.65}Zr_{0.2}Y_{0.15}O_{3-\delta}$, but needs further investigation to confirm it and eventually obtain a material with larger grain sizes.

For the convenience of further thermal, mechanical and hydrogen separation investigations, material preparation procedure can be simplified via purchasing $BaCe_{0.65}Zr_{0.2}Y_{0.15}O_{3-\delta}$ and $Ce_{0.85}Gd_{0.15}O_{2-\delta}$ commercial powders. An initial characterization of the microstructure of the as-received commercial powders is shown in Figure 6.1.

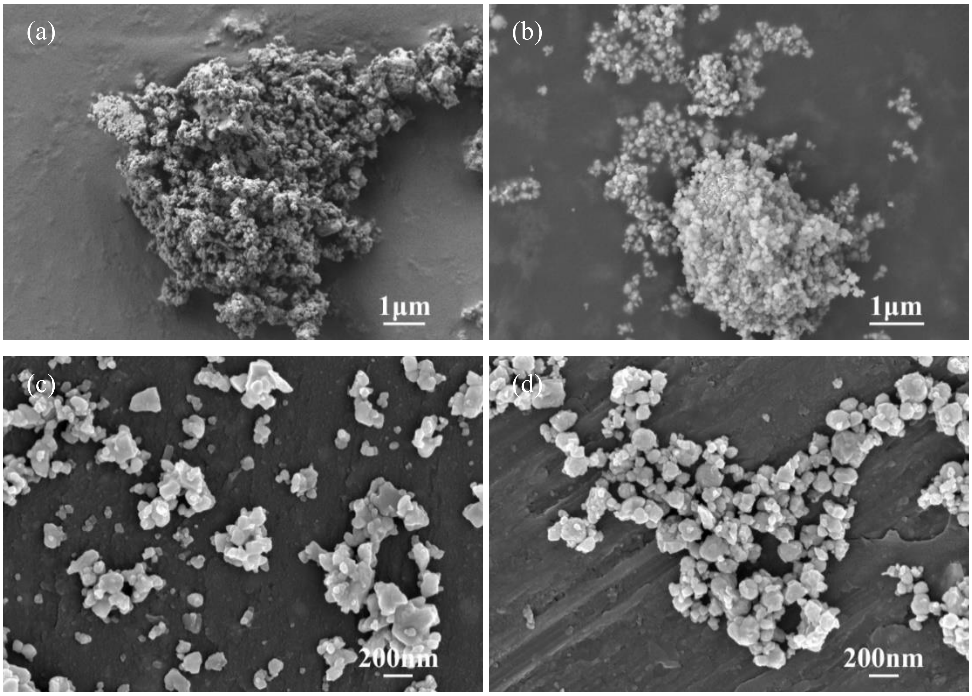

Figure 6.1 SEM microstructures of the as-received BCZ20Y15 (a) and GDC15 (b) commercial powders from Marion Technologies (France), and their corresponding microstructures after ultrasonic treatment (c), (d).

Severe agglomeration can be observed in both as-received powders (Figure 6.1 (a, b)). After ultrasonic treatment, their corresponding particle size are both ~ 100 nm (Figure 6.1 (c, d)). Their corresponding specific surface areas, 6.7 and 14.7 m^2/g, also verifying their fine primary grain sizes.

After one-day ball-mixing, the mixture of the two powders with a nominal 50:50 vol.% shows no very high homogeneity, which can be also observed clearly in the sintered microstructure (see Figure 6.2).

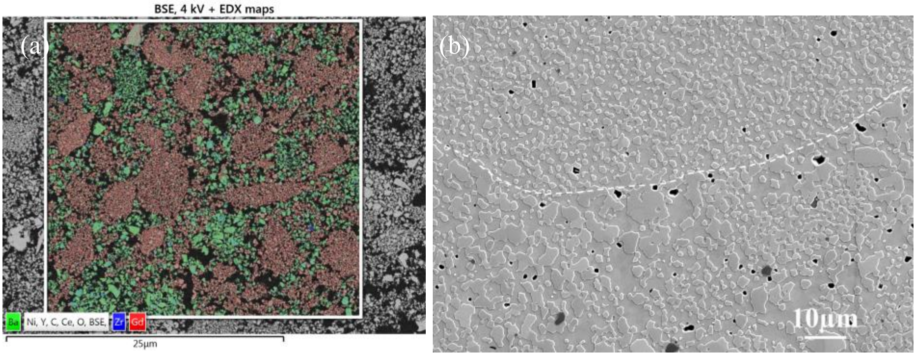

Figure 6.2 (a) SEM microstructure and EDX map of the mixture of as-received BCZ20Y15 and GDC15 powders. (b) SEM microstructure of the sintered BCZ20Y15-GDC15. The dashed line marks the inhomogeneity of the microstructure.

The observed inhomogeneity potentially resulted from the severe agglomeration of the two powders (Figure 6.1 (a, b)). Further investigation should start from the ball-mixing profile to obtain homogeneous materials.

6.3 Mechanical properties

Elastic modulus and hardness represent the elastic and plastic responses of the material under the applied load, which can be fundamental parameters for finite elemental method (FEM) simulation. Fracture toughness represents the energy that can be absorbed by the material during the crack propagation, which indicates the material fracture resistance. Elastic modulus, hardness and fracture toughness were in detailed studied combined with microstructural analysis on $BaCe_{0.65}Zr_{0.2}Y_{0.15}O_{3-\delta}$ and 50 wt.% $BaCe_{0.65}Zr_{0.2}Y_{0.15}O_{3-\delta}$-50 wt.% $Ce_{0.85}Gd_{0.15}O_{2-\delta}$ in **Chapter 3** and **Chapter 5**. The dual-phase material's elastic and plastic responses and fracture resistance are all enhanced compared with the single-phase material, due to the introduction of $Ce_{0.85}Gd_{0.15}O_{2-\delta}$, facilitating the further design of robust and reliable components. A further systematically investigation on the dual-phase material with different phase ratios might be necessary for a comprehensive understanding of this dual-phase materials' elastic and plastic responses. Besides that, fracture stress should be a fundamental input data for further life time prediction [3], thus necessary to be investigated in detail. Furthermore, investigations of elastic modulus, hardness, fracture toughness and fracture stress at elevated temperatures and under different application relevant conditions are highly suggested.

Under application relevant conditions, these proton conducting membranes are operated at an intermediate temperature (~ 600 – 800 °C) and are potentially exposed to high pressure differences over the membrane [4, 5]. Under such harsh conditions, membranes have to remain structurally and geometrically stable, preferably over a period of many years of operation, which means that the creep behavior is an aspect of concern. In **Chapter 4**, the compressive creep behavior of $BaCe_{0.65}Zr_{0.2}Y_{0.15}O_{3-\delta}$ at elevated temperature in different atmospheres was studied. The observed creep rate in 4% H_2/Ar, at 850 °C is somewhat higher than the suggested critical compressive creep rate for commercial use of the membrane material (1% per year) [6]. However, since the application temperature (~ 600 – 800 °C) is also lower than the test temperature, a rough extrapolation can be made of the creep rate of $BaCe_{0.65}Zr_{0.2}Y_{0.15}O_{3-\delta}$ at the application temperature. This leads to a creep rate which is close to the 1% per year, meaning that when designing the membrane components, the thermomechanical stability, in particular the creep behavior, should be one aspect of concern. A further creep behavior investigation on the dual phase $BaCe_{0.65}Zr_{0.2}Y_{0.15}O_{3-\delta}$-$Ce_{0.85}Gd_{0.15}O_{2-\delta}$ would benefit both the long-term structural stability analysis and the comprehensive understanding of interaction between the two individual phases.

6.4 Conclusions

In this thesis, dense single phase $BaCe_{0.65}Zr_{0.2}Y_{0.15}O_{3-\delta}$ and dual phase $BaCe_{0.65}Zr_{0.2}Y_{0.15}O_{3-\delta}$-$Ce_{0.85}Gd_{0.15}O_{2-\delta}$ proton membranes are synthesised through a solid-state reaction sintering method using $BaCO_3$, CeO_2, ZrO_2, Y_2O_3 and Gd_2O_3 as raw materials.

It is reflected that high density large grain size $BaCe_{0.65}Zr_{0.2}Y_{0.15}O_{3-\delta}$ can be obtained by adapting the improved sintering profile. The elastic and plastic responses of the material can be significantly enhanced via introducing $Ce_{0.85}Gd_{0.15}O_{2-\delta}$ into the material forming $BaCe_{0.65}Zr_{0.2}Y_{0.15}O_{3-\delta}$-$Ce_{0.85}Gd_{0.15}O_{2-\delta}$. The creep behavior of $BaCe_{0.65}Zr_{0.2}Y_{0.15}O_{3-\delta}$ demonstrates the necessity to concern the thermomechanical stability when applying this material into a membrane component.

However, for potential industrial applications, further investigations regarding the fracture stress of $BaCe_{0.65}Zr_{0.2}Y_{0.15}O_{3-\delta}$ and $BaCe_{0.65}Zr_{0.2}Y_{0.15}O_{3-\delta}$-$Ce_{0.85}Gd_{0.15}O_{2-\delta}$ are necessary. These analysis will be fundamental input data for further life-time prediction. Creep behavior investigation of $BaCe_{0.65}Zr_{0.2}Y_{0.15}O_{3-\delta}$-$Ce_{0.85}Gd_{0.15}O_{2-\delta}$ would benefit the long-term structural stability analysis. In addition, there is a necessity to systematically study the mechanical properties of the dual phase $BaCe_{0.65}Zr_{0.2}Y_{0.15}O_{3-\delta}$-$Ce_{0.85}Gd_{0.15}O_{2-\delta}$ with different phase ratios for more comprehensive understanding of the mechanical interactions between the two individual phases in the membrane.

References

[1] Y. Huang, R. Merkle, J. Maier, Effects of NiO addition on sintering and proton uptake of Ba(Zr,Ce,Y)$O_{3-\delta}$, Journal of Materials Chemistry A (2021).

[2] D.S. Yun, J. Kim, S.-J. Kim, J.-H. Lee, J.-N. Kim, H.C. Yoon, J.H. Yu, M. Kwak, H. Yoon, Y. Cho, Structural and electrochemical properties of dense yttria-doped barium zirconate prepared by solid-state reactive sintering, Energies 11(11) (2018) 3083.

[3] F. Zeng, J. Malzbender, S. Baumann, W. Zhou, M. Ziegner, A. Nijmeijer, O. Guillon, R. Schwaiger, W.A. Meulenberg, Mechanical reliability of $Ce_{0.8}Gd_{0.2}O_{2-\delta}$-$FeCo_2O_4$ dual phase membranes synthesized by one-step solid-state reaction, Journal of the American Ceramic Society 104(4) (2021) 1814-1830.

[4] W. Deibert, M.E. Ivanova, S. Baumann, O. Guillon, W.A. Meulenberg, Ion-conducting ceramic membrane reactors for high-temperature applications, Journal of membrane science 543 (2017) 79-97.

[5] E. Rebollo, C. Mortalo, S. Escolástico, S. Boldrini, S. Barison, J.M. Serra, M. Fabrizio, Exceptional hydrogen permeation of all-ceramic composite robust membranes based on $BaCe_{0.65}Zr_{0.20}Y_{0.15}O_{3-\delta}$ and Y-or Gd-doped ceria, Energy & Environmental Science 8(12) (2015) 3675-3686.

[6] J. Yi, H. Lein, T. Grande, S. Yakovlev, H. Bouwmeester, High-temperature compressive creep behaviour of the perovskite-type oxide $Ba_{0.5}Sr_{0.5}Co_{0.8}Fe_{0.2}O_{3-\delta}$, Solid State Ionics 180(36-39) (2009) 1564-1568.

Acknowledgements

This work was curried out at the Institute of Energy and Climate Research, Materials Synthesis and Processing (IEK-1) and Microstructure and Properties (IEK-2), at the Forschungszentrum Jülich GmbH. I would like to give my appreciation to all those who have participated and contributed to this work.

Firstly, I want to thank Prof. Dr. W. A. Meulenberg, Prof. Dr. L. Singheiser and Prof. Dr. R. Schwaiger for providing the opportunity to carry out this PhD project and offering support in my application for PhD funding.

Prof. Dr. W. A. Meulenberg, as my supervisor, guided me through all the scientific and cultural hurdles during my time as a PhD student, for which I am grateful.

In particular, I would like to thank my promoters at Twente - Prof. Dr. A. Nijmeijer and Prof. Dr. L. Winnubst. We held a series of meetings for scientific discussions and project management. We had meaningful discussions on the scientific areas which helped me to improve the fundamental scientific ideas.

To my daily supervisor at IEK-2 - Dr. J. Malzbender - I am grateful for the enormous amount of ideas and valuable advice he has provided me with regarding my PhD project and associated activities.

As my advisor at IEK-1, Dr. W. Deibert is greatly appreciated. He has contributed to the work by providing meaningful scientific inputs, in particular in areas related to sample preparation.

With no doubt, I would also like to express my gratitude to the directors of the Institutes in Jülich - Prof. R. Schwaiger and Prof. O. Guillon. They supported my participation in the conferences and provided a lot of advice on scientific aspects, which were helpful during the completion of this work.

I am also very grateful to Ms. T. Osipova and Mr. M. Turiaux for their support with thermodynamic tests, Mr. S. Heinz for his assistance with lab work, Dr. D. Grüner and Dr. E. Wessel for SEM investigations, Ms. D. Esser for FIB operations, Mr. M. Ziegner for XRD measurements, Ms. S. Schwartz-Lückge and Ms. A. Hilgers for particle morphological measurements, Mr. V. Gutzeit, Mr. J. Bartsch and M. Kappertz for assistance with sample preparation and Mr. V. Bader for the thermal treatment. Without all these experimental supports it would not have been possible to obtain all these meaningful results.

Many thanks also to Prof. M. Krüger and Dr. F. Schulze-Küppers for all their support through my first years as a PhD student.

It would be incomplete without thanks to my families. Many thanks to my parents and my grandmother for understanding and supporting my decision to study abroad.

In the end, I’d like to acknowledge the funding for my study from China Scholarship Council (CSC) which I greatly appreciate.

About the author

Wenyu Zhou was born on 14th July, 1993, in Yichun, China. After finishing his high school (Heilongjiang Provincial Experimental High School) in Harbin, he went to Harbin Institute of Technology (Harbin, China) studying in Materials Forming and Controlling Engineering, where he got his bachelor degree. After that, he continued to study at the same university and finished his Master degree in Materials Processing Engineering.

His interest in science drove him to Europe, where he studies as a jointed PhD student at Forschungszentrum Jülich GmbH (Jülich, Germany) and University of Twente (Enschede, the Netherlands). His PhD project, under the supervision of Prof. Dr. W. A. Meulenberg and Prof. Dr. Arian Nijmeijer, which sponsored by China Scholarship Council (CSC), focused on mechanical properties of proton conducting membranes. During his PhD career, he published four papers as first author in high level peer-reviewed journals (e.g. Journal of the American Ceramic Society and Journal of the European Ceramic Society).

Schriften des Forschungszentrums Jülich
Reihe Energie & Umwelt / Energy & Environment

Band / Volume 572
Developing an integrated value-based institutional framework for analyzing nexus governance challenges – the case study of Germany
C. Märker (2022), 290 pp
ISBN: 978-3-95806-617-5

Band / Volume 573
Ecological sanitation via thermophilic co-composting of humanure and biochar as an approach to climate-smart agriculture
D. Castro Herrera (2022), XVIII, 127 pp
ISBN: 978-3-95806-622-9

Band / Volume 574
Towards 3D crosshole GPR full-waveform inversion
A. Mozaffari (2022), viii, 122 pp
ISBN: 978-3-95806-623-6

Band / Volume 575
Investigations of the atmospheric OH, HO2 and RO2 radical chemical budgets and their impact on tropospheric ozone formation in a rural area in West-Germany in the JULIAC 2019 campaign
C. Cho (2022), 182 pp
ISBN: 978-3-95806-625-0

Band / Volume 576
Thermochemische Beständigkeit von Carbonat-Keramik-Membranen für die CO_2-Abtrennung in Wassergas-Shift-Reaktoren
U. Gude (2022), X, 176, LXIII pp
ISBN: 978-3-95806-626-7

Band / Volume 577
Neue Ziele auf alten Wegen?
Strategien für eine treibhausgasneutrale Energieversorgung bis zum Jahr 2045
D. Stolten, P. Markewitz, T. Schöb, F. Kullmann, S. Risch, T. Groß,
M. Hoffmann, D. Franzmann, T. Triesch, S. Kraus, R. Maier, B. Gillessen,
H. Heinrichs, N. Pflugradt, T. Grube, J. Linssen, L. Kotzur (2022), VI, 81 pp
ISBN: 978-3-95806-627-4

Band / Volume 578
Improving stationary and mobile cosmic ray neutron soil moisture measurements
Assessment of the cosmic ray neutron uncertainty
and the potential of the thermal neutron signal
J. C. Jakobi (2022), xxiii, 137 pp
ISBN: 978-3-95806-628-1

Schriften des Forschungszentrums Jülich
Reihe Energie & Umwelt / Energy & Environment

Band / Volume 579
Application-Specific Calibration of Condensation Particle Counters under Low Pressure Conditions
O. B. F. Bischof (2022), ix, 137 pp
ISBN: 978-3-95806-629-8

Band / Volume 580
Konzepte und Potenziale von Demonstrationsanlagen für die Produktion von erneuerbarem synthetischen Flugzeugtreibstoff als Beitrag zur Transformation der Reviere in NRW – Abschlussbericht
S. Weiske, F. Schorn, J. L. Breuer, L. Becka, N. Beltermann, N. Wegener, R. C. Samsun, P. Moser, S. Schmidt, C. Götte, E. Rietmann, U. Balfanz, A. Spieckermann, D. Beckmann, J. Edler-Krupp, F. Steffen und R. Peters (2022), 167 pp
ISBN: 978-3-95806-630-4

Band / Volume 581
Schlussbericht
Accelerating Low- carbon Industrial Growth through CCUS (ALIGN-CCUS)
S. Weiske, S. Schemme, R. C. Samsun, R. Peters, S. Troy, S. Morgenthaler, D. Schumann, P. Zapp (2022), 216 pp
ISBN: 978-3-95806-632-8

Band / Volume 582
Closed Carbon Cycle Mobility –
Klimaneutrale Kraftstoffe für den Verkehr der Zukunft
F. Schorn, J. Häusler, J. L. Breuer, S. Weiske, J. Pasel, R. C. Samsun, R. Peters (2022), 220 pp
ISBN: 978-3-95806-636-6

Band / Volume 583
Machine learning for monitoring groundwater resources over Europe
Y. Ma (2022), viii, 125 pp
ISBN: 978-3-95806-638-0

Band / Volume 584
Mechanical properties of single and dual phase proton conducting membranes
W. Zhou (2022), IV, VI, 133 pp
ISBN: 978-3-95806-645-8

Weitere ***Schriften des Verlags im Forschungszentrum Jülich*** unter
http://wwwzb1.fz-juelich.de/verlagextern1/index.asp

Energie & Umwelt / Energy & Environment
Band / Volume 584
ISBN 978-3-95806-645-8

Mitglied der Helmholtz-Gemeinschaft

JÜLICH
Forschungszentrum